DEVELOPMENT OF NON-TRADITIONAL FRET-BASED FLUORESCENT SENSORS

by

Rehan Higgins

B.Sc., The University of Victoria, 2014

A THESIS SUBMITTED IN PARTIAL FULFILLMENT OF

THE REQUIREMENTS FOR THE DEGREE OF

MASTER OF SCIENCE

in

THE FACULTY OF GRADUATE AND POSTDOCTORAL STUDIES

(Chemistry)

THE UNIVERSITY OF BRITISH COLUMBIA

(Vancouver)

May 2021

The following individuals certify that they have read, and recommend to the Faculty of Graduate and Postdoctoral Studies for acceptance, a thesis entitled:

DEVELOPMENT OF NON-TRADITIONAL FRET-BASED FLUORESCENT SENSORS

submitted by Rehan Higgins in partial fulfillment of the requirements for

the degree of Master of Science

in Chemistry

Examining Committee:

W. Russ Algar, Associate Professor, Chemistry, UBC
Supervisor

Suzana Straus, Professor, Chemistry, UBC
Supervisory Committee Member

Glenn Sammis, Associate Professor, Chemistry, UBC
Supervisory Committee Member

Abstract

Fluorescence is a powerful tool for probing changes in structure on the nanometer scale. Förster resonance energy transfer (FRET) between fluorophores has a strong distance dependence in the 1-10 nm range, enabling indirect observation of minute positional changes. FRET has been used extensively for investigation of biomolecular systems and for the design of nanostructures for sensing biomolecules. This thesis describes the design of several FRET based nanostructures for fluorescence-based sensing of biomolecules.

Molecular logic devices (MLDs) have the potential to make efficient biosensors which deliver complex information with a single output signal. These devices take multiple inputs and apply Boolean logic operations to produce a single binary (*i.e.* TRUE/FALSE) output. The unique molecular recognition abilities of DNA make it an ideal material for the construction of MLDs. Several DNA-based MLDs using FRET sensitized fluorescent emissions as output signals were devised. One of these devices was a protease biosensor designed to detect the presence *and* activity of a target protease, providing useful information about the target while reducing the rate of false-positive results. Though a working sensor was not ultimately achieved, important limitations on the design of this type of device were revealed. Two other devices were designed for the amplification of output signals from MLDs, an important aim to allow for more sensitive devices and more efficient logic circuits. Both devices were designed and tested using cascading DNA hybridization reactions to produce amplification of fluorescent output signals.

Chemical ‘nose’ arrays utilize a panel of sensor elements which have non-specific but differing responses to targets to generate a unique ‘fingerprint’ pattern for each analyte. FRET between

quantum dots (QDs) and dyes on peptides conjugated to QD surfaces can be used to determine rates of proteolysis. QDs with different surface chemistries can be used as individual sensor elements for the construction of a chemical 'nose' array to differentiate proteases, where the pattern of initial rates for the different surface chemistries represents the unique 'fingerprint' for a given protease. Three ionic QD surface ligands were synthesized, characterized, and tested for their effects on proteolysis and ability to differentiate between a panel of proteases.

Lay Summary

Fluorescence—the emission of light caused by excitation of electrons in a material—is a critical tool for investigating the interactions between structures at size scales below the limits of optical microscopes. Short range (1-10 nanometre) energy transfer between fluorescent molecules or nanoparticles can be used to detect changes in the positions of or interactions between biomolecules. In this thesis, several nanostructures were designed and developed for the detection of different biomolecular inputs, using changes in fluorescent emissions as measurable output signals. DNA-based logic gate devices were designed to produce single TRUE/FALSE fluorescent output signals to simultaneously detect the presence of multiple biomolecular inputs by utilizing Boolean logic functions. The results herein can be used to guide further development of these adaptable logic gate design strategies. Contributions were also made towards a fluorescent sensor array for the detection of proteases and using highly fluorescent nanoparticles (quantum dots).

Preface

This thesis is based on currently unpublished work. Rehan Higgins co-designed the research and completed the experiments and data analysis. Rehan Higgins wrote the thesis. Dr. Russ Algar co-designed the research and helped edit the thesis. Protease kinetics experiments were also co-designed by Tiffany Jeen and Katherine Krause.

Table of Contents

List of Tables

List of Figures

List of Abbreviations

A	Adenine
ABTS	2,2′-azino-bis(3-ethylben-zothiazoline-6-sulfonic acid)
ACN	Acetonitrile
AMP	Adenosine monophosphate
APS	Ammonium persulfate
ATP	Adenosine triphosphate
BHQ-2	Black hole quencher 2
Boc	Tert-butoxycarbonyl
Boc_2O	Di-tert-butyl dicarbonate
bp	Base pairs
C	Cytosine
CE	Capillary Electrophoresis
CHA	Catalytic hairpin assembly
Cy3	Cyanine 3
DCC	N, N′-Dicyclohexylcarbodiimide
DHLA	Dihydrolipoic acid
DHLA-C6	N-(6-(2,5-dioxopyrrolidin-1-yl)-6-oxohexyl)-6,8-dimercaptooctanamide
DIC	N,N´-Diisopropylcarbodiimide
DMAP	4-Dimethylaminopyridine
DMSO	Dimethyl sulfoxide
DNA	Deoxyribonucleic acid
DPBS	Dulbecco’s phosphate buffered saline
DPS	2,2′-Dipyridyldisulfide
dsDNA	Double stranded DNA
EB	Ethidium bromide
EDC	1-Ethyl-3-(3-dimethylaminopropyl)carbodiimide
ESI-TOF-MS	Electrospray ionization time-of-flight mass spectrometry
FAM	6-carboxyfluorescein

FRET	Förster resonance energy transfer
FTIR	Fourier transform infrared spectroscopy
FWHM	Full-width-at-half-maximum
G	Guanine
GSH	Glutathione
HDA	Hexadecylamine
His	Histidine
HP	Hairpin
HRP	Horse radish peroxidase
IR	Infrared
kDa	Kilodalton
LA	Lipoic acid
LA-C6	6-(5-(1,2-dithiolan-3-yl)pentanamido)hexanoic acid
LA-NHS	Lipoic acid succinimidyl ester
LLC	Luminescent lanthanide complex
Me_4N-DHLA	2-((5-(1,2-dithiolan-3-yl)pentanoyl)oxy)-N,N,N-trimethylethan-1-aminium
MeOH	Methanol
MLD	Molecular logic device
MS	Mass spectrometry
MWCO	Molecular weight cut-off
NHS	N-hydroxysuccinimide
NMR	Nuclear magnetic resonance
Ni-NTA	Ni^{2+}-nitrilotriacetic acid
NIR	Near-infrared
PAGE	Polyacrylamide gel electrophoresis
PL	Photoluminescence
PO_4-DHLA	2-(6,8-dimercaptooctanamido)ethyl phosphate
QD	Quantum dot
QY	Quantum yield

RCA	Rolling circle amplification
RCF	Relative centrifugal force
RNA	Ribonucleic acid
s-Cy3.5	Sulfo Cyanine 3.5
s-Cy5	Sulfo Cyanine 5
s-Cy5.5	Sulfo Cyanine 5.5
SELEX	Systematic evolution of ligands by exponential enrichment
SO_4-DHLA	2-(5-(1,2-dithiolan-3-yl)pentanamido)ethyl sulfate
ssDNA	Single stranded DNA
T	Thymine
TBE	Tri-borate-EDTA buffer
TCEP	Tris(2-carboxyethyl)phosphine
TEMED	Tetramethylethylenediamine
THF	Tetrahydrofuran
TLC	Thin layer chromatography
TMAH	Tetramethylammonium hydroxide
TMB	3,3',5,5'-tetramethylbenzidine
TOP	Trioctylphosphine
TOPO	Trioctylphosphine oxide
UV	Ultraviolet

Acknowledgements

Thank you to Dr. Russ Algar for the support, guidance, encouragement, and wealth of knowledge that you have given me over the past several years. It has been a real pleasure being part of your group. Your dedication, intelligence, and humility are inspiring to any young hopeful scientist.

Thank you to all my past and present colleagues in the Algar group, it has been a joy to work with you all and I wish everyone the best for their bright futures! Special thanks to Melissa Massey, Kelly Rees, and Katherine Krause for help with research and advice which contributed to this thesis.

Lastly, a big thank you to my family for the endless encouragement along the way. Thanks to my mom for sparking my interest in science, my dad for teaching me how to write, and my grandma for inspiring me with her lifelong curiosity and desire to learn. And to my siblings for listening to me constantly whinge about school.

Chapter 1: Introduction

Fluorescence is a powerful and versatile tool for probing biochemical systems at the molecular level. Specific conjugation or interactions of fluorophores allows for the analysis of biomolecules in their natural environment—something that is not possible with most other analytical techniques. Distance-dependent Förster resonance energy transfer (FRET) between fluorophores attached to biomolecules provides information about nanoscale conformational changes in biomolecules in real time, a phenomenon which has been used extensively in the field of bioanalysis. This thesis details several projects that aimed to develop FRET-based molecular devices for the detection and analysis of biomolecules.

Molecular logic devices (MLDs) employ Boolean operations to yield a single binary output from multiple independent inputs [1]. Nucleic acids have proven to be well suited for construction of MLDs as they exhibit exceptionally specific molecular recognition through Watson-Crick-Franklin base pairing [2]. DNA logic devices often employ FRET as a means of generating fluorescent output signal and have been designed for applications in bioanalysis, drug delivery, and molecular computing. An essential target in the design of efficient DNA logic devices is a high TRUE/FALSE signal contrast. This chapter will first introduce some of the fundamental concepts of fluorescence and DNA nanotechnology and then review strategies for the amplification of output signals in DNA logic devices.

1.1 DNA Nanotechnology

The increasingly facile and inexpensive synthesis of oligonucleotides with custom sequences in recent years has enabled the design and synthesis of complex nanostructures made from DNA. The relatively simple and predictable secondary structures of DNA allow for rational design of nanostructures. Careful design of oligonucleotide components has been used to produce a huge range of two- and three-dimensional DNA nanostructures over the past several decades [3]. The reversible nature of Watson-Crick-Franklin base pairing allows for design of systems capable of changing in response to stimuli (*e.g.* solvent conditions, temperature, presence/absence of other oligonucleotides, etc.) [4]. These dynamic DNA nanostructures enable unprecedented manipulation of the relative positions of components on the nanoscale, leading to a variety of applications in nanoparticle synthesis and functionalization [5], photonics [6], biosensing [7], and targeted drug delivery [8]. DNA logic gates are a class of DNA nanodevices which employ structural changes in response to Boolean inputs to alter the interaction between functional components (*e.g.* fluorophores) to produce a change in signal (*e.g.* fluorescence). This chapter will introduce relevant concepts regarding the structure, mechanics, and modification of oligonucleotides which are needed to understand/appreciate the research in this thesis.

1.1.1 DNA Structure

Complementary oligonucleotides typically hybridize to form B-DNA, a well-defined double-helical structure. Under suitable conditions, the geometric parameters (*e.g.* pitch, rise, diameter, etc.) of this structure are constant and precisely known [9]. This allows for accurate prediction of

the dimensions of DNA nanostructures through simple calculations based on the oligonucleotide sequences. Though varied in form and function, DNA logic gates are typically constructed from B-DNA duplex structures [10]. Due to the anti-parallel nature of the hybridization in B-DNA, oligonucleotides are capable of self-hybridizing to form hairpin (or stem-loop) structures (Figure 1.1a). A hairpin is formed when complementary segments hybridize into a double-stranded *stem*, with the single-stranded segment between them in the nucleotide sequence forming the *loop*. These structures have proven to be useful in creating fluorescent *molecular beacons* [11] and as means of creating *hidden toeholds* (*vide infra*) [12].

In nature, DNA usually exists as very long polynucleotides (millions of bases) hybridized with their complementary strands in double helices. DNA nanostructures use much shorter oligonucleotides (typically tens to hundreds of bases) and often utilize partially complementary sequences to create more complex morphologies (Figure 1.1). For example, four partially complementary strands can be co-hybridized to produce an immobile Holliday junction (Figure 1.1b). These multi-strand junctions can be used in combination and form the basis for the more complex higher order DNA nanostructures [13]. Other secondary structures of DNA exist, including double helix structures with different geometries (*e.g.* Z-DNA) as well as triple- and quadruple-stranded structures [14]. Though much less common in genetic DNA, some of these alternative structures have been used extensively in synthetic DNA nanostructures [15]. In particular the G-quadruplex structure (Figure 1.1c), where a four guanine bases combine to form a stackable tetrad, has found many applications in the field [16].

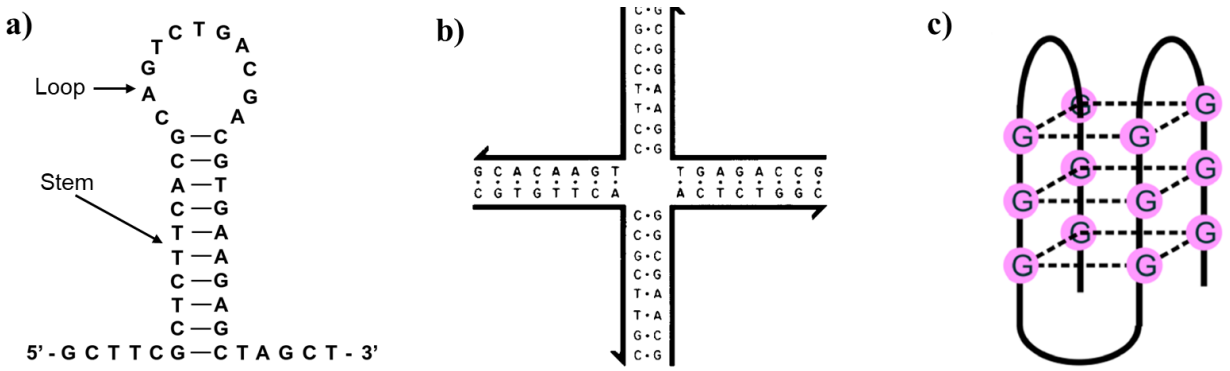

Figure 1.1 DNA secondary structures. **(a)** Hairpin/stem-loop structure, **(b)** immobile Holiday junction, and **(c)** G-quadruplex. Panel **(b)** is reproduced from [12] with permission from AAAS, and panel **(c)** is reproduced from [16] with permission from Springer Nature.

1.1.2 DNA Mechanics

Secondary structures of DNA are primarily stabilized by the hydrogen bonds formed between bases on complementary strands and stacking between adjacent bases on a strand [17]. The thermodynamic stability provided by base pairing and stacking competes with electrostatic repulsion between the charged phosphate backbones [18]. The stability provided by a guanine-cytosine (G-C) base pair is greater than that of an adenosine-thymine (A-T) pair due to the additional hydrogen bond in a G-C pair. The melting temperature (T_m) of a DNA duplex is defined as the temperature at which half of the population is dissociated into its constituent single strands and is a measure of the strength of the hybridization between two oligonucleotides.

For oligonucleotides in an aqueous environment, the T_m is primarily dependent on the sequence and concentration of the DNA. The strength of base-pairing and base-stacking interactions increases with the number of nucleotides and the G/C content of the sequences [17,19]. Higher

concentrations of cations, especially divalent cations such as Mg^{2+}, also stabilize duplex formation by shielding the negative charge of the phosphate backbones, reducing the electrostatic repulsion. The concentration of oligonucleotides also plays a significant role in determining the T_m, as rehybridization of separated strands becomes a more likely event at higher concentrations. Designing dynamic DNA structures requires careful control of the T_m of the various components. The binding energies must be strong enough to ensure a large majority of the oligonucleotide population adopts the same secondary structures under the desired conditions. Conversely, the hybridization of strands in the initial configuration must be weaker than that of the final configuration to provide a thermodynamic driving force for the interactions with other oligonucleotides or molecules.

1.1.2.1 Toehold Mediated Strand Displacement

DNA base pairs are susceptible to thermal fluctuations that result in short-lived disruption of hydrogen bonding interactions. This phenomenon, known as *DNA breathing* (or *fraying*), occurs more often at the ends of helices due to the relative lack of stabilization by base-pair stacking [20]. In nature, DNA breathing results in migration of branch points between homologous DNA strands during recombination [21]. Synthetic DNA structures often use displacement of one oligonucleotide by another to produce a conformational change or to change the relative spatial position of a label (*e.g.* fluorophore). The migration of a DNA junction is a stepwise random walk process with the forward and reverse migrations equally likely for each step [22]. The duplex formed with an 'invading' strand will be thermodynamically favored if it has more paired bases than the original duplex contained.

The rate limiting step for the displacement process is the initial nucleation step in which the invading strand first hybridizes to its complementary strand. For displacement of a stable duplex with two fully complementary strands, nucleation requires significant separation of the existing duplex and hybridization of the invading strand to occur simultaneously, and its rate is typically considered to be negligible [23]. The rate of displacement can be drastically altered by addition of a *toehold*—a single-stranded domain extending from the duplex. This toehold allows an invading strand with a complementary domain to the toehold to colocalize before displacing the existing strand via random branch migration (Figure 1.2). The increase in the rate of displacement from a toehold is dependent on the strength of its hybridization with the invading strand and can be tuned by altering its length and/or its G/C content. Increasing the length of toeholds has been shown to affect the rate of displacement across six orders of magnitude [24]. Inclusion of a spacer between the toehold and displacement domains creates a *remote toehold*, allowing for finer tuning of the displacement rate across three orders of magnitude by altering the length or stiffness of the linker [25]. A stronger toehold also serves to increase the thermodynamic favourability of the resulting duplex, reducing the rate of backwards reaction.

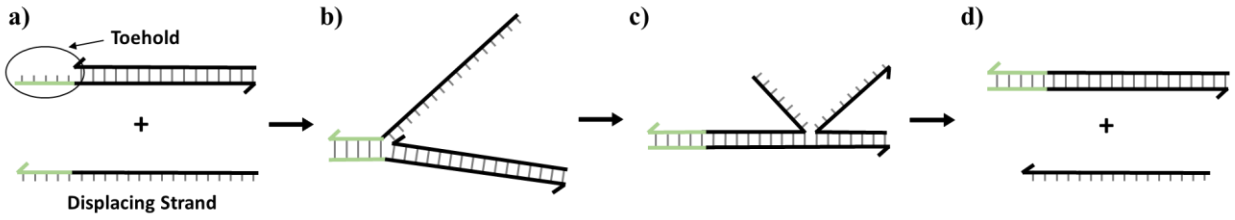

Figure 1.2 Toehold-mediated strand displacement. **(a)** The duplex DNA has a single-stranded toehold that **(b)** the displacing strand binds to. **(c)** This hybridization initiates migration of the branch point which leads to **(d)** displacement of the original strand and formation of a new duplex.

Toehold-mediated strand displacement is an almost ubiquitous tool in the design of dynamic DNA devices. The mechanism was first used to reversibly open and close a set of DNA nanotweezers [26], and has since been employed in a wide variety of DNA nanomachines including walkers [27], motors [28], and many more [4]. Toeholds can be effectively hidden by placing them in a double-stranded domain (often the stem of a hairpin) with relatively weak hybridization [29,30]. This strategy allows the displacing strand and the toehold-containing strand to coexist in solution and only hybridize with the addition of a stimulus (*e.g.* an oligonucleotide that hybridizes to open the hairpin). Toehold binding and branch migration domains can also exist on two separate nucleotides for more versatile and adaptable displacement designs. This *associative toehold activation* is achieved by including a complementary domain on a separate nucleotide—one containing a toehold binding domain and the other a displacing domain—to join the two domains together and initiate strand displacement [31]. Hidden toeholds and associative toehold activation are both important tools in the design of DNA logic gates and circuits as they can enable cascading hybridization reactions to occur from single inputs.

1.1.2.2 Proximity-Induced Intramolecular Strand Displacement

For hybridization of random-coil single-stranded DNA (ssDNA) the identity of the rate limiting step is temperature dependent. At higher temperatures the nucleation step, in which the two nucleotides associate and form the first few base pairs, is rate limiting. At lower temperatures, diffusion of the two nucleotides in solution becomes the rate limiting step [32,33]. These steps both depend on DNA concentrations, meaning an increase in effective concentration leads to an increase in reaction rate. The effective concentration of DNA can be dramatically increased by

affixing oligonucleotides to a common host. This phenomenon is known as *proximity-induced intramolecular strand displacement* and has been accomplished by hybridization to a common DNA 'track' [34], attachment to nanoparticles [35], and through DNA-protein interactions [36]. Increasing the effective concentration of oligonucleotides encourages hybridization of strands that would not hybridize free in solution under analogous conditions. This can greatly reduce background signals by reducing the unwanted hybridization of components free in solution, and has been used to engineer protein biosensors with very low detection limits [36,37]. Low background signal for FALSE outputs is a desirable trait for DNA based logic gates, and proximity-induced strand displacement has potential to be a very useful tool in these applications.

1.1.3 DNA Modification

Modification of DNA to incorporate non-nucleotide species into oligonucleotides is critical to their use in nanotechnology applications. A wide variety of synthetic modifications are available, many of which fall outside the scope of this research [38]. The incorporation of reactive moieties and their use for conjugating DNA with fluorescent dyes or nanoparticles are discussed below.

1.1.3.1 Functionalizing DNA with Reactive Tags

Many applications of DNA nanotechnology require attachment of oligonucleotides to signalling molecules (*e.g.* fluorescent dyes), surfaces, or biomolecules. Incorporating a stable reactive tag during synthesis allows for facile post synthetic modification to specifically conjugate the

oligonucleotide. Effective conjugation reactions with DNA attach non-nucleotide species with high yield to a specific position in the sequence. These reactions are typically carried out under mild aqueous conditions to ensure DNA solubility and to avoid oligonucleotide degradation. Common reactive tags and conjugation reactions include, but are not limited to, thiols for maleimide coupling [39], alkynes or azides for copper-catalyzed cycloadditions [40], and primary amines for NHS-ester coupling [41].

Solid-state DNA synthesis involves sequential addition of phosphoramidite modified nucleobases from the 3' to 5' termini. Molecules containing reactive tags can be easily added to the 5' terminus of an oligonucleotide during synthesis as phosphoramidites [41]. Addition of reactive tags to the 3' terminus is also possible but generally less desirable due to the higher cost of reagents. Inclusion of internal reactive tags (within the oligonucleotide sequence) is more complex, but can be achieved through modification of the base, sugar, phosphate group, or replacement of a nucleoside with a molecule of the same size [42]. Modification of a base within a nucleotide sequence influences its hybridization, with the degree of this effect highly dependent on the type of modification.

Labelling DNA with fluorescent reporters is a common strategy to provide output signals in DNA logic gates and other DNA nanotechnology applications. Fluorescent dyes with emissions ranging from ultraviolet (UV) to near infrared (NIR) are readily available with reactive moieties for conjugation with reactive tags on oligonucleotides. Alternatively, nucleosides modified with fluorescent dyes can be directly incorporated into oligonucleotides during synthesis [43], though the range of dyes available for this strategy is more limited. Organic dyes have been shown to

exhibit small stabilizing effects on duplex formation when attached to the termini of oligonucleotides [44].

1.1.4 Ligation

Construction of large DNA nanostructures typically requires connection of many shorter oligonucleotides into a larger construct. Enzymatic ligation to form covalent bonds between oligonucleotides at the junctions has been extensively used to produce robust one-, two-, and three-dimensional DNA nanostructures [3]. Ligases catalyze the formation of a phosphodiester bond between adjacent 3'-hydroxyl and 5'-phosphoryl groups in a double-stranded DNA (dsDNA) duplex [45]. These adjacent groups can appear at a nick in a long DNA strand or, more importantly for DNA nanotechnology applications, at a *sticky end* junction between two duplexes (Figure 1.3). These junctions are formed by a small overhang of ssDNA at the end of a duplex, which hybridizes to a complementary overhang on a target for ligation. Ligations in the laboratory are typically carried out by one of several different bacterial or viral ligases that have some structural differences but all follow the same general reaction mechanism [46].

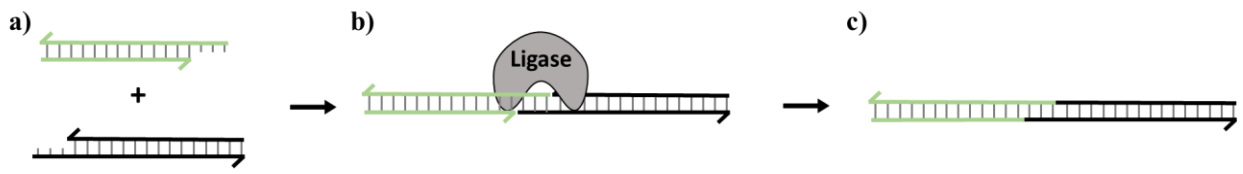

Figure 1.3 Sticky end ligation. **(a)** When duplexes with dangling single-stranded 'sticky ends' are mixed, **(b)** the ligase interacts with the weakly hybridized sticky ends. After ligation **(c)** both sets of nucleotides are joined, forming a single larger duplex.

T4 bacteriophage DNA ligase is the most commonly used ligase in DNA nanostructure synthesis, in part due to its ability to ligate *blunt ends* (*i.e.* DNA duplexes without ssDNA overhangs) [47]. T4 DNA ligase consists of a single polypeptide chain with a molecular weight of approximately 6.8 kDa and relies on ATP and Mg^{2+} as cofactors. The reaction mechanism has three main steps: activation of the enzyme with ATP to form a ligase-AMP complex, transfer of the AMP to the 5' phosphoryl group, and catalysis of the ligation reaction to form a phosphodiester bond and release AMP [45]. In contrast to other DNA ligases, T4 forms a relatively stable complex with the DNA after transfer of the AMP. Blunt-end ligation with T4 is attributed to this complex existing long enough to allow contact with another DNA duplex and subsequently catalyze the ligation reaction [48]. The ligase-DNA complex consists of the adenylated protein as a C-shaped clamp wrapped fully around the DNA helix, where it can move laterally to a phosphorylated 5' terminus [49]. Though the ligase does not differentiate between DNA sequences, the presence of ribonucleosides [49] or 2'-O-methylation [50] adjacent to the ligation site has been shown to significantly disrupt the enzymatic activity. It can be surmised from this observation that other nucleotide modifications in the region of the ligation site are likely to affect the enzyme activity. In the case where both inter- and intramolecular ligation are possible, the intermolecular reaction can be favoured by

increasing the DNA concentration (or effective concentration). Inducing DNA condensation by addition of hexamine cobalt chloride or polyethylene glycol has been shown to result in an increased proportion of intermolecular products for blunt-end ligation with T4 DNA ligase [51,52].

1.2 Fluorescence

Photoluminescence (PL) is the emission of light from a substance resulting from the absorption of a photon. Absorption of a photon results in an excited-state electron that can produce emission in two ways: relaxation from a singlet excited state (fluorescence) or relaxation from a triplet excited state (phosphorescence). The relaxation of a triplet excited state to the ground state is a spin-forbidden transition and, as a result, phosphorescence is typically a relatively long lived (~1 μs–10 s) and low intensity emission. Singlet-state relaxation is spin allowed and these fluorescent emissions are typically much more intense and shorter lived (~1–10 ns). Materials that exhibit fluorescence—called *fluorophores*—range from relatively simple organic molecules to metal complexes and clusters to semiconductor nanoparticles. Fluorophores of all types are widely applied as analytical tools, particularly in biochemical and biological applications. The following sections will briefly introduce the phenomenon of fluorescence and the classes of fluorophores relevant to the presented research.

1.2.1 Photophysics of Fluorescence

Fluorescence is a subset of PL that arises specifically from the relaxation of an electron in a singlet excited state and occurs via a three-stage process. First, a fluorophore must absorb a photon with an appropriate energy to excite an electron from the ground state (S_0) to an excited singlet state (S_1). Each electronic state (*e.g.* S_0, S_1) contains many vibrational energy states (v_n), giving many possible transitions between electronic and vibrational states. The absorption process occurs in approximately 10^{-15} s, which is significantly faster than the typical periods of vibration of nuclei (10^{-10}–10^{-12} s). The difference in time scales means that the nuclei are effectively stationary during photon absorption. This gives rise to the Franck-Condon principle which states that electronic transitions between states are more likely to occur if they result in no change of the position of the nuclei [53]. The shape of the absorption peaks of fluorophores is in part a result of this principle, with the largest peak representing the most favorable transition. Once excited, the electron remains in a higher electronic state for a finite amount of time, typically on the order of 10^{-10}-10^{-7}s, which is defined as the fluorescence lifetime. During this time, relaxation of the excited electron to the lowest vibrational state occurs, as transitions between vibrational states within an electronic state occurs on a 10^{-12}-10^{-10}s timescale. Vibrational relaxation results in some non-radiative energy loss, leading to a Stokes shift—the difference in wavelength between absorbed and emitted photons. Other types of non-radiative relaxation can occur during this time as well, most prominently internal conversion. These processes reduce the overall conversion efficiency of absorbed photons to emitted photons, referred to as the quantum yield (QY). In the final stage of fluorescence, the excited electron relaxes from the S_1 to S_0 state releasing the energy in the form of a photon. The excitation to S_1 occurs from the lowest energy level of S_0 and relaxation to S_0 occurs from the

lowest energy level of S_1 meaning the absorption and emission and spectra typically appear as mirror images each other.

1.2.2 Förster Resonance Energy Transfer

The energy of an absorbed photon can be released via several intrinsic or bimolecular pathways. One of these pathways is Förster resonance energy transfer (FRET). Named after the German scientist Theodore Förster, FRET is the non-radiative transfer of energy from an excited state of a donor chromophore to an acceptor chromophore via dipole-dipole coupling [54]. Importantly, this transfer occurs without contact between molecules and over relatively long distances (~1–10 nm). The rate of FRET (k_{ET}) is highly sensitive to the distance between the donor and acceptor pair (r):

$$k_{ET} = \left(\frac{R_0}{r}\right)^6 \frac{1}{\tau_D}$$

As the energy transfer can only occur from the excited state, k_{ET} is inversely proportional to the excited state lifetime (τ_D). The Förster distance (R_0) represents the donor-acceptor distance at which the FRET efficiency is 50%:

$$R_0 = 0.2108\left(\frac{\kappa^2 \Phi_D J}{n^4}\right)^{1/6} \qquad \text{(in Å)}$$

The Förster distance is dependent on the orientation of the transition dipoles (represented by the orientation factor κ), the quantum yield of the donor (Φ_D), the degree of overlap between the donor emission and acceptor absorbance spectra (represented by J), and the refractive index of the material between the donor and acceptor (n).

The utility of FRET as an analytical tool arises from its distance dependence. FRET interactions are typically relevant within the 1–10 nm range, with the usable range dependent on the R_0 value for a given donor-acceptor pair [55]. This scale is particularly useful for probing biological systems, as biomolecules typically fall within a similar size range (1-100 nm). Structural changes that alter the distance between the donor and acceptor within this range can be detected by a change in the intensity of FRET-sensitized emission (if the acceptor is a fluorophore) or quenching of the donor fluorescence. FRET has been extensively used as a 'nanoruler' to precisely track the distance between labelled materials in real time [56], and for more binary on/off switching in response to association or dissociation events. The foregoing are particularly useful for probing interactions between biomolecules, as well-placed labels can simply and effectively reveal the formation of complex structures in real time under biocompatible conditions.

1.2.3 Fluorophores

A wide range of naturally occurring and synthetic materials can produce fluorescent emissions. Each of these materials have distinct chemical and fluorescent properties that lend them unique advantages and drawbacks for different applications. The following sections will briefly describe the classes of fluorophores relevant to the presented research.

1.2.3.1 Fluorescent Dyes

Most organic fluorescent dyes are relatively small (< 2 kDa) compounds with extended aromatic and conjugated domains. In general, as the degree of conjugation increases, the wavelengths of absorption and fluorescence emission increase. This trend is a result of the decreasing energy gap between the ground state and the first excited state. The rigid planar structure of aromatic domains increases the quantum yields of dyes (*i.e.* efficiency of fluorescence) by reducing the non-radiative decay pathways associated with structural flexibility [57]. Heteroatoms substituted on an aromatic rings also have significant effects on their fluorescent properties, though the effect of the substituent position and identity are less easily generalizable [53]. Organic dyes are the most widely used and versatile fluorophores in modern applications. Hundreds of fluorescent dyes with emissions spanning from the near-infrared to UV have been developed [56]. Many of these dyes are commercially available with reactive tags for facile labelling of biomolecules [58]. These compounds also vary widely in other important qualities including solubility, stability, and quantum yield.

Fluorescence quenchers are a related class of compounds that have strong absorption in the UV-visible range but do not fluoresce themselves. These compounds can alter the fluorescence output of a system by quenching the emission of a fluorophore through FRET. Fluorophore-quencher pairs are often used in oligonucleotide-based molecular beacons, where signal is generated by a conformational change that removes the fluorophore from the FRET radius of the quencher [11].

Intercalating dyes are a subset of fluorescent dyes that specifically label DNA without direct conjugation. These dyes are typically planar molecules with a centre of rotation that greatly reduces their quantum yield. In solution, these molecules will insert themselves between bases of

a DNA duplex (or other secondary structure) where they are held via π-π bonding. This intercalation (or groove binding) effectively locks the molecule in a planar conformation causing a significant increase in quantum yield, thereby resulting in a large increase in fluorescent signal. Various dyes exist for the specific detection of duplex [59] and quadruplex [60] DNA. Though background fluorescence from the free dye is a significant drawback in many applications, intercalating dyes are very effective for the detection of DNA secondary structures where specific labelling is impractical.

1.2.3.2 Luminescent Lanthanide Complexes

Trivalent lanthanide ions (Ln^{3+}) display fascinating optical properties that arise from their unique electronic configurations. Ln^{3+} ions all share a [Xe]$4f^n$ (n = 0–14) configuration, with the unfilled 4f orbitals shielded by the filled $5s^2 5p^6$ subshells. The shielding prevents environmental perturbations of the 4f orbitals resulting in very well-defined energy levels. Line-like emissions from 4f-4f transitions span the NIR and visible ranges and have little sensitivity to the surrounding environment [61]. These transitions are formally parity forbidden, resulting in very long excited state lifetimes (µs–ms) [62]. The long-lived emissions are a key advantage of Ln^{3+}-based luminescent materials as they allow for time-gated measurements to reduce background signal from interfering fluorescence [63]. The forbidden nature of the transitions also means that Ln^{3+} ions have very weak absorption (0.1–10 M^{-1} cm^{-1}) [64].

The brightness of Ln^{3+} ions can be greatly increased by the presence of a sensitizing (or 'antenna') compound. Luminescent lanthanide complexes (LLCs) are constructed from Ln^{3+} ions with a

surrounding cage of ‘antenna’ chromophoric ligands. The primary role of these ligands is to absorb light and efficiently transfer it to the Ln^{3+} ion that produces emission [62]. The presence of efficient antenna ligands can increase the overall brightness of the Ln^{3+} centre by a factor of 10^4-10^5 [64]. To produce bright LLCs, ligands should have high molar absorptivities and effectively shield the Ln^{3+} centre from solvent-induced quenching. These ligands are typically multidentate to reduce solvent intrusion and maintain stability [62]. Finally, ligands often include reactive tags to allow conjugation of the LLCs to molecules of interest (*e.g.* oligonucleotides) [65].

1.2.3.3 Quantum Dots

The development of luminescent nanoparticles in recent decades has been motivated, in part, by the need for materials with optimized optical properties for more sensitive and robust fluorescent signalling. One of the most well developed and successful classes of these materials are quantum dots (QDs). QDs are colloidal semiconductor nanocrystals with exceptionally bright and robust PL emission. Cadmium chalcogenides are the most commonly used semiconductor materials as they generally produce QDs with the best visible-spectrum PL properties, though other QD materials have been developed [66]. The small size of QDs (typically 1–10 nm) produces a quantum confinement effect that is responsible for their fluorescence. The relatively small number of atoms in the nanocrystal reduces the number of orbitals available in the valence and conduction bands compared to the bulk material. This results in separation of the band into discrete energy levels at the band edge and an overall increase in the width of the band gap. Nanocrystals within a certain size domain, which varies between QD materials, have an appropriate band gap energy to

produce visible PL emission. Importantly, variation of QD size within this range can be used to continuously tune the emission wavelength.

The PL emission of QDs is generally brighter, narrower, and more robust when compared to most other luminescent materials. QDs have large molar extinction coefficients (10^5–10^7 M^{-1} cm^{-1}), absorb across a broad spectral range, and have relatively high quantum yields (0.1–0.9), producing exceptionally bright emission [67]. This combination, along with resistance to photobleaching, makes QDs well suited to analytical fluorescent applications, especially in the field of bioanalysis [68]. The narrow emission bands (full-width-at-half-maximum (FWHM) of 25–40 nm in the visible spectrum) of QDs makes them ideally suited to act as FRET donors [69]. Furthermore, the large size of the QDs relative to molecular dyes allows them to act as a donor to many FRET acceptors in parallel. The use of QDs in analytical applications typically requires some sort of modification of the nanoparticle surface to produce selective interactions between QDs and analytical targets.

1.2.3.3.1 QD-DNA Conjugation

Direct attachment of DNA to QD surfaces is critical to their incorporation into DNA logic devices. A necessary first step is the dispersion of QDs in aqueous media, which can be accomplished in two ways. The first method involves exchanging the hydrophobic surface ligands, which stabilize the QDs during synthesis, for hydrophilic small molecules or polymer ligands. Small-molecule ligands typically bind to the QD surface through thiol groups and have a distal hydrophilic group (*e.g.* carboxyl) to provide aqueous stability [69]. The other method preserves the hydrophobic

ligands of the QD by encapsulating the whole structure with an amphiphilic polymer or phospholipid. Here, the hydrophobic sections integrate with the QDs original hydrophobic surface ligands, while the outer hydrophilic regions provide aqueous stability and sites for functionalization [69]. Both methods are effective and used in different applications.

DNA-functionalized QDs were first developed in 1999, using both 3' and 5' thiol-terminated DNA to bind to the inorganic surface of the QDs [70]. Since this innovation, many alternative methods have been developed to either directly attach functionalized DNA to QD surfaces or to conjugate DNA to existing surface ligands [71]. Achieving a high density of DNA on the QD surface requires careful balancing of conditions to maintain the colloidal stability of the QDs while minimizing the electrostatic repulsion between the DNA strands and any charged surface ligands. Increasing ionic strength shields charges on both DNA and QD surface, allowing for more DNA-QD coupling while also risking QD aggregation. Stepwise addition of salt helps to negate the aggregation problem as QDs with some DNA on their surface are far less prone to aggregation [72]. Potential hydrogen bonding between nucleobases and QD surface ligands results in non-specific adsorption of oligonucleotides to QD surfaces, reducing their capacity to conjugate further DNA strands [73]. A DNA duplex has many fewer exposed nucleobases, reducing its capacity to hydrogen bond to the QD ligands, and conjugation with dsDNA has been shown to increase the DNA density on QD surfaces [74].

1.3 Amplified Photonic DNA Logic Gates

DNA logic gates are nanostructures made from oligonucleotides that take multiple inputs and perform a Boolean logic operation to produce a single TRUE or FALSE output. In photonic logic gates, this output comes in the form of a photonic emission, where a pre-defined threshold value determines whether output signals are TRUE or FALSE. To achieve approximately binary signal outputs, logic gates require good separation in the signal intensities of TRUE and FALSE states. A good photonic DNA logic gate should have a TRUE state with an intense luminescent signal and a FALSE state with minimal signal, giving a significant gap between the two states. Output signals for equivalent states (*e.g.* the three TRUE states of an OR gate) should be equal in intensity or at least consistently lie within a well-defined region. High TRUE:FALSE signal contrasts and predictable responses are particularly important for potential applications of DNA logic devices, including biosensing in biological media [75] and targeted drug delivery [76]. A 'traditional' photonic DNA logic gate employs a single fluorescent dye and quencher pair, with inputs causing a change in the interactions between these two components. This design has can produce a maximum of one fluorescent output per input which fundamentally limits the TRUE:FALSE signal contrast. Systems capable of amplifying the effect of inputs to induce many outputs have potential to produce fluorescent logic gates with much higher signal contrasts. The following sections will briefly introduce the field of DNA logic gates then review recent efforts to produce amplified photonic logic gates, either with or without the help of enzymes.

1.3.1 DNA Logic Gates

Logic gates are devices which take binary inputs—TRUE and FALSE or, alternatively, 1 and 0—and perform a Boolean operation to produce a binary output. There are four basic one-input Boolean operators, the most important of which are the YES gate (output = input) and the NOT gate (output = opposite of input). In the case of two-input Boolean operators there are a total of sixteen gates, representing the sixteen possible response patterns. These sixteen gates can all be expressed as combinations of the six elementary two-input Boolean logic gates (Table 1.1). The most intuitive and common of these are the AND gate (TRUE output in response to two TRUE inputs) and the OR gate (TRUE output in response to a one or two TRUE inputs).

Table 1.1 The six elementary two-input Boolean logic gates. These gates can be combined in series to produce all sixteen possible two-input logic gates.

Input		Output					
		AND	OR	NAND	NOR	XOR	XNOR
A	B			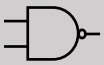	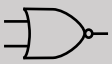		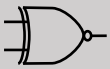
0	0	0	0	1	1	0	1
0	1	0	1	1	0	1	0
1	0	0	1	1	0	1	0
1	1	1	1	0	0	0	1

In the context of DNA logic gates, a TRUE input represents the presence of an input, typically an oligonucleotide, while a FALSE input represents its absence. Outputs for DNA logic gates are more varied, but many systems use photonic signals to produce measurable outputs. Toehold-

mediated strand displacement is a central mechanism in these logic gates, with inputs displacing an existing strand as they hybridize to the logic gate oligonucleotide. In photonic logic gates this can be used to produce a FRET sensitized photonic signal by bringing two fluorophores into proximity, or to restore the fluorescence of a fluorophore by removing a quencher from the system. A study by Massey *et al.* provides an illustrative example of the use of toehold-mediated strand displacement to produce several photonic logic gates (AND, OR, NAND, and NOR) [75]. In the OR gate (Figure 1.4), hybridization of either input to a central oligonucleotide results in displacement which separates fluorophores from a fluorescence quencher, restoring a FRET sensitized fluorescent signal.

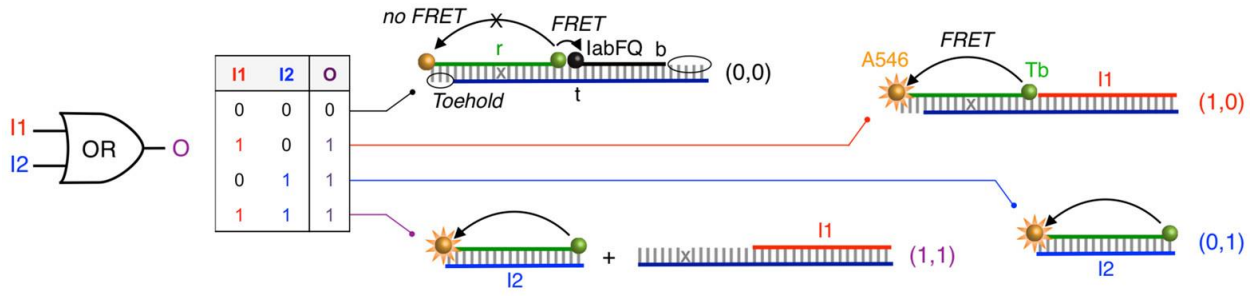

Figure 1.4 A FRET based photonic logic gate. The logic gate uses toehold-mediated strand displacement by input 1 (I1) *or* input 2 (I2) to separate an LLC FRET donor from a fluorescence quencher, producing a FRET sensitized fluorescent signal from the fluorescent dye (A546). Adapted from Ref. [75] with permission from American Chemical Society.

DNA based logic gates were initially developed with the ambitious goal of creating DNA-based computers [77–79]. The specific base-pairing of DNA allows for molecular recognition that is

unparalleled, making it an ideal material for the synthesis of logic gates on the nanoscale. Logic gates that produce oligonucleotide outputs through strand displacement can be connected in sequence to produce more complex logic circuits [80]. More recent research in the field has produced adaptable DNA logic gate systems that can be combined to produce circuits comprising tens or even hundreds of individual gates [81,82]. Though DNA computing remains a long-term goal, simpler DNA logic gates have found more immediate application in the field of bioanalysis. Logic gates can be used to produce biosensors capable of delivering complex information about multiple targets through a single output signal [83,84]. The use of OR gates, for example, can allow for simultaneous screening for multiple targets, while AND gates can reduce false positives in disease diagnostics by indicating the presence of multiple biomarkers.

1.3.2 Enzyme-Assisted Amplified DNA Logic Gates

Organisms have evolved an extraordinary array of enzymes for the synthesis, modification, and decomposition of DNA. Use of these enzymes in combination with synthetic DNA nanotechnology greatly enriches our ability to manipulate DNA at the molecular level. The catalytic nature of enzymes makes them a very useful tool for amplification in DNA logic gates. Enzymes are unique in their ability to specifically extend or cut oligonucleotides under relatively mild aqueous conditions. Enzymatic amplification in DNA logic gates typically involves the synthesis of many copies of an output strand. In the context of photonic logic gates, this type of system presents the inherent disadvantage of the output strands being unlabelled. Fluorescent signal must therefore come from intercalating dyes or via a secondary signal producing step, often through a DNAzyme (*vide infra*), which can contribute to higher background signals. A second

key disadvantage of enzymatic systems is the restriction to specific buffer and temperature conditions, and the complication of the system with enzyme co-factors and/or starting materials. Though this is not necessarily a disadvantage for every application, the more stringent reaction requirements generally reduce the versatility of logic gate applications, as well as the ability to combine logic gates into circuits. Overall, enzymatic amplification can be a powerful technique in certain applications, but generally produces less adaptable and translatable logic gate designs than those based purely on DNA hybridization.

DNA polymerases are commonly employed to amplify logic gate outputs by rapidly synthesizing oligonucleotides based on a template strand. These systems often leverage the powerful rolling circle amplification (RCA) technique to produce significant amplification of output oligonucleotides. A study by Chen *et al.* neatly illustrated this concept (Figure 1.5), using RCA to amplify the oligonucleotide output from an AND logic gate with oligonucleotide inputs with detection by the intercalating dye SYBR Green I [85]. In this system, the primer for the RCA was the output from a DNA AND logic gate complex. Once released the primer-initiated RCA, where the enzyme phi 29 DNA polymerase catalyzes the synthesis of a long repeating nucleotide. The fluorescent signal from SYBR Green I was consequently increased due to intercalation into the RCA product. The amplification cycle allowed for detection of the oligonucleotide inputs in amounts as low as 500 amol, making the device relevant for use in biological applications. Two other studies use combinations of enzymes and intercalating dyes to produce signal amplification [86,87]. Both of these studies, however, use the enzymes rather than oligonucleotides as inputs and are therefore less adaptable logic gate designs.

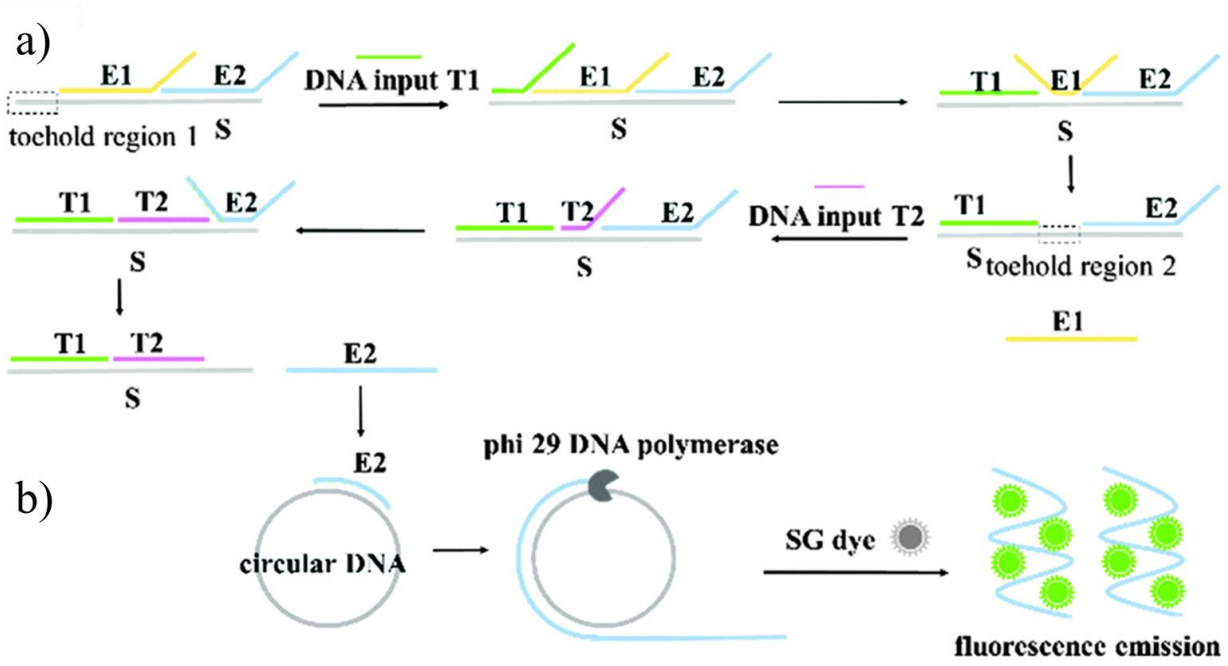

Figure 1.5 Rolling circle amplification (RCA) of an AND gate. **(a)** Hybridization of two inputs (T1 and T2) releases the output strand (E2). **(b)** The output strand initiates the RCA cycle, leading to the synthesis of long oligonucleotides into which SYBR green (SG) intercalates to produce a fluorescent signal. Adapted from Ref. [85], with permission from Royal Chemical Society.

Other studies employed polymerases and nicking endonucleases to produce many copies of a peroxidase-like DNAzyme (*vide infra*) that generates a chemiluminescent signal from the oxidation of luminol [88,89]. Here, logical inputs bind to oligonucleotide structures causing conformational changes that expose sites for interactions with the enzymes. The use of catalytic DNAzymes as a means of signal generation has the potential to compound the amplification effects and greatly increase the output. A study by Orbach *et al.* used DNA polymerase together with a nicking endonuclease to produce many copies of a Mg^{2+} dependent DNAzyme (*vide infra*) to cleave a *reporter* oligonucleotide labelled with both a fluorophore and a quencher [90]. Initially,

the fluorophore of the *reporter* is fully quenched, giving a very low background signal. Cleavage of the strand leads to spatial separation of the fluorophore and quencher, restoring the fluorescent signal. The combination of catalytic components (polymerase and DNAzyme) led to the cleavage of many reporter strands per input. Several logic gates were produced using this design with very good signal contrast in all cases, albeit with relatively slow responses, showing the power of this dual catalytic system.

1.3.3 Non-Enzyme Assisted Amplified DNA Logic Gates

Though enzymes are remarkably efficient at modifying and manipulating DNA they are not without drawbacks in the context of logic gate design. Enzyme-free amplification of logic gates is a desirable objective as these systems have the potential to produce more robust and adaptable nanodevices. In this type of system, DNA hybridization is used to achieve signal change, eliminating the need for added starting materials (*e.g.* nucleosides) and enzyme co-factors (*e.g.* ATP). Several approaches for the design of enzyme-free amplified logic gates are described in the following sections with examples from the recent literature.

1.3.3.1 Strand Displacement Cascades

As discussed in section 1.1.2, the kinetics of DNA strand displacement is highly dependent on the existence of single-stranded toehold regions. If a toehold region is effectively hidden in a double-stranded region, an invading strand can exist alongside the duplex in solution without initiating

strand displacement. Opening of the duplex to expose the toehold domain initiates the toehold binding and subsequent displacement. This type of system can be employed to produce a cascade of displacement reactions upon addition of an oligonucleotide initiator (or ‘catalyst’). A study by Qian and Winfree demonstrated the potential of displacement cascade reactions to amplify logic gates through a simple three-step catalytic cycle (Figure 1.6) [91]. To initiate the amplification step, a catalytic *input* strand binds to a toehold on the *gate* strand and displaces the *output* strand, simultaneously exposing a second toehold on the *gate* strand. The output strand then binds to a toehold on a quencher-labelled strand, displacing the hybridized fluorescent dye-labelled reporter strand and thereby producing a fluorescent signal. In the final step, a *fuel* strand binds to the exposed toehold on the gate strand, displacing the *input* strand to restart the cycle. Importantly all three oligonucleotides—the *input*, *output*, and *fuel* strand—form an equivalent number of base pairs with the *gate* strand giving them equal binding energies. Displacement of the input by the *fuel* strand is driven by the large excess of the *fuel* strand and the cycle repeats many times, with an impressive 15:1 TRUE:FALSE signal contrast achieved in the AND gate. A key advantage of this type of design is its ease of integration into larger logic circuits. As all components of the gate are oligonucleotides, the outputs from one gate can be taken as the inputs for a second gate. In the Qian and Winfree study, basic logic units were successfully integrated into a series of circuits, the largest of which was a 16-input square-root circuit, while maintaining relatively high signal contrast. One drawback of this system, and of DNA-based logic gates in general, is the relatively slow rate of the displacement reactions (Figure 1.6c). Though displacement can be sped up through the use of longer toeholds [24], the rate is ultimately limited by the random walk hybridization of the invading strand [22].

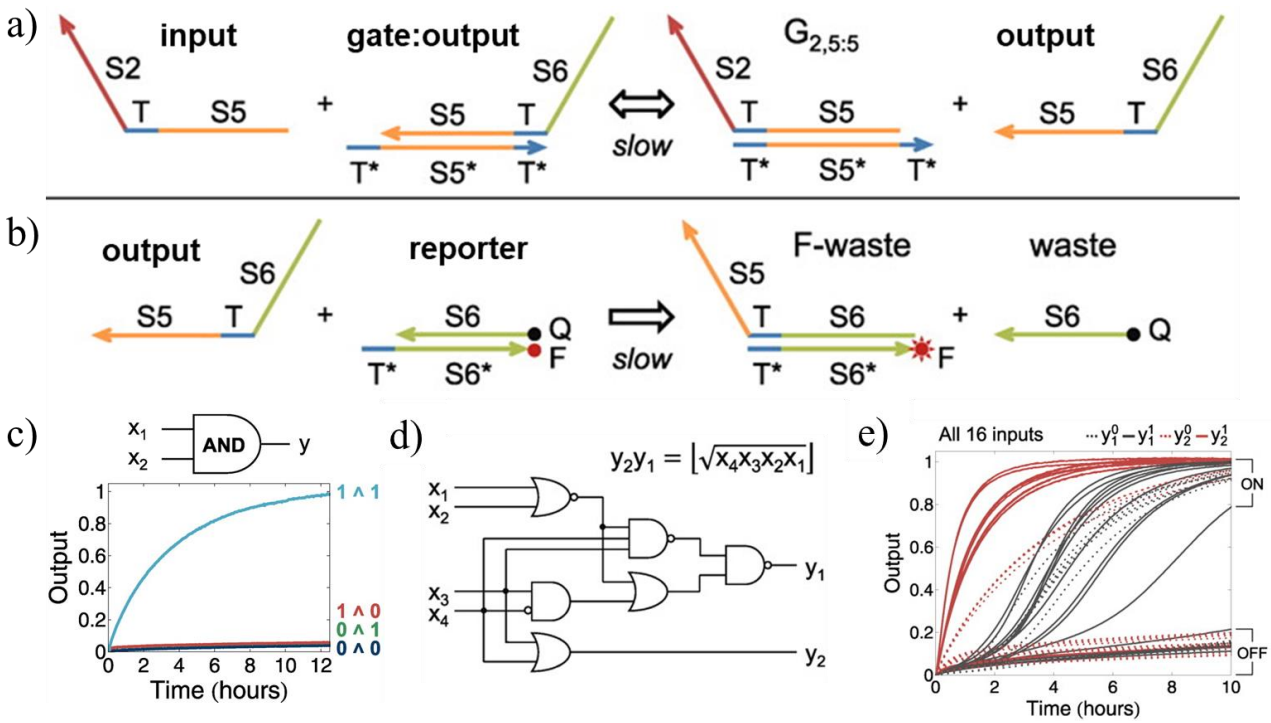

Figure 1.6 DNA logic gates based on strand displacement cascades. **(a)** To start the cycle the catalytic *input* strand hybridizes to the *gate* strand, displacing the *output*. **(b)** To generate a signal, the *output* then binds to the dye-labelled *reporter*, displacing its quencher labelled complement. The cycle is reset by displacement of the *input* by hybridization of a *fuel* strand to the *gate* (not pictured). This design scheme was used to make **(c)** simple logic gate components and **(d-e)** connect them into larger logic circuits with good signal contrast. Adapted from Ref. [91], with permission from AAAS.

The above type of catalytic cycle can also be exploited to produce larger DNA-linked structures as a means of signal amplification. Yao *et al.* demonstrated a similar amplification scheme to induce DNA mediated aggregation of gold nanoparticles [92]. A hidden toehold at each end of a linker strand was exposed by the displacement of a blocking strand by the two input *catalyst*

strands. DNA bound to the surface of a gold nanoparticle then hybridized with the linker strand displacing the *catalyst* strands and initiating a new displacement cycle. The shift in absorbance of the aggregated gold nanoparticles was taken as the TRUE signal for the AND logic gate. The use of gold nanoparticles here provides a simpler absorbance readout, while sacrificing some of the sensitivity and signal contrast of a fluorescent system.

1.3.3.2 Catalytic Hairpin Assemblies

Intramolecular hybridization can be used to hide toeholds within a single oligonucleotide. This allows for the construction of simpler systems, reducing the number of strands necessary to produce an amplification cycle. This is very beneficial in the context of DNA logic gates, as simpler systems are generally more robust and conducive to the construction of larger logic circuits. The intermolecular hybridization is typically used to create hairpin structures, where the toehold is hidden within the stem segment. Catalytic hairpin assemblies (CHAs) employ at least two separate hairpins with dangling ends which hybridize to form a duplex when opened but remain independent under the initial conditions. An initiator strand functions to open one of these hairpins, exposing a toehold to bind the dangling end of the other hairpin. Toehold mediated strand displacement of the initiator by the second hairpin releases the initiator from the complex to start another catalytic cycle. Catalytic hairpin assembly is a high efficiency method that can achieve thousand-fold amplifications under isothermal conditions [93]. It is also a relatively simple technique with the simplest versions involving only three oligonucleotides—an initiator and two hairpin strands. The efficiency and simplicity of CHA makes it well suited for use in nucleic acid logic gate systems.

A 2015 study by Guo *et al.* provides an illustrative example of this design in a logic gate application (Figure 1.7) [94]. This system consists of two partially complementary hairpin strands which, when hybridized, leave an exposed toehold for the hybridization of a fluorescent dye labelled strand. The catalytic *initiator* domain was separated into two strands: one carrying the toehold domain and the other carrying the displacement domain. These two strands remained separate in solution until the addition of the two AND *input* strands, which hybridized with them to form a four-stranded initiator complex. This *initiator* opened the first hairpin (*H1*) through toehold mediated strand displacement exposing a toehold to bind the second hairpin (*H2*). Displacement of the initiator by *H2* recycled the initiator to open another copy of *H1*. A single-stranded domain on *H1* was left available to bind to the toehold of the fluorescent dye labelled strand, removing it from its duplex with a quencher strand and restoring fluorescence. Several similar logic gates based on hairpin cascades have used modulation of FRET quenching to produce an output signal [95,96], while others have used peroxidase like DNAzyme [97,98]. Despite the described advantages of CHA systems, all the studies described above achieved only moderate signal contrast. This is likely due, in part, to high background signal caused by leakage, which can occur due to impurities in oligonucleotide components and breathing of the hidden-toehold containing duplexes [93]. CHA is a relatively recently developed technique, first introduced in 2008 [99], and there is still much room for progress in this field.

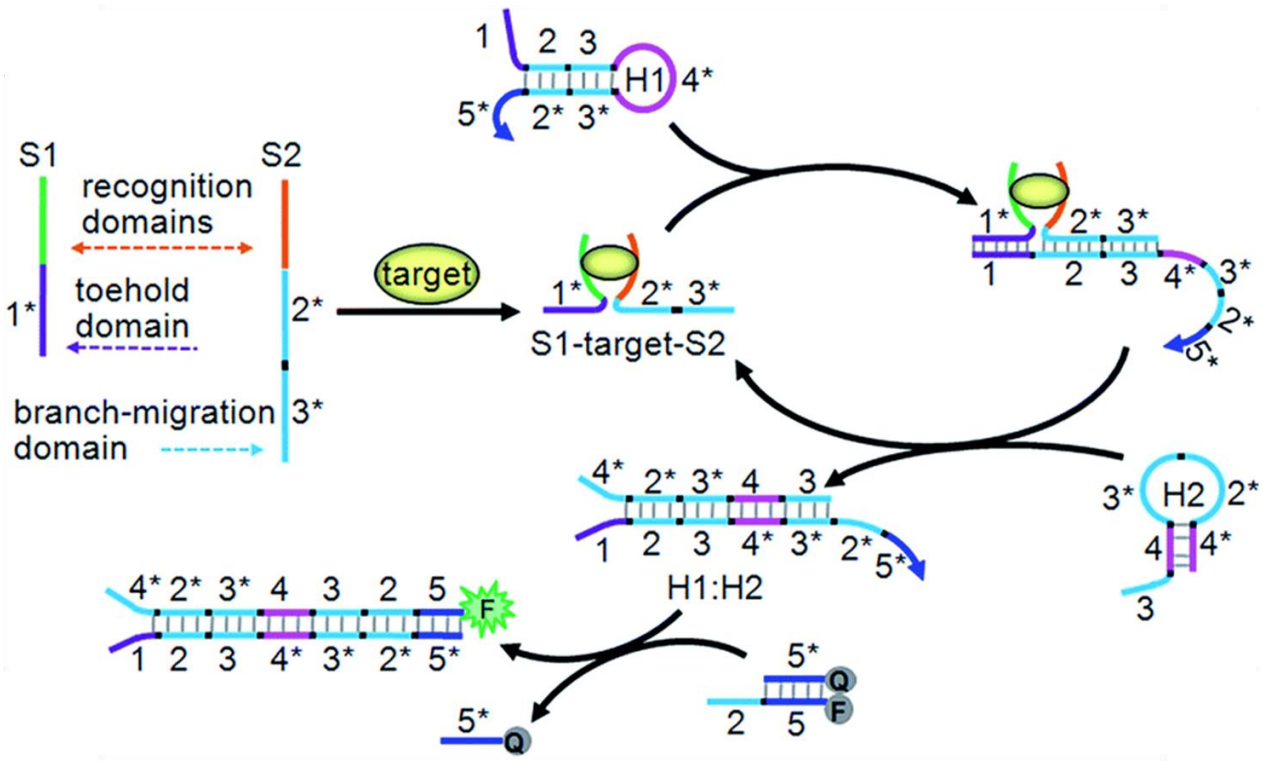

Figure 1.7 Catalytic hairpin assembly for AND gate detection of analytes. Target binding by the two inputs leads to opening of hairpin 1 (H1), which subsequently opens hairpin 2 (H2). This releases the inputs to restart the cycle and allows hybridization of the dye labelled *reporter*, producing a fluorescent signal. Reproduced from Ref. [94] with permission from Royal Society of Chemistry.

1.3.3.3 DNAzymes

Catalytic nucleic acids (DNAzymes) are oligonucleotides that form secondary structures capable of catalyzing reactions. The development of DNAzymes was inspired by the discovery of naturally occurring catalytic RNA molecules (ribozymes) in the 1980s [100]. Analogous DNA structures were discovered by screening large randomly generated libraries of oligonucleotides for catalytic activity through the systematic evolution of ligands by exponential enrichment process (SELEX)

[101]. Briefly, SELEX involves successive rounds of incubation of a pool of oligonucleotides with the catalytic target followed by separation and replication of the most active sequences. This process is iterated until the few best candidate oligonucleotides remain. The final oligonucleotides are then sequenced and fully characterized to determine their activity [102]. Using SELEX, a broad range of DNAzymes catalyzing several major classes of reactions have been developed in the past few decades. Though limited in function compared to enzymes, DNAzymes have the advantages of being more sequence addressable, resilient to varying conditions, and easily produced [101]. Among these, bond-cleaving and G-quadruplex-hemin DNAzymes have been used as a means of signal amplification for nucleic acid logic gates [103].

1.3.3.3.1 Bond-Cleaving DNAzymes

The first DNAzyme was developed in 1994 for the Pb^{2+} assisted cleavage of an RNA strand [104]. Many related DNAzymes have since been developed to cleave RNA and, more recently, DNA [105]. This class of DNAzymes functions by forming a duplex with their target strand, where the catalytic strand is pinched with a loop structure protruding from the duplex. This loop coordinates a divalent metal ion that is brought close to a phosphodiester bond on the target strand where it deprotonates the 2-hydroxyl leading the cleavage of the bond [106]. This catalytic reaction can be employed to produce fluorescent signal by adding reporter strands containing a fluorophore and quencher on either side of a cleavage site. Importantly, once cleaved, the two fragments of the reporter strand are too short to form stable duplexes with the DNAzyme and are released to allow binding of a new target. These reporter strands often have a ribonucleotide at the cleavage site as RNA-cleaving DNAzymes are typically more efficient than their DNA-cleaving counterparts.

Though a very useful tool in logic gate design, bond-cleaving DNAzymes are somewhat limited in their versatility as they have relatively restrictive requirements for pH and buffer conditions [101]. Furthermore, though cleaving of oligonucleotide sequences is useful as a means of fluorescent signal generation, it is less useful as a means of output propagation, limiting the use of these structures as intermediates in extended logic circuits.

The first cleavage DNAzyme based logic gates were developed in 2002, using hairpins to block the target binding sites of the DNAzyme [107]. Inputs activated the cleavage of the reporter strand by opening the hairpins via hybridization to allow target binding. This design strategy was used to produce NOT, AND, and XOR gates. Subsequent studies have produced more complex logic circuits based on the similar activation principles [108–110]. A study by Elbaz *et al.* used the pH dependence of two different DNAzymes to produce a pH controlled system with three switchable logic functions [111]. Several other studies use DNAzymes split between two separate oligonucleotides, where the logical inputs function to activate the DNAzyme by joining these domains. Perhaps the most interesting aspect of this type of logic gate design is its programmability. The DNAzyme subunits include programmable segments at either end of the active segment to bind an activator nucleotide and a substrate nucleotide. The utility of this design comes from the fact that these components can be easily interchanged, allowing a simple design to be used to create a variety of logic gates [112,113]. Most impressively, this design strategy was used to produce a range of logic gates which were used to detect cancer-linked miRNAs in samples of cell lysate [114]. This strategy can also be augmented by implementing more complex logical designs to join the DNAzyme subunits together, allowing for the construction of larger logic circuits [115,116].

1.3.3.3.2 G-quadruplex/Hemin DNAzymes

G-quadruplexes are non-canonical DNA secondary structures formed by stacked guanine tetrads [117]. The planar aromatic guanine tetrads are able to efficiently bind (typically aromatic) ligands through π-π stacking and electrostatic interactions, with the binding most commonly occurring at the exterior face of the quadruplex [118]. G-quadruplex forming sequences have been developed through SELEX to bind and metalate proporphyrin IX forming a G-quadruplex-hemin structure, which acts as a DNAzyme mimicking the catalytic activity of peroxidase enzymes [101]. Peroxidases catalyze oxidation of their substrates. Horseradish peroxidase (HRP), in particular, has been used extensively as a reporter enzyme due to its ability to catalyze oxidation reactions with chromophoric and fluorescent products [119]. This capability is very useful in the context of logic gate amplification, as a photonic signal can be generated from unlabelled strands while avoiding the use of intercalating dyes. The aromatic binding site of the G-quadruplex is functionally similar to the hemin binding pocket of HRP [120]. Likewise, the oxidative mechanism of the DNAzyme is thought to be similar to that of HRP giving the G-quadruplex-hemin DNAzymes analogous activities.

Peroxidase-like oxidation is typically used to produce colorimetric or chemiluminescent signals [16], but can also generate fluorescent signals (*e.g.* oxidation of Amplex Red to produce the fluorescent compound resorufin) [121]. Chen *et al.* used the G-quadruplex-hemin DNAzyme catalyzed oxidation of colourless 3,3',5,5'-tetramethylbenzidine (TMB) to the blue-green oxTMB as a signal reporter for a complete set of the two-input elementary logic gates [122]. The G-rich domain was initially hybridized in a hairpin, blocking the formation of a G-quadruplex and therefore the catalytic activity. Addition of the inputs activated a separate cleaving DNAzyme

which cleaved the hairpin allowing the G-quadruplex to form. The G-quadruplex subsequently bound hemin and the visible formation of oxTMB was quantified by absorbance measurements, with a signal contrast of approximately 5:1 achieved. A study by Gao *et al.* used the disruption of a triplex helical DNA structure by oligonucleotide logical inputs to release G-quadruplex-hemin DNAzyme to oxidize TMB [123]. Other studies have used metal ions and pH as logic gate inputs to control the formation of a G-quadruplex-hemin DNAzyme [124,125]. In general, the dependence on conditions (*e.g.* pH and cation dependence), intercalating compounds, and oxidizable dyes limits the versatility of this logic gate design.

A common strategy to employ G-quadruplex-hemin DNAzymes as signal reporters is to have the G-quadruplex domain in two separate sections (either in separate strands or on opposite ends of a single strand) that are brought together in response to a target analyte or input. This design modification enables systems with nucleotide inputs. Li *et al.* used a split G-quadruplex on the ends of a logic gate-actuated DNA nanotweezer to produce an amplified signal (Figure 1.8) [126]. The nanotweezers were held open by a DNA duplex and closed when one of the duplex strands was removed by hybridization with the two inputs. This brought the DNAzyme domains on the ends of the nanotweezers together to form a G-quadruplex and allowing the binding of hemin. The colorimetric signal was produced by the oxidation of the colourless 2,2′-azino-bis(3-ethylben-zothiazoline-6-sulfonic acid) ($ABTS^{2-}$) to the blue coloured $ABTS^{-}$. Other studies have used split G-quadruplex domains in a interlocked ring DNA nanostructure [127] or on the ends of a hairpin strand [128] to produce colorimetric logic gates.

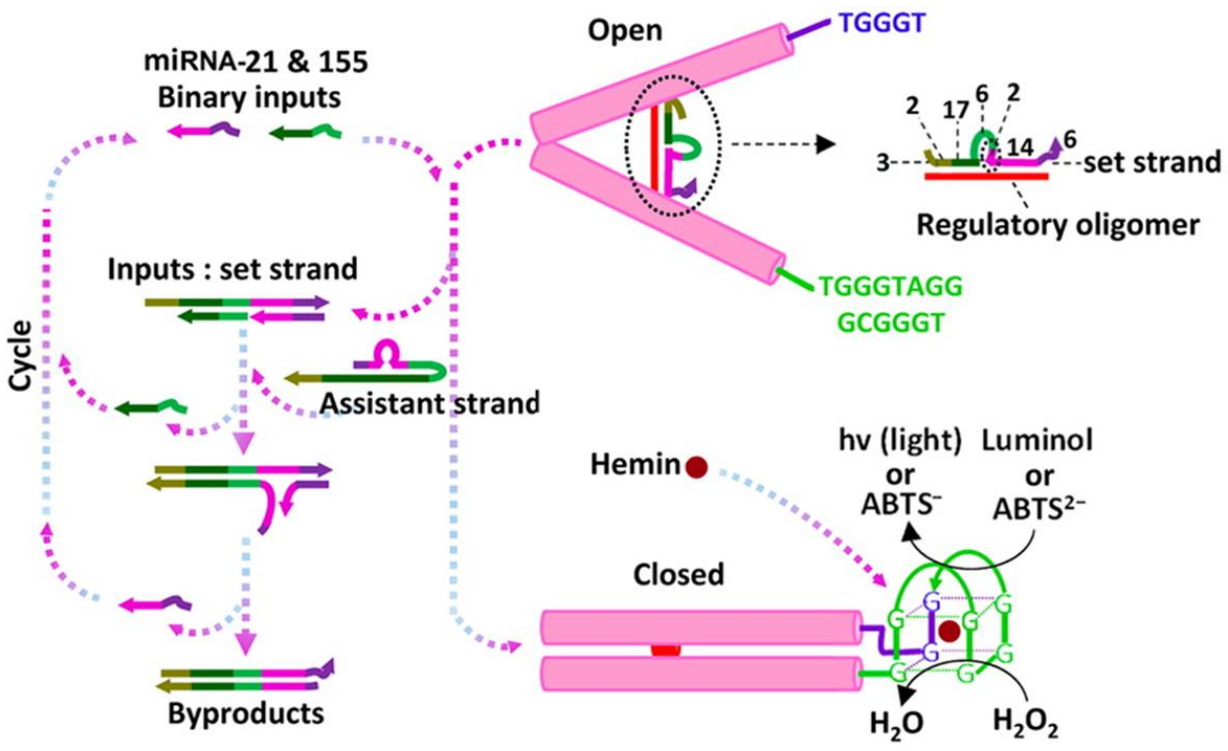

Figure 1.8 AND gate actuated nanotweezers with a split-DNAzyme. MiRNA inputs displace the *set* strand, allowing the nanotweezers to close and bring the two halves of an HRP-like DNAzyme together, producing a colorimetric signal through the oxidation of $ABTS^{2-}$. Reproduced from Ref. [126] with permission from American Chemical Society.

1.4 Contributions of this Thesis

The development of photonic DNA-based nanostructures with built in Boolean logic operations has the potential to produce efficient sensing devices that provide more direct information than traditional sensors. DNA provides a versatile material for assembling complex devices on the nanoscale, enabling the development of a wide range of logic gates with fluorescent readouts. The efficacy of these logic devices hinges on output states (TRUE and FALSE) with significantly

different signal intensities (*i.e.* signal contrast) to produce a truly binary readout. Work in this thesis primarily focused on the development of fluorescent DNA logic gates to expand the capabilities of this class of device; however, some work focused on the development of QDs for sensing applications.

Chapter 2: details efforts to design and synthesize a DNA-based logic sensor for accurate sensing of active proteases in biological samples. Though the sensor was ultimately not successfully developed, the attempted optimization of the structure-switching aptamer design revealed important theoretical limits on the design of this type of system.

Chapter 3: and Chapter 4: focused on the development of design strategies for non-enzymatic amplification of fluorescent output signals from DNA logic gates. This amplification is a valuable tool for the construction of logic devices with high signal contrasts. Achieving amplification without the use of enzymes allows for more versatile systems that are not constrained by the conditions required for enzyme activity. Both systems made use of hidden toeholds to produce chain reactions of DNA displacement, bringing many fluorophores into proximity and producing an amplified FRET signal. Chapter 3: describes the synthesis and testing of a novel displacement cascade logic gate. Chapter 4: describes attempts to implement a DNA walker design using different DNA hairpins conjugated to a central QD. These studies represent important steps towards the synthesis of logic gates with high signal contrast using these novel non-enzymatic ligation techniques.

Chapter 5: focused on the development of a different type of QD-based sensor using small molecule ligands rather than DNA to coat the QDs. This project made an important contribution to the ongoing development of a library QD surface ligands that affect the activity of proteases at

the surface of QDs. The three ligands developed here will ultimately contribute to the development of a QD-based sensor array for the differentiation of proteases.

Chapter 2: AND Gate Protease Logic Probe

2.1 Logic Probe Design

Proteases are important signalling molecules for many biological processes in both healthy and diseased cells. This importance has led to interest in proteases as biomarkers for diseases including inflammatory diseases [129] and cancers [130] among others. The activity of proteases is strictly regulated within organisms, meaning that both the presence and activity of protease biomarkers are important for disease diagnosis [131]. An ideal protease sensor would therefore determine both the concentration *and* activity of a protease in a biological sample. Sensors typically generate a signal by binding to a protease (where signal increases with concentration), or through the proteolytic hydrolysis of a substrate peptide (where signal increases with activity). The aim of this project was to design and construct a DNA-based sensor that combined these functions.

To accomplish this goal, a logical AND gate sensor was proposed where a single logical output indicates the presence *and* activity of the target protease (Figure 2.1). This sensor design would also function to lower the error rate by eliminating false positive results caused by binding of a non-target protein, non-specific hydrolysis of the substrate peptide, or probe degradation. The proposed sensor uses a FRET-sensitized fluorescent signal as a TRUE output. Specifically, the signal is generated by a fluorescent organic dye after FRET sensitization from a luminescent lanthanide complex (LLC). The long luminescent lifetime of the LLC enables the use of a time-gated measurement, where a short time lag, typically microseconds, between excitation and signal measurement is used to avoid collection of short-lived background signals (*e.g.* autofluorescence).

The sensor is actuated by removal of two quencher molecules conjugated to biomolecules that interact with the protease (Figure 2.1). One quencher is conjugated to a DNA aptamer that is hybridized to a template oligonucleotide in the sensor's initial configuration. Binding of the aptamer to the protease releases it from the template strand, thereby removing the quencher from the FRET radius of the LLC and fluorescent dye. The second quencher is located on the distal end of the of the substrate peptide for the protease. Cleavage of this peptide by the protease releases the quencher-labelled end, thereby removing the second quencher from the FRET radius of LLC. Only in the case where both of these events occur (*i.e.* both quenchers are removed from the structure) is a time-gated FRET-sensitized fluorescent dye signal produced (Figure 2.1e). In the cases of non-specific peptide cleavage (Figure 2.1c) or non-specific aptamer dissociation (Figure 2.1d), no FRET sensitized signal is produced as one of the quenchers remains in proximity with the LLC.

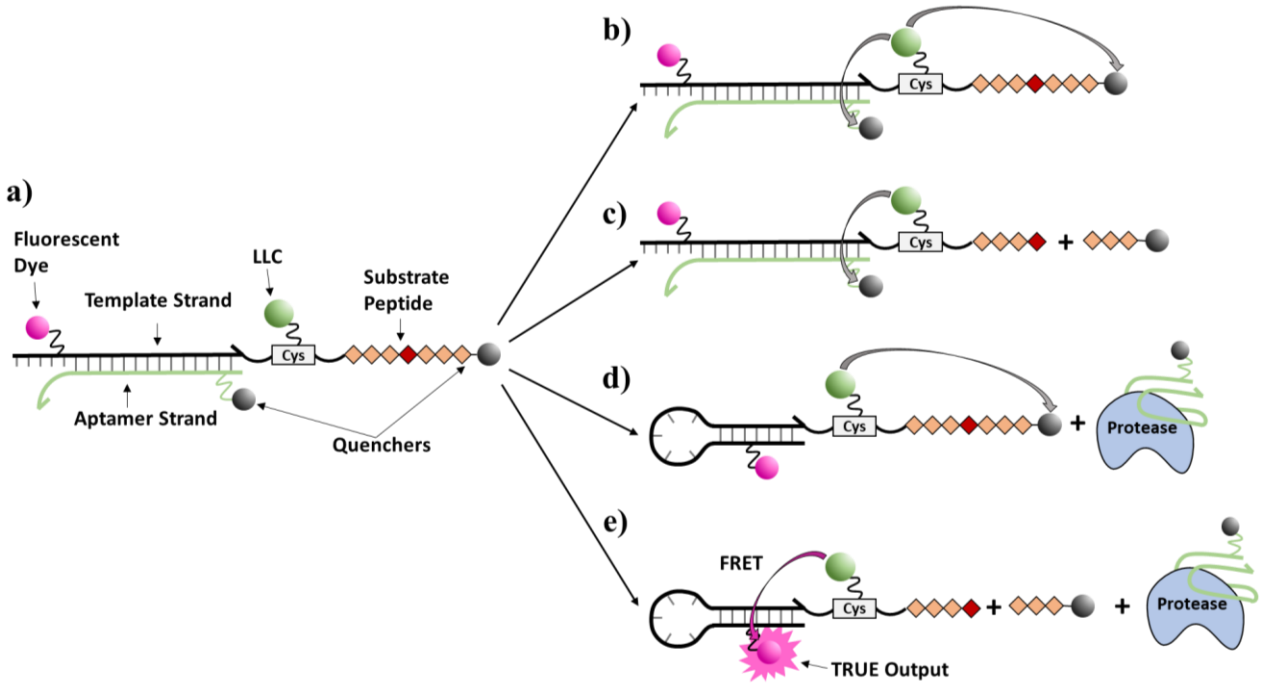

Figure 2.1 AND gate protease logic probe design and expected outcomes. The logic gate generates a FALSE response with **(a)** no protease interaction, **(b)** non-specific peptide degradation, or **(c)** aptamer binding of the inactive protease. A TRUE output is only generated in the **(e)** presence of the active protease, where aptamer binding and peptide hydrolysis both occur.

Thrombin was chosen as a target protease for proof of concept of the sensor design. Thrombin is a serine protease that is integral in the blood clotting cascade [132], and its activity has been shown to be a biomarker for various cancers [133] and neurological disease [134], among others. Importantly, the peptide substrate is well known and characterized and there are several established aptamers for thrombin, making it an ideal model protease for development. Once validated with thrombin, the generalized sensor design could be implemented for other clinically relevant proteases such as prostate specific antigen or a matrix metalloproteinase. Adaptation of the sensor

design to a different target protease would require substitution of the substrate peptide and the aptamer and template oligonucleotides with new sequences.

2.2 Synthetic Approach

The proposed synthetic approach (Figure 2.2) for the biosensor utilizes a series of efficient reactions to conjugate the various components of the system. The C- and N-termini of the peptide provide suitable reactive sites for conjugation reactions. The inclusion of a cysteine amino acid at the N-terminus end of the peptide sequence provides an additional reactive site (*i.e.* thiol group) for conjugation to the peptide. The cysteine can be used as the central unit to which the different components of the structure are conjugated. The cysteine is placed at the N-terminus of the substrate peptide sequence, leaving two exposed reactive sites (the N-terminus amine and the side chain thiol) to specifically attach the template oligonucleotide and the LLC. The designed oligonucleotide was synthesized with two unique functional groups, enabling specific conjugation of the fluorescent dye and attachment to the peptide chain. The fluorescent dye (MB™ 543), quencher (Black Hole Quencher 2®; BHQ-2), and LLC (Lumi4-Tb terbium(III) cryptate) are all available with reactive groups for conjugation with the biomolecules.

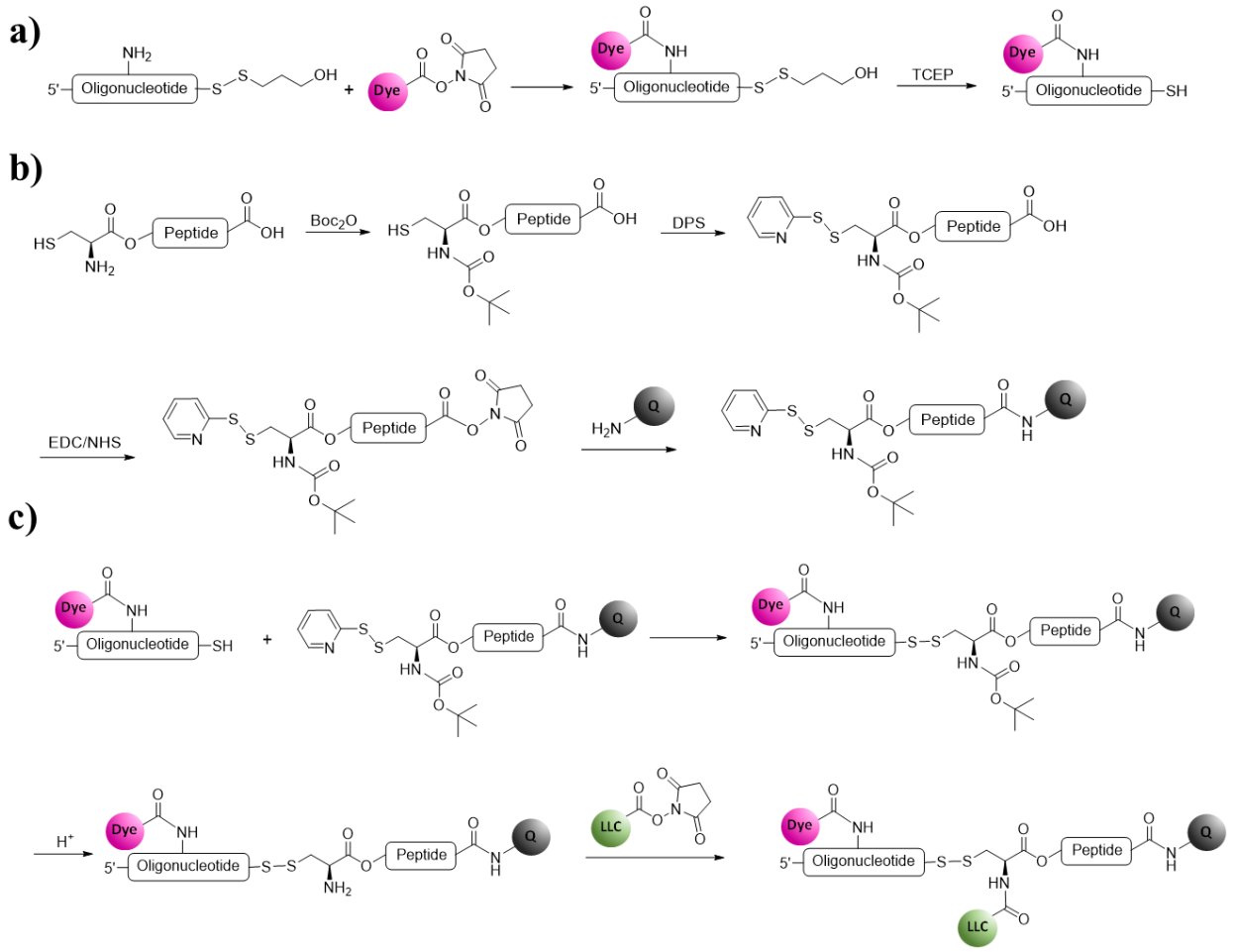

Figure 2.2 Synthetic scheme for the protease logic sensor. **(a)** The oligonucleotide is dye labelled and the dithiol is reduced. **(b)** The peptide is labelled with a quencher and the active groups are protected. **(c)** Finally, the oligonucleotide and peptides are conjugated, and the product is labelled with the LLC.

The biomolecular components of the sensor require conjugation reactions to be carried out under mild and aqueous conditions. These reactions also need to be high yielding to achieve a reasonably efficient overall synthetic pathway. The synthetic design for the sensor was therefore developed with a minimum of steps mainly employing two nominally effective bioconjugation reactions (Table 2.1). The first of these reactions is the coupling of a primary amine to an activated ester.

N-hydroxysuccinimide (NHS) is commonly used to activate carboxylic acids, forming a highly reactive NHS ester. The reaction between NHS esters and primary amines creates stable amide linkages, and this chemistry is used extensively for labelling of biomolecules [135]. Many fluorescent dyes and quenchers are available in the form of NHS esters to allow for facile labelling of amine-containing targets. The second main reaction used in this design is coupling of two sulfur groups via thiol-disulfide exchange. In this reaction, the thiol attacks a pyridyl disulfide, with the pyridyl thiol acting as a leaving group and converting to a non-reactive species preventing the reverse reaction [135]. Thiols are common reactive tags for dyes and oligonucleotides and the thiol of cysteine is a natural target for this reaction. In addition to these two reactions, protection of the peptide with tert-butyloxycarbonyl (Boc) is necessary to prevent unwanted side reactions during conjugation steps. The synthetic plan was designed such that conjugation of the most expensive/difficult to synthesize components was completed as late as possible to minimize the losses. As such, the final step is the conjugation of the LLC to the otherwise completed biosensor structure.

Table 2.1 Stepwise synthetic plan for the construction of the protease logic sensor. (EDC; 1-Ethyl-3-(3-dimethylaminopropyl)carbodiimide, Ni-NTA; Ni^{2+}-nitrilotriacetic acid)

Step #	Function	Method
1	Dye labelling of oligonucleotide	NHS ester-amine reaction
2	Purification of dye-labelled oligonucleotide	Size exclusion chromatography
3	Peptide N-terminus protection	Boc addition
4	Peptide Cysteine thiol protection	Disulfide-thiol exchange
5	Peptide C-terminus activation	EDC/NHS activation
6	Quencher labelling of peptide C terminus	NHS ester-amine reaction
7	Purification of quencher labelled peptide	Ni-NTA agarose
8	Oligonucleotide-peptide conjugation	Disulfide-thiol exchange
9	Peptide N terminus deprotection	Boc removal
10	LLC labelling	NHS ester-amine reaction
11	Purification of logic sensor	Size exclusion chromatography

2.3 Aptamer Duplex Design

The first step in validating the proposed sensor was to test the structure-switching aptamer duplex design. There are several established thrombin aptamers with different binding modes and affinities [136]. Initially, the HD-22 aptamer was chosen due to its higher binding affinity. HD-22 is a 29 nucleotide long thrombin aptamer that was first developed through the SELEX process in 1997 [137]. When bound to thrombin the aptamer has two structurally distinct sections, a duplex and a G-quadruplex, both of which are involved in the binding interactions with thrombin [138]. Binding of the aptamer has some effect on the proteolytic activity of thrombin but does not fully inhibit its activity. Reported dissociation constants (K_D) for HD-22 range from 0.65 nM [139] to ~100 nM [140].

To construct the first part of the logic sensor, the interactions between thrombin and a DNA duplex containing the HD-22 aptamer were investigated. The design of the oligonucleotide that hybridizes with the aptamer, referred to here as the *template* strand, is a critical part of the logic sensor design. The hybridization must be strong enough to ensure the oligonucleotides are in duplex form at room temperature but not too strong such that the hybridization prevents binding of the aptamer to thrombin. The initial template was designed to produce a duplex with a minimum melting temperature (T_m) while retaining >95% duplex form under the starting conditions (typically 25 °C, 0.1 μM DNA in Tris buffer with 30mM Na^+ and 0.5 mM Mg^{2+}, pH 7.5) to produce a low background signal. The structure-switching template was designed to form a hairpin structure upon dissociation of the aptamer, where the hairpin formation served two purposes. Firstly, formation of the hairpin was hypothesized to encourage binding of thrombin by the aptamer by reducing the increase in overall free energy of the system caused by the dissociation of the duplex. Secondly, the rigid duplex of the hairpin reduces the freedom of movement of the fluorescent dye conjugated to the template strand. The behaviour of random-coil DNA in solution is, by nature, less predictable, and the exact position of a dye conjugated to a single-stranded oligonucleotide is not consistent nor easily determined. However, a dye conjugated to an oligonucleotide in a duplex gives a fixed distance between the dye and the central LLC in the sensor, producing a more consistent FRET signal. Previous work in our group has revealed a 'sweet spot' for the distance between an LLC and a FRET acceptor for time-gated FRET measurements with high signal-to-noise ratios [141]. The formation of the hairpin allows the FRET acceptor dye to be fixed at this 'sweet spot' distance, in principle improving the fluorescent performance of the device. This fixed distance also avoids the non-specific interactions between the fluorescent dye and the LLC which have been observed in prior work [142].

Initially, low-cost fluorescent labels were used with the oligonucleotides to test the efficacy of the structure-switching template-aptamer duplex. The template and aptamer were labelled with a FRET pair of fluorescent dyes, 6-carboxyfluorescein (FAM) and cyanine-3 (Cy3), respectively, to enable observation of their hybridization status. When hybridized, FRET caused significant quenching of the FAM signal and sensitization of the Cy3 signal (Figure 2.3a). In experiments, the template was hybridized to the aptamer and dissociation of the duplex in the presence of thrombin was measured at different concentrations and in a variety of buffers. At room temperature, no binding with thrombin was observed. At 37 °C, some dissociation of the duplex due to thrombin binding was observed, with the degree of dissociation increasing with thrombin concentration. Even with five equivalents of thrombin, however, less than 20% of the duplex was dissociated (Figure 2.3b). The proper functioning of the logic sensor would require the duplex to fully dissociate in the presence of thrombin, ideally at room temperature.

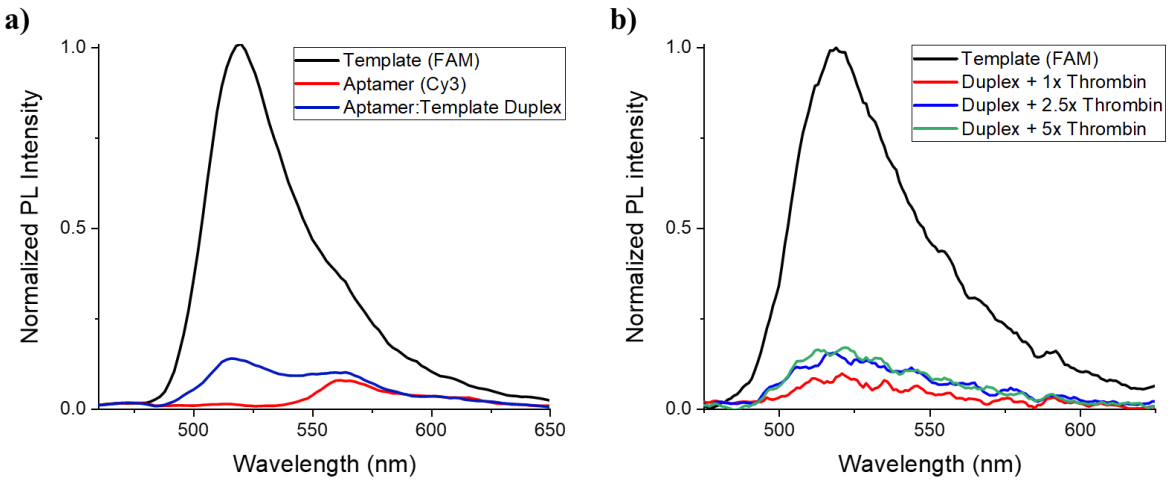

Figure 2.3 HD-22 duplex dissociation with thrombin by fluorescence (excitation at 440 nm). **(a)** Hybridization of the aptamer and template oligonucleotides led to significant quenching of the FAM signal (emission maximum at 512 nm). **(b)** Addition of thrombin to the duplex resulted in some dissociation of the duplex, measured by restoration of the FAM signal.

Based on these results, the template was redesigned to produce a less stable duplex encouraging dissociation and therefore leading to more efficient thrombin binding. To allow for testing of multiple template designs with minimal costs, unlabelled oligonucleotides were used and dissociation of the duplex/formation of the aptamer-thrombin complex was monitored by capillary electrophoresis (CE). Five different templates were designed (Table 2.2), forming duplexes with calculated T_m values ranging from 23.5 °C to 33.5 °C under the testing conditions (0.1 μM DNA in Tris buffer with 30mM Na^+ and 0.5 mM Mg^{2+}, pH 7.4). Three of these templates included mismatched bases within the duplex-forming segment of the oligonucleotide to destabilize their hybridization with the aptamer. The other two templates contained segments to hybridize with two separated regions of the aptamer sequence. The hypothesis with these templates was that leaving

the thrombin binding region of the aptamer unhybridized would allow it to interact with the protease more readily.

Table 2.2 Sequences of HD-22 and template oligonucleotides. Segments of the template sequences that hybridize with the aptamer are bolded and mismatched bases within these segments are in red. T_m values for the duplex formed between the aptamer and the given template were calculated using DINAMelt [143] at conditions approximating the intended experimental conditions (0.1 μM DNA with 30mM Na^+ and 0.5 mM Mg^{2+}).

Name	Sequence (5'-3')	Calculated Duplex T_m (°C)
HD-22 Aptamer	AGTCCGTGGTAGGGCAGGTTGGGGTGACT	-
Complementary	TAAATTGTGGTAAAA**CCCTACCACGGACT**	37.0
Single Mismatch	TAAATTGTGGTAAA**GCCGTACCACGGACT**	29.5
Double Mismatch	TCCGTAAAAGTAA**TGCGCTACGACGGACT**	23.5
Double Mismatch (short HP)	TCCGAATAGGTAA**TGCGCTACGACGGACT**	26.5
Pinched (6 bp)	**AGTCAC**AAAAA**ACCACGGACT**	27
Pinched (7 bp)	**AGTCACC**AAAA**ACCACGGACT**	33.5

The single-stranded oligonucleotides, DNA duplexes, and aptamer-thrombin complexes were all readily separated and detected by CE with UV detection. The template oligonucleotides were annealed with the aptamer strand then measured by CE. This experiment revealed very limited hybridization with the aptamer for four of the five template strands (Figure 2.4a). The *single mismatch* template did form a relatively stable duplex with the aptamer with ~85% of the DNA in duplex form as determined by CE peak areas. This duplex was measured after incubation with increasing amounts of thrombin (0.5-2.0 equivalents) and the ratio between the peak area of the aptamer-thrombin complex and the DNA duplex was measured (Figure 2.4b). At two equivalents

of thrombin, only ~20% of the aptamer was bound to thrombin, with the rest remaining hybridized to the template (Figure 2.4c).

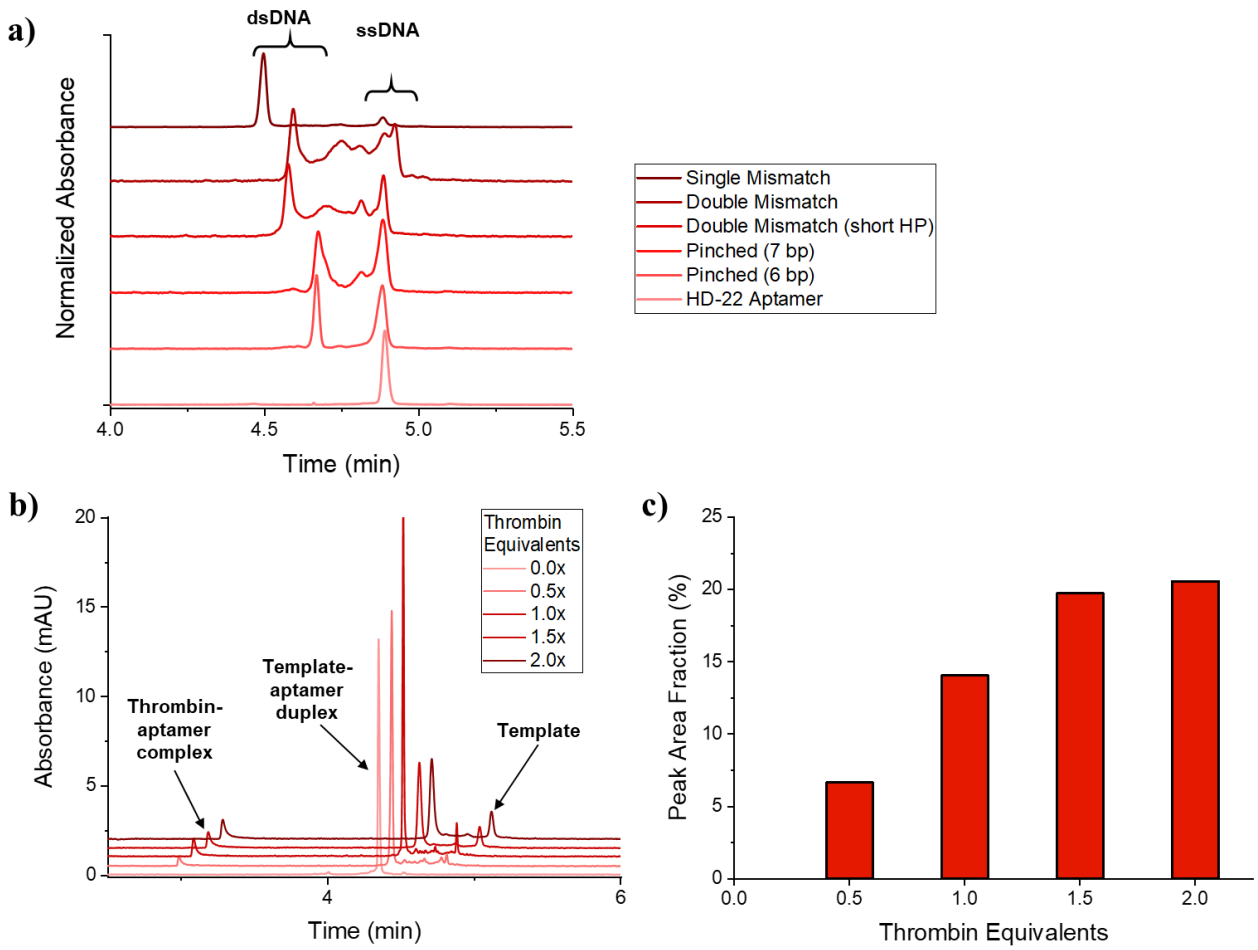

Figure 2.4 HD-22 duplex dissociation with thrombin by capillary electrophoresis (absorbance at 260 nm). **(a)** CE chromatograms showed incomplete hybridization between the template and aptamer oligonucleotides for most of the template designs, with the single mismatch template displaying nearly complete hybridization. **(b)** The single mismatch template-aptamer duplex peak decreased as the thrombin-aptamer complex peak and the template oligonucleotide peak increased with increasing equivalents of thrombin. **(c)** The relative peak area of the aptamer-thrombin complex increased with increasing concentration of thrombin but remained relatively low (20% of the total) even with 2.0 equivalents of thrombin.

The investigation of the different template strands revealed an issue with the use of this aptamer for the logic probe: even with a very low calculated T_m and an excess of thrombin, dissociation of duplex was incomplete. To achieve a binary signal at low concentrations of thrombin, a duplex that will readily dissociate is critical. The reason for this low binding efficiency was hypothesized to be a result of the nature of the structure of the aptamer. Hybridization of parts of the active regions of the HD-22 aptamer by the template oligonucleotide may have interfered with the interactions between the aptamer and thrombin. Though the structure of the HD-22-thrombin complex is well known, the mechanism of its binding is less well understood. The aptamer may, for example, need to undergo the structural rearrangement to form a G-quadruplex before it binds to thrombin, and hybridization to the template strand may sufficiently inhibit this process to significantly affect the binding to thrombin. A second simpler aptamer, which is the 15-mer thrombin aptamer HD1, was investigated next to see if it would produce a duplex more suitable for use in the logic probe.

The HD1 aptamer, originally published in 1992 [144], was one of the earliest aptamers discovered after the development of SELEX in 1990. This aptamer has been shown to selectively interact with exosite I of thrombin (and prothrombin) [145]. Binding of the aptamer inhibits some of the proteolytic activity of thrombin [146] but does not reduce the ability of the proteases to specifically cleave short peptide sequences [147]. HD1 forms a single anti-parallel G-quadruplex that is responsible for the binding to thrombin [148]. The dissociation constant (K_D) of HD1 is ~100nM, which is significantly lower than that of HD-22 [136]. This aptamer has been used extensively in molecular beacon systems for real-time fluorescent detection of thrombin [149]. It was

hypothesized that the simpler binding mode would lead to more complete dissociation of the template-aptamer duplex, and therefore be a better candidate for use in the logic probe.

Three templates were designed to provide duplexes with T_m values ranging between 31 and 39 °C (Table 2.3). The templates varied in the number of base pairs in their duplexes with the aptamer and in the number of duplex base pairs in their self-hybridized hairpin form. Template-aptamer duplex melt curves were measured and were found to match the theoretically calculated melt curves (Figure 2.5a). The dissociation of the template-aptamer in the presence of thrombin was then measured. CE proved to be ineffective for detecting thrombin and HD1 binding as the complex eluted as a very broad peak with low absorbance. Instead, formation of the thrombin aptamer complex was measured by polyacrylamide gel electrophoresis with silver staining. This provided a qualitative measure to compare the dissociation of the different aptamer-template complexes. The two template strands with internal mismatches both showed significant dissociation and thrombin binding (Figure 2.5b). Based on this data the *single mismatch* template strand was carried forward to the next stage of the experiment.

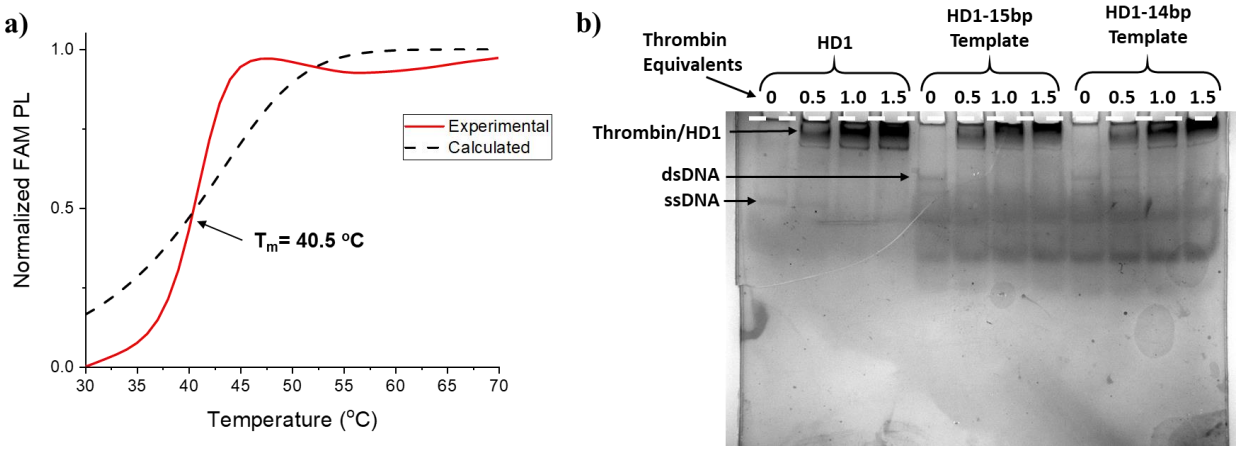

Figure 2.5 T_m determination and template aptamer dissociation by silver-stained PAGE. **(a)** Experimental (by restoration of FRET quenched FAM signal) and theoretical T_m determination for *16-bp* template (10 µM DNA, 20 mM tris buffer with 10 mM NaCl). **(b)** Silver-stained PAGE analysis of template-aptamer dissociation in the presence of thrombin.

Table 2.3 Sequences of HD1 and template oligonucleotides. The aptamer sequence is underlined, segments of the template sequences that hybridize with the aptamer are indicated in bold, and mismatched bases are in red. T_m values for the duplex formed between the aptamer and the given template were calculated using DINAMelt at conditions approximating the intended experimental conditions (0.1 µM DNA with 30mM Na^+ and 0.5 mM Mg^{2+}).

Name	Sequence (5'-3')	Calculated Duplex T_m (°C)
HD1 Aptamer	GAGGTTGGTGTGGTTGG	-
16-bp Template	G**CCAACCACACCAACCTC**AGTGGTTGGC	38.5
15-bp Template	G**CCAACCACACCAACCT**AAGTGGTTGGC	35.5
14-bp Template	G**CCAACCACACCAACC**AAAGTGGTTGGC	31.0

The *15-bp* template was commercially synthesized with an internal amine linker (Uni-Link™) to allow for conjugation with a fluorescent dye. The HD1 aptamer was commercially synthesized

with Iowa Black® FQ quencher conjugated at the 5' terminus. The template was subsequently labelled at the internal amine linker with Cy3-NHS dye, allowing the duplex formation/dissociation to be monitored by the FRET quenching of the fluorophore. This duplex was tested under a range of buffer and DNA concentration conditions to find the optimal response to thrombin. Under optimized conditions, the duplex was shown to give a linear response to addition of thrombin, with ~75% dissociation at a 40-fold excess of thrombin (Figure 2.6). Though the linear response was promising, this system had a very high background signal due to fluorescence from oligonucleotides already dissociated under the starting conditions. The various conditions tested suggested that achievement of a T_m amenable to competitive binding with thrombin would reduce duplex hybridization to a point where there was significant fraction of unhybridized oligonucleotides under the starting conditions. To aid in design and development of subsequent templates, thermodynamic calculations were used to optimize the duplex and hairpin binding energies.

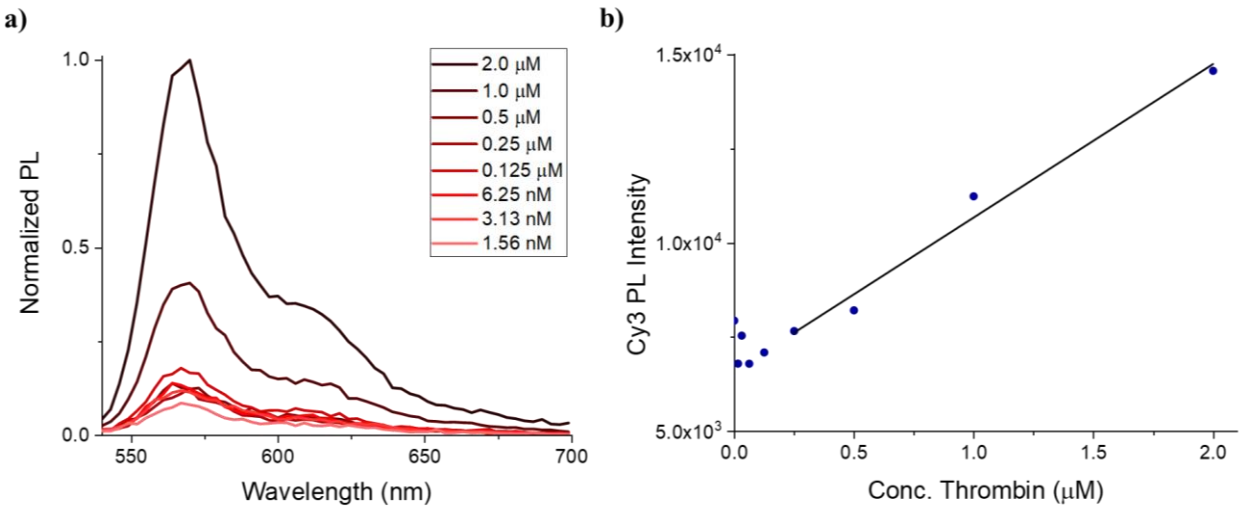

Figure 2.6 Duplex dissociation due to thrombin binding under optimized conditions. **(a)** Raw spectra show increasing Cy3 emission with increasing thrombin concentration, with a **(b)** linear response from 0.25 μM to 2.0 μM: 50 nM DNA duplex in 20 mM Tris buffer (pH 7.4) with 100 mM KCl, reacted overnight at room temperature (excitation at 520 nm).

A theoretical survey of many different strand designs was conducted to determine the relationship between the T_m of the system and the change in free energy (ΔG) between the duplex and hairpin conformations (

Figure 2.7). The thermodynamic calculations were performed using the UNAfold webserver which calculates predicted parameters for an oligonucleotide or pair of oligonucleotides based on their sequence, concentration, and buffer conditions [150]. The length and A:T vs G:C content of both the duplex forming region and the hairpin forming region of the theoretical template oligonucleotides were varied (see Table A2 and Table A2 for full list of tested sequences and design parameters). Additionally, the length of the non-hybridized hairpin loop segment was

varied. Template strands were also designed for aptamer sequences with a domain added to facilitate optimization of the hybridization properties of the oligonucelotides. The T_m and ΔG values were determined at fixed conditions (1.0 μM DNA in 100 mM Na^+ and 0.5 mM Mg^{2+} at 25 °C) that closely matched the preferred experimental conditions. The tested sequences were rationally designed to give a range of representative data points. The system T_m was plotted versus the difference in ΔG between the duplex and hairpin forms of the template (or the 'ΔΔG'). Importantly, experimental ΔG values for the binding of HD1 to thrombin are reported at –8.8 kcal/mol [151]. This indicates that for an aptamer-template duplex to substantially dissociate in the presence of thrombin its ΔΔG value (*i.e.* the energy penalty for duplex dissociation) would have to be < +8.8 kcal/mol.

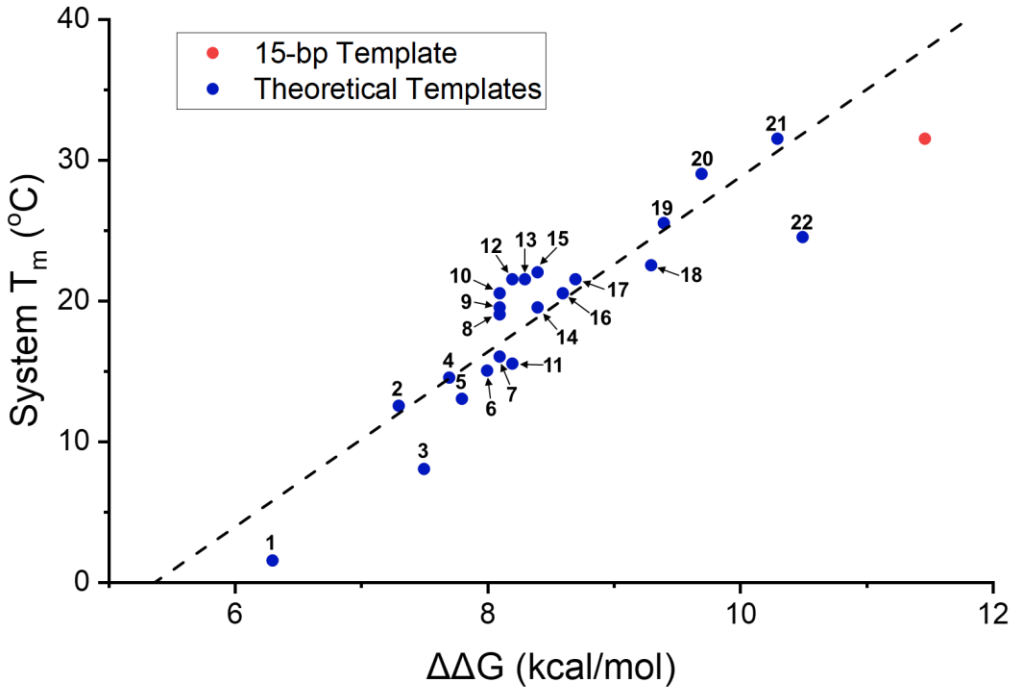

Figure 2.7 Theoretical survey of template designs. Calculated T_m for aptamer:template duplexes versus the difference between the calculated free energy values of the duplex and hairpin conformations. Calculations were performed using the UNAFold web server [150]. See Table A2 and Table A2 for full list of tested sequences and design parameters.

2.4 Conclusions

Based on this theoretical survey, the energy of the HD1-thrombin binding is not sufficient to provide the driving force for the dissociation of a duplex that is fully stable at room temperature. The inclusion of a hairpin structure in the template design necessitates the formation of a duplex with relatively strong hybridization to favour the duplex formation over self-folding. In turn, this strength of hybridization reduces the ability of thrombin to disrupt the duplex. Designs in which the $\Delta\Delta G$ of the aptamer-template complex was below the ΔG of the HD1-thrombin interaction (*i.e.* in which the aptamer would readily dissociate to bind thrombin) had a $T_m < 25$ °C and would therefore be unstable at room temperature. A system of this type would need to be constructed with a template that did not form a hairpin and with less complementary bases between the template and the aptamer. Indeed a survey of similar systems revealed that none included a hairpin design in their template strands [152–158]. As the hairpin was required in the design of this logic sensor, the project was deemed unviable and abandoned. A different implementation of the overall concept may be explored in future research.

2.5 Experimental Methods

Materials: Native and modified (labelled with cy3, FAM, or Iowa Black® FQ quencher, or containing an internal uni-link) oligonucleotides were custom synthesized and purified by PAGE

or HPLC by Integrated DNA Technologies (Coralville, IA). Cyanine 3 NHS ester (cy3-NHS) was from Lumiprobe (Hallandale Beach, FL).

Instruments: PL and absorption spectral measurements were made with an Infinite M1000 Pro plate reader (Tecan Ltd., Morrisville, NC). Gel images were collected with a Gel Doc XR+ Gel Documentation System (Bio-Rad Laboratories Ltd., Hercules, CA). ImageJ software (NIH, Bethesda, MD) was used for processing images. Capillary electrophoresis analysis was done with an Agilent 7100 CE system (Agilent Technologies Inc., Santa Clara, CA).

DINAMelt calculations: All thermodynamic calculations for DNA were conducted using DINAMelt through the UNAFold web server [150]. DINAMelt online software provides thermodynamic parameters for oligonucleotides, and T_m values for systems with two oligonucleotides, based on input sequences, concentrations, buffer conditions, and temperatures [143].

NHS-ester dye labelling: Oligonucleotide samples dissolved in nuclease-free water were dried by vacuum centrifugation in 1.5mL microcentrifuge tubes. Dried samples were resuspended to 100 μM in 100 mM sodium bicarbonate buffer (pH 8.2) and cooled on ice. Ten molar equivalents of the dye NHS-ester (dissolved in DMSO) were diluted with DMSO to a final volume of one-quarter the total intended reaction volume and added to the oligonucleotide solution. The reaction was covered from light and briefly vortexed and centrifuged before being placed back on ice for 5 min. The reaction mixture was then covered to protect from light and placed on a rotating mixer and mixed overnight at room temperature. After the reaction, the oligonucleotide was isolated by ethanol precipitation. The reaction mixture was diluted ~2.5X with water and 3 M sodium acetate to a final concentration of 0.5 M sodium acetate. Three volumes of ethanol were added to this

mixture for a final composition of 75% ethanol, and the solution was incubated at –20 °C for at least 4 h. The mixture was then centrifuged at 17 000 RCF for 30 min and the supernatant was discarded. Finally, the pellet was rinsed with 70% ethanol and then left to air dry for 20 min to remove residual solvent.

Displacement tests with fluorescent measurements: Equimolar amounts of template and aptamer oligonucleotides were mixed in the chosen buffer, typically *DNA hybridization buffer* (20 mM Tris, 10 mM NaCl, 0.5 mM $MgCl_2$, pH 7.4). The mixture was annealed by heating to 94 °C for 5 min and slowly cooling to room temperature. The annealed duplex was diluted to the working concentration (typically 50–500 nM) and combined with thrombin. The mixture was incubated at room temperature or at an elevated temperature in a heating block for a set amount of time before being transferred to a 96-well plate. Fluorescence measurements were conducted using an Infinite M1000 Pro plate reader (Tecan Ltd., Morrisville, NC).

Capillary electrophoresis (CE): DNA samples were diluted to 5-10 μM in *DNA hybridization buffer*. Samples were mixed with 0-2.0 molar equivalents of thrombin and incubated at room temperature for 1 h. Samples were injected (1-5 μL) onto the capillary and eluted isocratically with borate buffer (20 mM, pH 8.5).

Polyacrylamide gel electrophoresis (PAGE): A 7.5 mL-solution of the desired concentration of acrylamide/bis-acrylamide (37.5:1) solution was made by diluting an appropriate volume of 40% w/w stock into 1X TBE. The solution was degassed under vacuum for 30 min. To the degassed solution, 7.5 μL of tetramethylethylenediamine and 30 μL of 25% w/v ammonium persulfate (aq) were added. The solution was gently mixed before being transferred to a vertical gel caster and

left to set at room temperature for 1–2 h. Samples were diluted to 10 μL with a final concentration of 25% v/v glycerol before loading onto the gel. Gels were run with 1X TBE as the running buffer.

Ethidium bromide staining: After running, gels were removed from the cast and submerged in 1X TBE with 0.5 μg/mL ethidium bromide. The solution was gently mixed for 15–30 min before imaging with the Gel Doc XR+ under UV illumination.

Silver staining: A standard protocol was followed for the silver staining of polyacrylamide gel [159]. Briefly, gels were submerged in fixer solution of 7.5% v/v glacial acetic acid for 10 min. The gel was then washed three times with deionized water and transferred to a solution of 15% v/v formaldehyde for 10 min. Following removal of the formaldehyde solution, the gel was submerged in a 10 mg/L $AgNO_3$ (aq) solution for 20 min for silver impregnation. After a brief rinse with deionized water, the silver impregnated gel was developed in a cold solution of 30 g/L Na_2CO_3 (aq) with 2 μg/mL sodium thiosulphate for ~2 min. Finally, the gel was transferred to a cold 7.5% v/v glacial acetic acid solution for 10 min to stop the development before washing with deionized water. The stained gel was imaged with white light epi-illumination on a Gel Doc XR+ system.

Chapter 3: Displacement Cascade Logic Gate Amplifier

3.1 Logic Gate Amplification

A common shortcoming of fluorescent logic gates is low contrast between TRUE and FALSE logic outputs. In a traditional logic gate design, inputs produce a change in the logic gate structure (*i.e.* displacement of an oligonucleotide in a duplex), which, in turn, leads to a change in fluorescent signal (*i.e.* increase of a FRET signal). The signal output in this model is fundamentally limited as a single set of inputs can only produce signal from one fluorophore. Logic gates that produce multiple copies of an output from a single set of inputs are desirable. This type of system would, in theory, have a much larger contrast between the TRUE and FALSE output states. Amplification of outputs would also improve the ability of DNA logic gates to work in circuits by increasing the concentration of inputs for the downstream logic gates. The following project focused on the design and construction of fluorescent DNA logic gates with output signals amplified by cascading displacement reactions.

3.2 Displacement Cascade Logic Gate Design

This project aimed to design and synthesize a DNA-based logic gate that amplifies fluorescent signal through a chain reaction of oligonucleotide hybridization events. The design of the device is based on the use of hidden toeholds to produce a cascading displacement reaction. The cascade is initiated by the uncovering of the first toehold in the sequence through the hybridization of logical inputs to a terminal *gate* unit. FRET between fluorophores on a long *amplifier* strand comprising many short repeating segments (*backbone units*) and on *reporter* oligonucleotides acts

as the fluorescent output signal. The presence of many repeating fluorophore-containing segments activated by a single logic gate unit theoretically allows for many-fold amplification of the output signal with respect to the amount of input. The logic gate can be described as the combination of two main components: the *gate* unit, which produces the Boolean logic function; and the *amplifier* unit, which generates the fluorescent signal (Figure 3.1). The *gate* segment forms a hairpin at one terminus of the structure. The sequence of this segment, and the corresponding inputs, could be modified to produce a variety of logic functions without modifying the other components of the system.

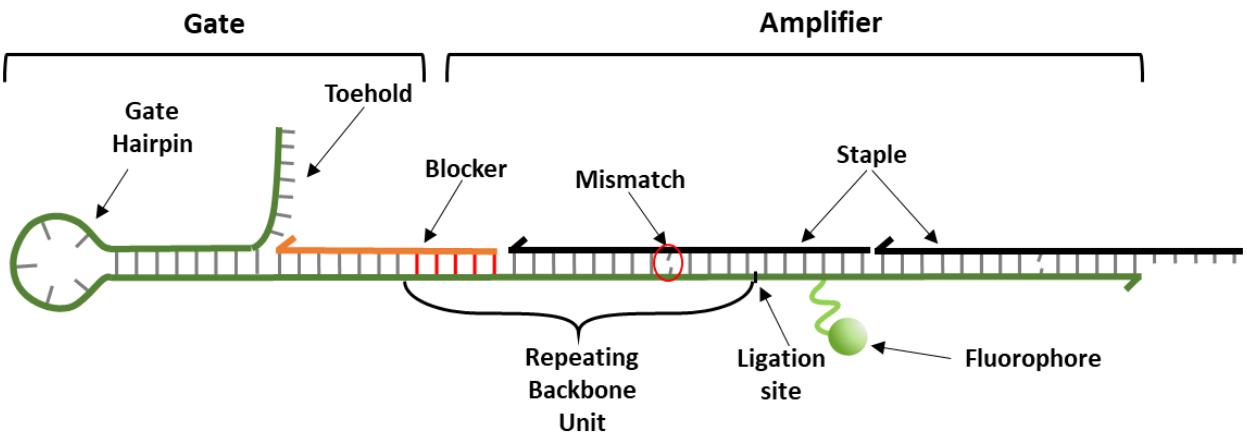

Figure 3.1 Design of the logic gate shown with two repeating *backbone units*, the first of which is incorporated in the *gate* oligonucleotide (see Figure 3.3 for FRET scheme).

An AND gate was used as the model for proof of concept (Figure 3.2). In the AND gate, the *gate* segment includes an independent *blocker* strand that is hybridized to the single-stranded 3' end of the hairpin structure (Figure 3.2a). The *blocker* strand also spans across the first toehold of the

backbone unit and blocks initiation of the displacement cascade. In the AND gate, *input 1* opens the hairpin by binding to the seven-nucleotide toehold at the 5' terminus (Figure 3.2b). This reveals the hidden toehold—previously part of the hybridized stem of the hairpin—for *input 2* to hybridize (Figure 3.2c). Finally, *input 2* displaces the *blocker* strand which subsequently dissociates from the complex, uncovering the hidden toehold of the first *backbone* unit (Figure 3.2d). The actuation of the *gate* unit does not produce a fluorescent signal itself, but instead controls a displacement cascade along the *amplifier* strand which is responsible for the signal generation.

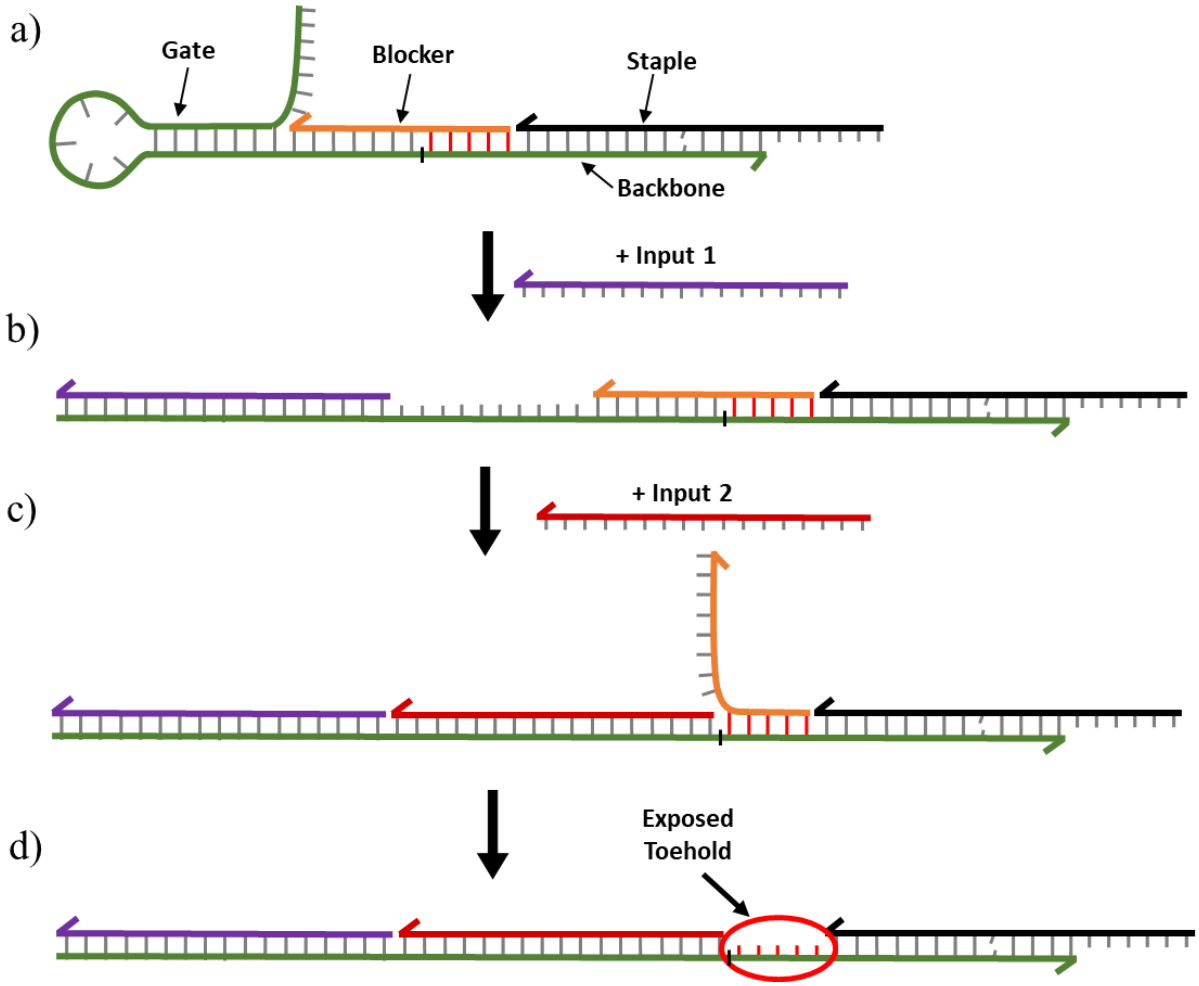

Figure 3.2 Functioning of the terminal AND gate. **(a)** Addition of *input 1* to the initial logic gate system results in **(b)** opening of the terminal hairpin and an exposed toehold. **(c)** *Input 2* then binds to this exposed toehold, partially displacing the *blocker* strand. The remaining five base-pairs between the *blocker* and the *backbone unit* are not strong enough to retain the *blocker*, which **(d)** dissociates from the complex leaving an exposed toehold. The exposed toehold allows binding of the *reporter*, initiating the displacement cascade (see Figure 3.3).

The *amplifier* strand is a long nucleotide made up of repeating segments each labelled with a fluorophore. This long nucleotide is hybridized to many shorter *staple* strands of the same length as the repeating *backbone units*. Finally, dye-labelled *reporter* strands, which are the complements

of the *backbone units*, are free in solution under the starting conditions. The presence of the *staples* is crucial to blocking immediate hybridization of the *reporter* strands to the *amplifier* structure. The *staple* oligonucleotides are largely complementary to the *backbone units* but contain single-base mismatches to lower the overall duplex stability. These mismatches provide a thermodynamic driving force for their displacement by the *reporter* strands. To incorporate hidden toeholds into the design, the sequence of the *staple* strands is shifted by five nucleotides with respect to the repeating unit of the *amplifier*. As a result, the entirety of the *amplifier* strand except for a five-nucleotide toehold region is fully hybridized with the *staple* strands in the initial state (Figure 3.3a).

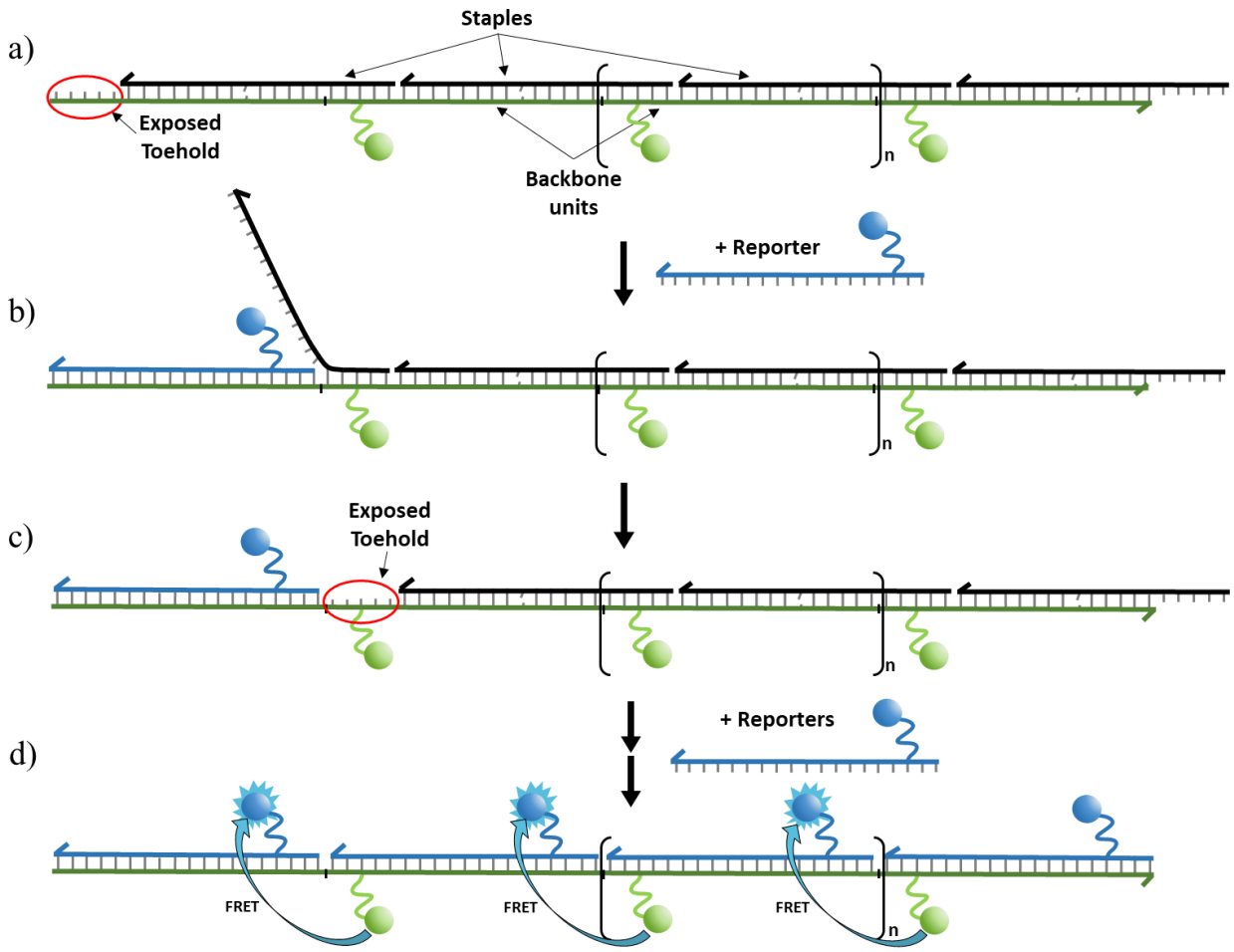

Figure 3.3 Functioning of the *amplifier* to produce the displacement cascade (note: terminal *gate* strand omitted from this diagram for clarity). **(a)** Opening of the AND *gate* results in an exposed toehold, **(b)** to which a *reporter* strand can hybridize. This displaces a *staple* strand, **(c)** leading to a second exposed toehold. **(d)** This process repeats down the chain until the *amplifier* strand is completely hybridized with *reporter* strands, resulting in the amplified FRET signal.

The combination of the AND *gate* and the *amplifier* with the hybridized *staples* and *blocker* comprise the logic gate system. The first toehold of the *amplifier* segment is revealed by actuation of the AND *gate*, initiating the displacement cascade which functions by the following steps. First,

a *reporter* strand binds to the newly exposed toehold and displaces the first *staple* strand on the *amplifier* (Figure 3.3b). This displacement leads to the dissociation of the *staple* strand, thereby revealing a second five-nucleotide toehold region (Figure 3.3c). This state is functionally equivalent to the initial state of the cycle as both leave the system with an identical exposed toehold. Consequently, this process repeats until the *staple* strands have been completely replaced by *reporter* strands (Figure 3.3d), a process which is described as a displacement cascade. Hybridization between the *reporters* and *backbone units* brings their respective fluorophores into proximity. The resulting FRET sensitized fluorescent signal of the *reporter* strand fluorophore is then taken as the logical output signal.

Successful implementation of this design relies on optimization of the synthetic method for construction of the logic gate and the oligonucleotide sequence design. The overall length of the *amplifier* strand is determined by the number of repeating *backbone units* it contains. Due to the length of the *gate* and *amplifier* a logic gate with only three repeating *backbone units* would already be over one hundred bases in length. Direct synthesis of oligonucleotides becomes increasingly difficult at lengths of 100+ base-pairs (bps) as errors during synthesis lead to impurities and diminishing yields [160]. An alternative synthetic method needed to be developed to produce the required DNA nanostructure. Modification of the sequence design was the primary tool for balancing the thermodynamics of the various DNA interactions that are critical to the logic gate function. To provide successful amplification of the logical output signal, the system needs to be stable enough to undergo no displacement under initial conditions but destabilized enough to allow for complete and rapid displacement after addition of the inputs. The following sections will describe the experimental work done and progress made towards realizing this logic gate design.

3.3 Logic Gate Synthesis

The *amplifier* strand required to construct this logic gate was too large to feasibly use traditional solid-phase oligonucleotide synthesis. Instead, enzymatic ligation was used to join the independent repeating units of the structure. The *backbone unit*, *staple*, and *gate* oligonucleotides were commercially synthesized and mixed in the presence of a ligase to construct the logic gate system. The commonly used laboratory enzyme T4 DNA ligase was employed for this project. This ligase efficiently ligates double-stranded DNA (dsDNA) fragments with sticky-ends—short single-stranded (ssDNA) sections that hybridize to the ligation target [48]. Hybridization of the *staple* strand to the *backbone unit* provides the required dsDNA fragments and the five-nucleotide offset of the two sequences provides the sticky-end to produce specific ligation (Figure 3.4). The design requires that only the fluorophore containing *amplifier* half of the duplex is ligated, leaving the *staple* strands as independent oligonucleotides that can dissociated one at a time. To accomplish this, only the *backbone units* were synthesized with phosphoryl groups at the 5' ends—a requirement for successful ligation [49]. As the *staple* strands lack phosphoryl groups at the 5' terminus, they cannot undergo ligation and therefore remain as independent oligonucleotides throughout the reaction.

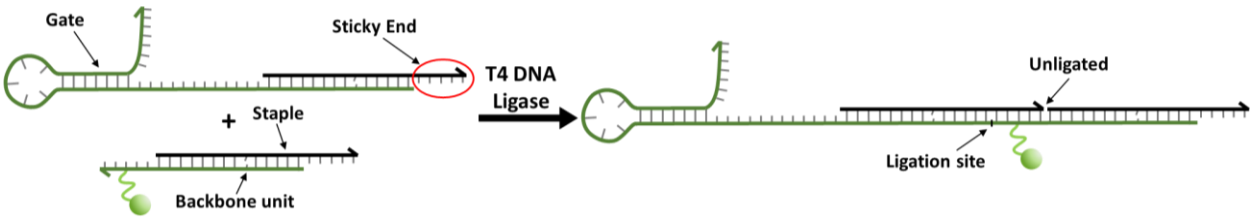

Figure 3.4 Ligation of the first *backbone unit* to the *gate* strand to produce the *logic gate*. The sticky ends caused by the *staple* overhang give specific attachment of the *backbone units*, while the *staple* strand remain independent as they lack the necessary phosphorylation to undergo ligation.

The average length of the *amplifier* strand is controlled by altering the ratio of components added to the ligation mixture. Specifically, the number of *backbone units* per *gate* strand (with the *staple* strand in slight excess relative to the *backbone units*) determines the average length. The 3' end of the *gate* strand is able to join to the 5' end of a *backbone unit* through sticky-end ligation due to the inclusion of a single *backbone unit* segment at the 3' end of its sequence (Figure 3.4). Standard solid-phase oligonucleotide synthesis leaves the 5' end as an alcohol, unlike the 5' phosphate group of naturally occurring DNA. Ligation at the 5' end is not possible due to the lack of this phosphoryl group as well as the lack of sticky end. Addition of a *gate* strand to the terminus therefore effectively terminates the chain growth in the 5' direction. Growth of the nucleotide structure can be thought of as a polymerization reaction with the *backbone unit-staple* duplex as the monomeric unit. The random nature of the addition of monomer units implies that the final products should show a distribution around the average length predicted by the *backbone unit* to *gate* strand ratio. The difference in average length based on the *backbone unit* to *gate* ratio was observed experimentally by polyacrylamide gel electrophoresis (PAGE) (Figure 3.5a). For the purposes of this project, *backbone unit* to *gate* strand ratios of between 5 and 20-to-1 were typically used. For

example, a ligation with a 20-to-1 ratio of *backbone unit* to *gate* strand and a slight excess of the *staple* strand gave a structure with the expected approximate average length of ~400 nucleotides (Figure 3.5b).

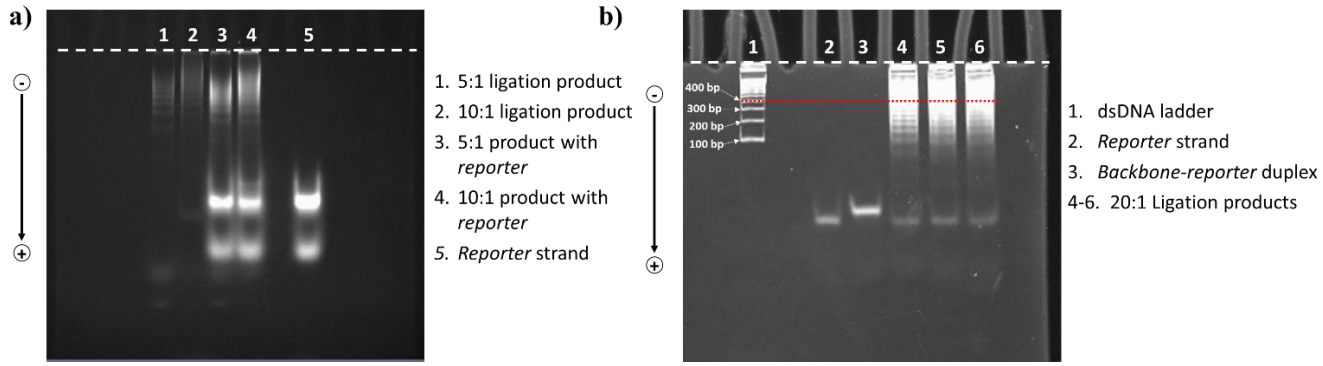

Figure 3.5 PAGE analysis of logic gate systems synthesized through enzymatic ligation. **(a)** Alteration of the *backbone* to *gate* strand ratio results in different average lengths of the ligated product, and **(b)** this average length was found to show a distribution around the values expected based on the oligonucleotide lengths (Note: lanes 4-6 are replicates of the same *logic gate* sample).

Several methods were tested for purification of the ligated *logic gate* system. Firstly, spin filtration with 30 kDa cut-off centrifugal filters was employed to remove excess starting materials and ligase (Figure 3.6a). PAGE purification by electroelution was effective for ligation products without conjugated dyes but gave very low yields when attempted with dye labelled systems, likely due to interactions between the dialysis membranes and fluorescent dyes. Finally, purification by size exclusion chromatography was tested using different resins (Sephacryl s-300 HR and s-100 HR), which proved effective for fractionation of the ligated products (Figure 3.6b). Though effective,

these methods all separate the products based on size rather than sequence. An important aspect of the nominal purity of the product is the proportion of the structures that are capped with a *gate* strand. Uncapped sequences would undergo spontaneous displacement with the *reporter* strand, and their presence must be minimized for optimal functioning of the device. Several different methods were tested to ensure complete 'capping' of the nucleotide structures with the *gate* strand during ligation. These included increased reaction time (up to 5 days), addition of excess *gate* strand after 24 h of reaction, and slow addition of the *backbone unit* to the reaction. Without sequence analysis it is difficult to directly determine the effectiveness of these synthesis strategies. Fluorescence displacement studies (*vide infra*), however, showed better performance (*i.e.* less displacement without the addition of logic inputs) for samples ligated over 5 days and samples with excess *gate* strand added.

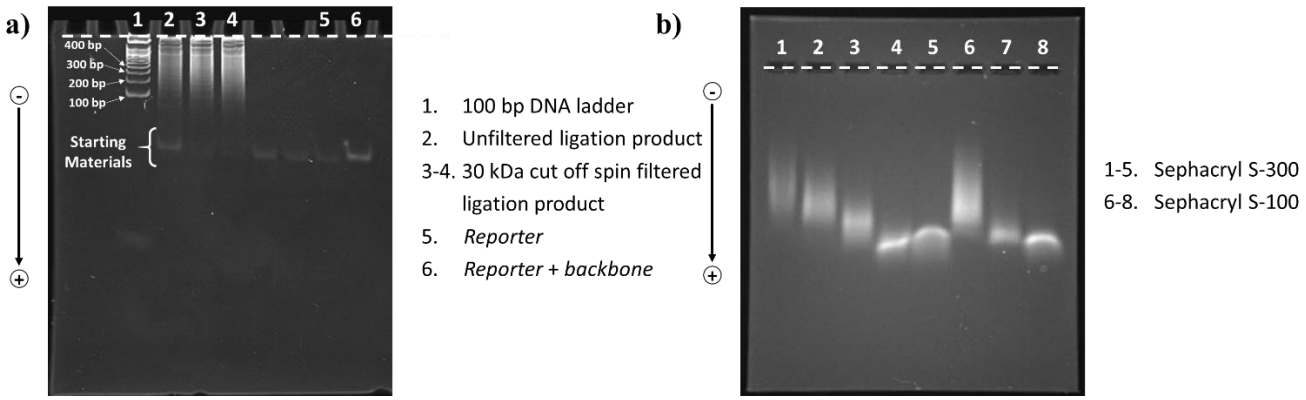

Figure 3.6 PAGE analysis of purification strategies. **(a)** 30 kDa molecular weight cut-off spin filtration was effective for removal of un-ligated starting materials (Note: lanes 3-4 are replicates of the same *logic gate* sample). **(b)** Analysis by agarose gel showed the efficacy of size exclusion chromatography for separation of the logic gate systems based on size, with volume fractions from the S-300 column (lanes 1-5) showing more precise separation than volume fractions of approximately equal volume from the S-100 column (lanes 6-8).

Further optimization of the ligation procedure is necessary to produce a functional logic gate with high signal contrast. Specifically, purification of the ligated structure to eliminate uncapped nucleotides would likely lead to better input response and higher signal contrasts. This goal could be accomplished by specific extraction of nucleotides containing the *gate* sequence with a complementary capture strand tethered to a magnetic bead, with subsequent separation of the product from the bead by heating or addition of a denaturing agent to disrupt the base-pairing (*e.g.* formamide). This option was not pursued at this stage of the project but would be a useful strategy for optimization of the system. Another challenge is to reduce the polydispersity of the ligated product to produce a more uniform displacement response. It was hypothesized that slow addition of the *backbone unit* strand during ligation would lead to nucleotide structures of more uniform size, but this was not rigorously investigated.

3.4 Logic Gate Sequence Optimization

The design of the AND logic gate structure requires careful balance of the hybridization energies of seven oligonucleotide sequences. Arguably, the most important of these are the *staple*, *backbone unit* (which makes up the *amplifier*), and *reporter* strands, as these components are responsible for the signal generation via the displacement cascade. High signal contrast in a fluorescent AND gate system is generated by low fluorescence with none or only one input added (*i.e.* a low background) and a large fluorescent response to both inputs. To achieve a low background signal, the *staple-amplifier* hybridization needs to be strong enough to prevent spontaneous dissociation and displacement by the *reporter* strand. To effectively produce a response to the inputs, however, this hybridization needed to be destabilized enough relative to the *reporter-amplifier* hybridization to

allow the displacement cascade to occur. The difference in stability between the *staple-amplifier* and *reporter-amplifier* hybridization provides the thermodynamic drive for the displacement reaction cascade. A logic gate design optimized for high signal contrast, therefore, would maximize this difference in stability while maintaining stability under the starting conditions. Several iterations (Table 3.1) of the logic gate design were designed, synthesized, and tested in attempts to realize this high signal contrast fluorescent logic gate.

Table 3.1 Oligonucleotide sequences for the successive logic gate versions. Bases in red represent mismatches within the sequences when hybridized to their intended complementary strand. Blue 'L's represent internal Uni-link™ moieties in the *backbone unit* sequences.

Name	Sequence (5'-3')
V.1 AND gate	ATCCTACTTACAACTATGTAAGTCCAGAGCCTAGTCGAAATTAAG
V.1 blocker	AGGCTCTGGACT
V.1 backbone	GAGCCTAGTCGAAATTAAG
V.1 18-mer staple	GGCTCCTTAATTTCGACT
V.1 19-mer single mismatch staple	GGCTCCTTAATTACGACTA
V.1 19-mer double mismatch staple	AGGCTCCTTAATAACGACT
V.1 input 1	AGTTGTAAGTAGGAT
V.1 input 2	CTTAATTTCGACTAGGCTCTGGACTTACA
V.2 AND gate	ACCGGTACACATAGCAGCGTCTATGTGAAGTCCAGAGCCTAGTCGAA ATTAAG
V.2 input 1	CTGCTATGTGTACCGGT
V.2 input 2	TGGACTTCACATAGACG
V.2 blocker	AGGCTCTGGACTTACA
V.2 backbone	GAGCCTAGLCGAAATTAAG
V.3 AND gate	GCAGGTCCCAGCAGAAGTCTGCTGGTGTGAAGTGGAGAGGCGCTAGA GAAGGATGGTAGGACG
V.3 input 1	ACTTCTGCTGGGACCTGC
V.3 input 2	TCCACTTCACACCAGCAG
V.3 blocker	GCCTCTCCACTTCACA
V.3 backbone	GAGGCGCTAGAGLAGGATGGTAGGACG
V.3 staple	GCCTCCGTCCTACAATCCTAATCTAGC

The first version (V.1) of the logic gate had a 19-mer *backbone unit* with three different *staple* strands tested: a fully complementary 18-mer and two different 19-mers with one and two internal mismatches, respectively. Unlabelled *backbone units* were used for this initial version to allow for efficient testing of multiple designs. The degree of hybridization of the fluorescein (FAM)-labelled

reporter strand was determined by using the DNA intercalating dye ethidium bromide (EB) to quench the fluorescence of FAM conjugated to the *reporter* strand. EB is a commonly used intercalating dye which specifically labels dsDNA, and has previously been shown to act as a FRET acceptor for FAM [161]. As the *reporter* strand is single stranded, the amount of EB binding—and therefore FRET between FAM and EB—is minimal before its hybridization to the *amplifier* structure. The FRET sensitization of the EB signal proved to be an unreliable measure of hybridization due to large variation in EB signals from sample to sample. Instead, FRET quenching of FAM was used as the measurable signal change.

The V.1 design proved the effectiveness of the ligation procedure (*vida supra*) and was tested for its displacement behaviour in the presence of the *reporter* strand. Samples of the ligation product with and without the *blocker* strand were mixed with *reporter* strand and incubated at room temperature. After the given interval (typically 1 h), EB was added, and the fluorescent signal of FAM was measured. Initial tests of the ligated products showed no significant differences in displacement behaviour between samples with or without the *blocker* strands. This indicated that significant hybridization of the *reporter* strand was occurring regardless of the whether the initiating toehold was exposed. Optimization of the *logic gate* synthesis, including increased ligation time and spin filtration of the product, greatly reduced this unwanted hybridization (Figure 3.7). *Logic gates* made using the three different *staple* strands produced significantly different results. The 19-mer *staple* with a single mismatch, as well as the original 18-mer *staple*, produced stable systems under starting conditions. The 19-mer *staple* with two mismatches proved to be too destabilized and underwent a large degree of displacement even with the *blocker* strands.

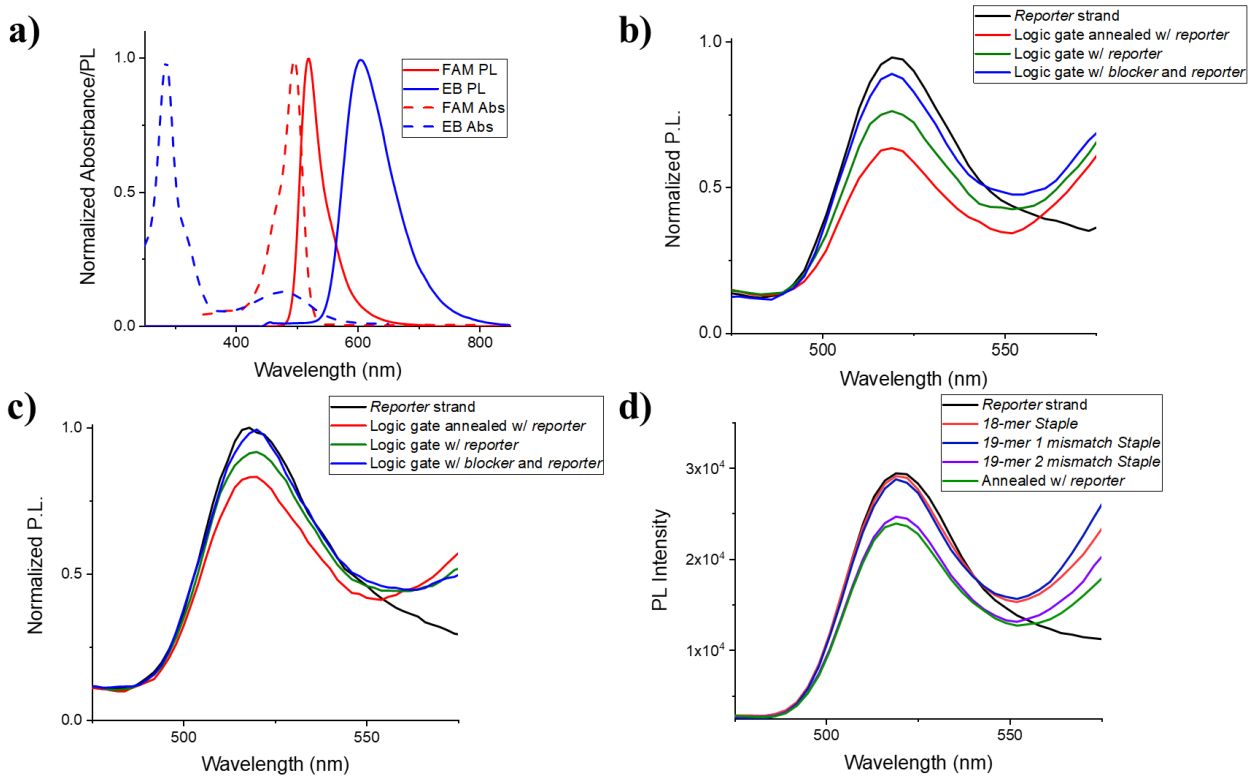

Figure 3.7 FRET quenching of FAM by EB (excitation at 300 nm, EB emission max at 605 nm omitted for clarity). **(a)** Absorbance and fluorescence spectra for FAM and EB. For **(b-d)**, the *reporter* strand signal represents the signal with no FRET quenching (*i.e.* no displacement). The annealed sample, where components were mixed and annealed by slow cooling from 95 °C before measurement, represents the maximum FRET quenching (*i.e.* full displacement). **(b)** Initial ligation products underwent a significant amount of displacement, as indicated by the decrease in FAM signal at 512 nm, even with the *blocker* present. **(c)** Optimization of the ligation procedure (extended ligation time and spin filtration) led to no detectable displacement in the sample with *blocker* present. **(d)** The redesigned 19-mer *1 mismatch staple* strand was found to produce a stable *logic gate* under starting conditions, while the *2 mismatch staple* underwent significant hybridization before the addition of inputs.

Initial tests of the V.1 AND *gate* strand design showed no significant differences in displacement between samples with none, only one, or both inputs added. To improve upon this result, the *gate*

strand was redesigned to remove the possibility of hybridization between the *input 2* strand and the *reporter*. Truth table tests for the ligated V.2 product showed a pattern of displacement consistent with AND gate behaviour (Figure 3.8a). Though this design displayed the desired response pattern, the signal contrast was significantly lower than desired. This was, in part, due to the low sensitivity of the FRET quenching by EB. To further investigate and optimize this system a *backbone unit* with reactive handle for dye-labelling (V.2) was synthesized.

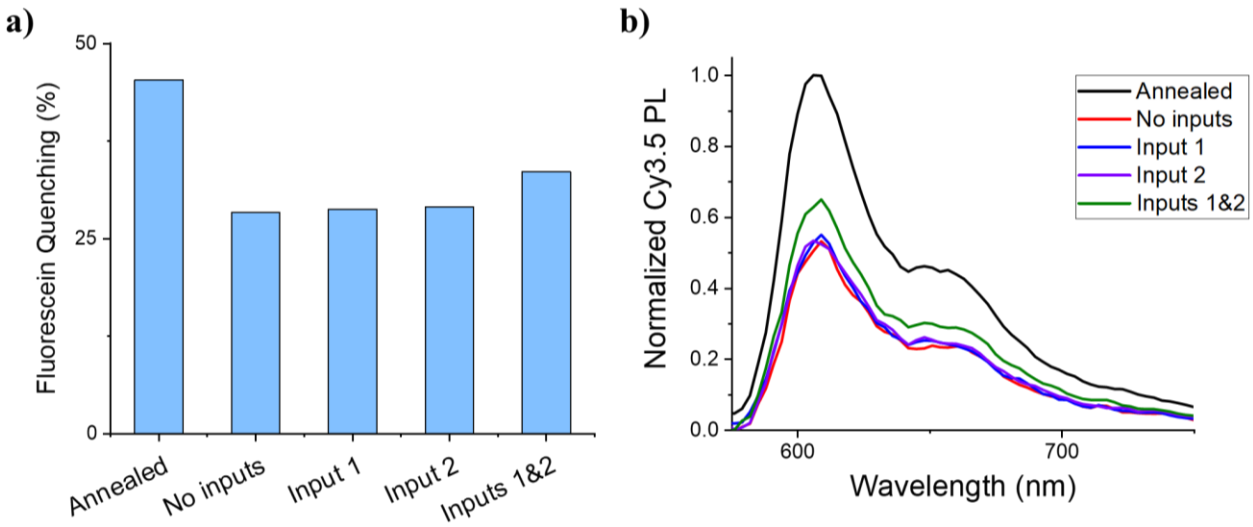

Figure 3.8 AND gate behaviour of the V.2 logic gate system. **(a)** With the original (non-dye labelled backbone) design EB FRET quenching of *reporter* FAM (exc. 300 nm), calculated by loss of signal compared to the *reporter* strand alone, showed the correct pattern of response to inputs (*i.e.* increased fluorescein quenching for the sample with both inputs), albeit with very low signal contrast (significant fluorescein quenching for samples with zero or one inputs) and incomplete displacement. **(b)** Incorporation of a dye into the *backbone unit* retained the AND gate response pattern, as measured by FRET between FAM on the *reporter* and s-Cy3.5 on the *amplifier* (exc. 470 nm, FAM signal subtracted), but produced high background due to undesired hybridization. In both cases, the annealed sample represents full hybridization of the *reporter* strand to the *amplifier*.

The V.2 *backbone* included an internal amine linker (Uni-link^{TM}) inserted into the sequence to enable conjugation with a fluorescent dye. The Uni-link group occupies the space of a single base within the phosphodiester backbone of the oligonucleotide but does not include a nucleobase to participate in hybridization. It was hypothesized that this internal linker would have a smaller destabilizing effect than a base-pair mismatch due to the lack of repulsion caused by the non-bonding nucleobase, and that the overall hybridization of the system would not be significantly affected. Dye labelling of the *backbone unit* was accomplished through coupling of NHS-ester containing sulfo-Cyanine 3.5 (s-Cy3.5) to the Uni-link amine. Ligation reactions with *backbone units* pre-labelled with fluorescent dyes proved to be unsuccessful, with no detectable formation of the ligated product. This result was likely due to inhibition of the ligase by the conjugated dye or degradation of the 3' phosphate during the conjugation reaction. Dye-labelling post-ligation was more effective, and ligation reactions were successfully conducted with all three *staple* strands. The mismatch-containing *staple* strands, however, were shown to undergo displacement regardless of the presence of the *blocker* strand. The fully complementary *staple* strand showed better stability at starting conditions and displayed AND gate behaviour in response to inputs (Figure 3.8b). The signal contrast, however, remained quite low due to incomplete hybridization (*i.e.* the signal for the sample with both inputs not matching the intensity of the annealed sample) as well as the high background signal from a combination of direct excitation of s-Cy3.5 and undesired displacement (*i.e.* the high signal for the samples with zero or one inputs). This displacement results from too weak hybridization between the *staple* and *amplifier*, suggesting that the presence of the linker/dye within the sequence had a much more significant destabilizing effect on the hybridization than anticipated. Stronger hybridization between the *staple* and *amplifier* was necessary to improve the performance of the logic gate.

A final sequence design was implemented with longer nucleotide components to allow for the inclusion of mismatches within the *staple* strands without compromising the overall hybridization. The V.3 design used 27 nucleotide *backbone unit*, *staple*, and *reporter* strands in place of the 19-mers from the earlier designs, allowing for stronger hybridization while still incorporating mismatches to provide the thermodynamic drive for displacement. Logic gates with varying ratios of the Uni-link-containing *backbone unit* and *gate* strand (1-, 2-, 5-, and 10-to-1) were synthesized to provide an initial test of this redesigned system. For these tests, a stoichiometric mixture of the *staple* and *gate* strands was annealed before addition of the *backbone unit* strand for ligation. This annealing step and the exclusion of excess *staple* strand was devised to promote complete capping of the *gate* strands. For the samples with ratios greater than 1:1, subsequent addition of *backbone unit* and *staple* strands were done in a single step. PAGE analysis of the ligation products revealed significant amounts of product with very low mobility (*i.e.* remained in the well) for the 2:1, 5:1, and 10:1 samples (Figure 3.9). This could indicate that instead of being terminated by the *gate* strand, the *backbone units* are being ligated into very long DNA structures which do not have the desired logic gate function.

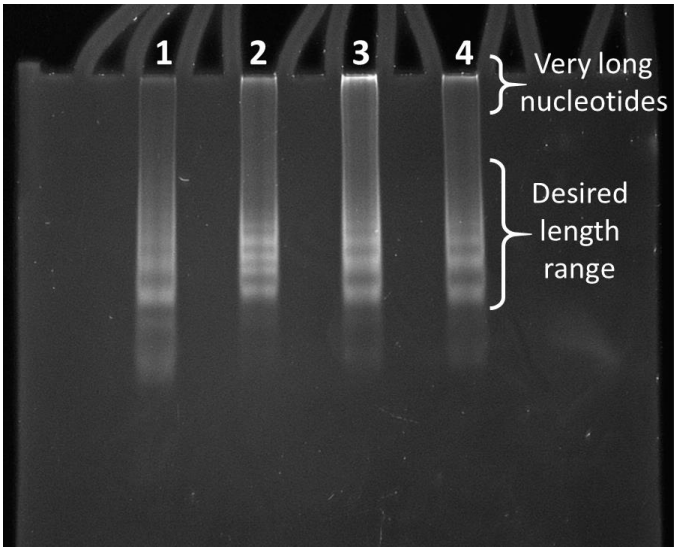

1. 1:1 ligation product
2. 2:1 ligation product
3. 5:1 ligation product
4. 10:1 ligation product

Figure 3.9 EB stained PAGE analysis of the V.3 *logic gates*. The ligated products show some product in the predicted length range, but also show significant amounts of material stuck in the well, indicating the presence of very long ligated products.

The synthesized *logic gate* systems were labelled with s-Cy3.5, and the *reporter* strand was labelled with sulfo-Cyanine 5.5 (s-Cy5.5) to act as a FRET acceptor. Measurement of the FRET sensitized s-Cy5.5 signal for the 1:1 sample showed AND gate behaviour in response to the inputs (Figure 3.10a). Addition of both inputs led to displacement similar to a sample with no *blocker* strand added (Figure 3.10b), indicating the proper functioning of the *gate* unit. Neither sample achieved a signal comparable to an annealed sample of the logic gate and *reporter* strand, however, indicating that the displacement was not complete within the given reaction time. Longer incubation resulted in a ~50% loss of signal contrast due to undesired hybridization in the samples with zero or one inputs. Further optimization of reaction conditions is necessary to allow for longer incubation times while retaining signal contrast. Analogous measurements for the 2:1, 5:1, and 10:1 *logic gates* produced similar response patterns, but with lower signal contrast in all cases compared to the 1:1 sample. This indicates that, though the displacement mechanism of the *gate* strand appears to be functioning, the synthesis of the V.3 *logic gate* is not producing the desired structures.

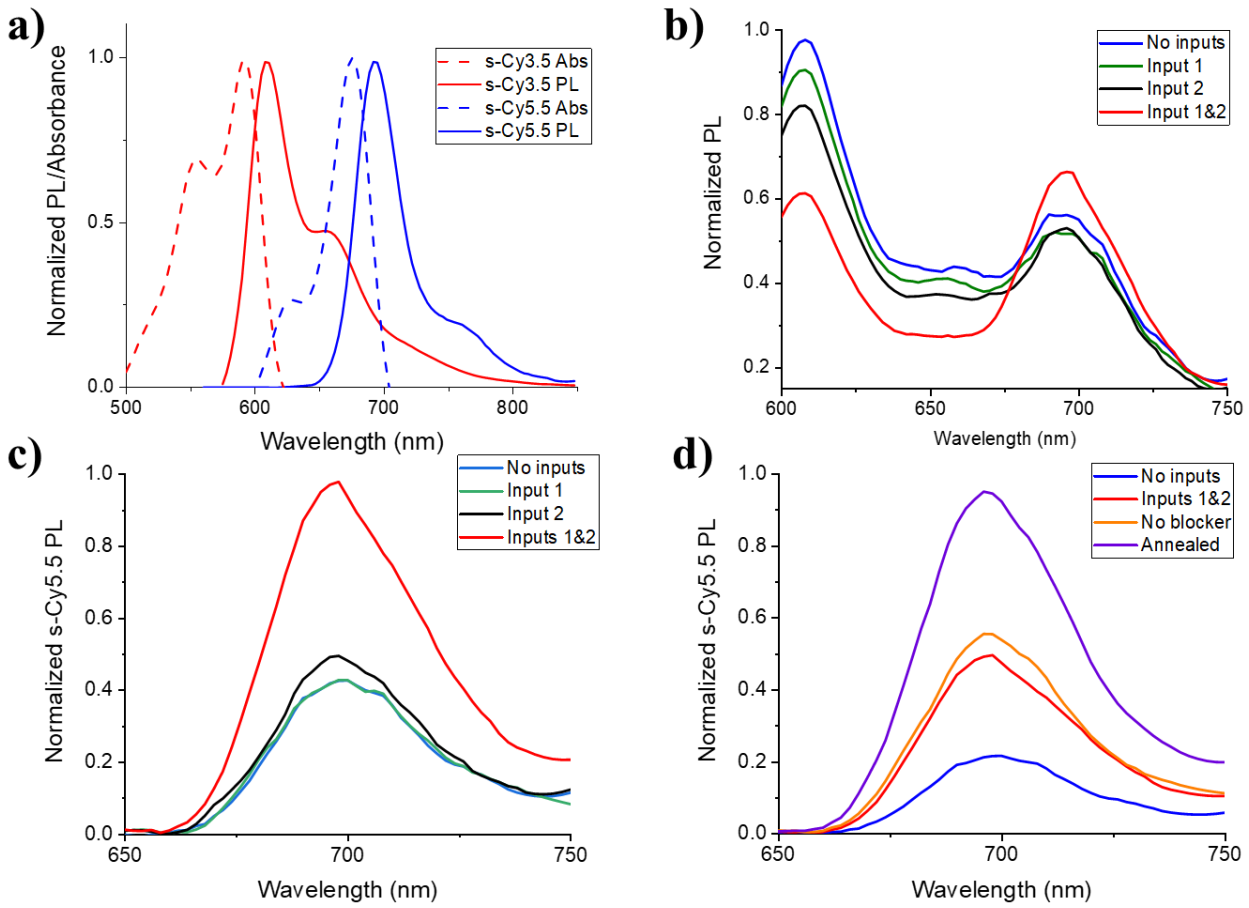

Figure 3.10 AND gate behaviour of the V.3 ligation product by FRET between s-Cy3.5 on the *backbone* and s-Cy5.5 on the *reporter* (ex. 550 nm). **(a)** Spectral overlap between s-Cy3.5 and s-Cy5.5 allows for efficient FRET. **(b)** The V.3 *logic gate* synthesized with a 1:1 ratio of *backbone* to *gate* strands showed the correct AND gate response pattern, but with limited signal contrast in the raw spectra. **(c)** Subtraction of the s-Cy3.5 signal and signal generated by direct excitation s-Cy5.5 resulted in much better signal contrast. **(d)** A sample with both inputs nearly matched the displacement of a sample with no blocker, as expected, but neither sample matched the displacement of the *logic gate* annealed with the *reporter* strand. **(d)** The sample with no inputs (*i.e.* the background signal) remained relatively high, reducing the overall signal contrast.

3.5 Conclusions

The DNA-based logic gate described in this chapter utilized an oligonucleotide displacement cascade to produce an amplified fluorescent signal. The intended result of this signal amplification was to produce a logic gate with high signal contrast between the TRUE and FALSE states. The logic gate was designed and synthesized to produce the intended AND gate response to inputs. The signal contrast achieved, however, did not meet the intended aims of the project. The relatively low signal contrast is likely caused by undesired hybridization of the *reporter* strand to the *backbone*, resulting in signal generation without actuation of the *gate* unit. This could be due to a combination of 'impurities' from the ligation procedure (*i.e.* structures without a *gate* strand at the terminus), and too weak hybridization of the *staple* and *backbone* strands. Sequence specific purification of ligation products would likely help to increase the signal contrast. Optimization of the *staple:backbone* hybridization energy would also help to increase signal contrast. Increasing the hybridization strength, however, would also result in a slower displacement reaction, potentially reducing the efficacy of the logic gate. The results presented here indicate that thorough optimization of the synthesis and displacement reactions of system could result in an amplified logic gate with very high signal contrast. Additionally, replacement of the organic dye conjugated to the *backbone units* with a luminescent lanthanide complex (LLC) to act as the FRET donor would lead to much better signal contrast by enabling time-gated fluorescence measurements.

3.6 Experimental Methods

Materials: Oligonucleotides were custom synthesized by Integrated DNA Technologies (Coralville, IA). Sulfo-cyanine 3.5 (s-Cy3.5) NHS-ester and sulfo-cyanine 5.5 (s-Cy5.5) maleimide were from Lumiprobe (Hallandale Beach, FL). T4 DNA ligase and T4 DNA ligase reaction buffer were from New England Biolabs (Ipswich, MA).

Instruments: PL and absorption spectral measurements were made with an Infinite M1000 Pro plate reader (Tecan Ltd., Morrisville, NC). Gel images were collected with a Gel Doc XR+ Gel Documentation System (Bio-Rad Laboratories Ltd., Hercules, CA). ImageJ software (NIH, Bethesda, MD) was used for processing images.

Ligation: The g*ate* (1.0-10.0 nmol), *staple* (22.0 nmol) and *backbone* (10.0-20.0 nmol) were mixed diluted to a final volume of 50 µL of 1X T4 DNA Ligase Reaction Buffer. To this mixture T4 DNA Ligase was added (3.0 µL, 1200 units). The ligation mixture was cooled to 4 °C and incubated for 1-5 days. The mixture was then heated to 75 °C for 5 min before cooling to room temperature. The product was purified by filtration with 10 kDa cutoff centrifugal filters (10 min, 16 900 RCF). The product diluted and spin filtered three times with 500 µL of *DNA hybridization buffer* (20 mM Tris, 10 mM NaCl, 0.5 mM $MgCl_2$, pH 7.4). The product was analyzed by PAGE, and its concentration was determined by absorbance at 260 nm.

NHS-ester dye labelling: Oligonucleotide samples dissolved in nuclease-free water were dried by vacuum centrifugation in 1.5 mL microcentrifuge tube. Dried samples were resuspended to 100 µM in 100 mM sodium bicarbonate buffer (pH 8.2) and cooled on ice. Ten molar equivalents of the dye NHS-ester (dissolved in DMSO) were diluted with DMSO to a final volume of one-

quarter the total intended reaction volume and added to the oligonucleotide solution. The reaction was covered from light and briefly vortexed and centrifuged before being placed back on ice for 5 min. The covered reaction mixture was then placed on a rotating mixer and mixed overnight at room temperature. After the reaction, the oligonucleotide was isolated by ethanol precipitation. The reaction mixture was diluted ~2.5-fold with water and 3 M sodium acetate to a final concentration of 0.5 M sodium acetate. Three volumes of ethanol were added to this mixture for a final composition of 75% ethanol, and the solution was incubated at –20 °C for at least 4 h. The mixture was then centrifuged at 17 000 RCF for 30 min and the supernatant was discarded. Finally, the pellet was rinsed with cold 70% ethanol and then left to air dry for 20 min to remove residual solvent.

Maleimide-thiol dye labelling: Oligonucleotide samples dissolved in nuclease-free water were diluted to 200 µL in 10X Dulbecco's phosphate buffered saline (DPBS) with 10 mM tris(2-carboxyethyl)phosphine (TCEP). After 30 min incubation at room temperature, this mixture was loaded onto a Nap-10 column and eluted with 10X DPBS. Ten molar equivalents of the maleimide containing dye (in DMSO) were added to the solution and the reaction was covered from light and placed on a rotating mixer overnight at room temperature. The volume was reduced to ~500 µL under vacuum then loaded onto a NAP-10 column and eluted with 0.2 M triethylammonium acetate. The product was then fully dried under vacuum. If necessary, unconjugated dye was removed by ethanol precipitation of the oligonucleotides (see above).

Displacement tests: Ligation products (1.0-10.0 pmol) were mixed with the *blocker* (2 equiv) strand and annealed by heating to 95 °C for 5 min before slowly cooling to room temperature. To this mixture, one or more of *input 1* (1 equiv), *input 2* (1 equiv), and *reporter* (1 equiv to the

concentration of *backbone* units) were added, and the solution was diluted to 100 µL with *DNA hybridization buffer*. The mixture was incubated for a set period at constant temperature (typically 1 h and room temperature) before transferring the solutions to a 96-well plate and measuring the fluorescent signal on the plate reader. For experiments using ethidium bromide (EB), 10 µL of EB (1 µM) was added to the solution and the solution was incubated for 2-3 min before measurement.

Polyacrylamide gel electrophoresis (PAGE): A 7.5 mL-solution of the desired concentration of acrylamide/bis-acrylamide (37.5:1) solution was made by diluting an appropriate volume of 40% w/w stock into 1X TBE. The solution was degassed under vacuum for 30 min. To the degassed solution, 7.5 µL of tetramethylethylenediamine (TEMED) and 30 µL of 25% w/v ammonium persulfate (APS, aq) were added. The solution was gently mixed before being transferred to a vertical gel caster and left to set at room temperature for 1–2 h. Samples were diluted to 10 µL with a final concentration of 25% v/v glycerol before loading onto the gel. Gels were run with 1X TBE as the running buffer.

Chapter 4: Quantum Dot-Catalytic Hairpin Assembly Logic Gate

4.1 Logic Gate Design

This project focuses on the design and synthesis of a logic gate in which oligonucleotides colocalized on the surface of a quantum dot (QD) interact to produce amplification of a fluorescent signal. As in Chapter 3:, this project aimed to develop a method for amplification of a DNA-based logic gate through cascading hybridization events. The proposed amplified logic gate is based on the use of a catalytic hairpin assembly (CHA) to produce a FRET-sensitized fluorescent signal. In a CHA, a *catalyst* oligonucleotide opens a hairpin through toehold-mediated displacement to reveal a toehold previously hidden within the stem of the hairpin (Figure 4.1). An invading strand then binds to this exposed toehold and displaces the catalytic oligonucleotide, leaving a newly formed duplex. The *catalyst* strand is free at this point to bind a second hairpin and repeat the cycle. This project aimed to adapt this design to produce an amplified FRET-sensitized fluorescent response to logic inputs. Here, the catalytic strand comprises the end of a hairpin (HP)-forming sequence that is opened upon hybridization with logic inputs. This *catalyst* HP strand is colocalized along with the *acceptor* HP strand on a QD. The QD serves dual purposes: a FRET donor to sensitize a fluorescent dye on the *reporter* strand and a means of increasing the effective concentrations of the catalytic sequence and the target hairpin.

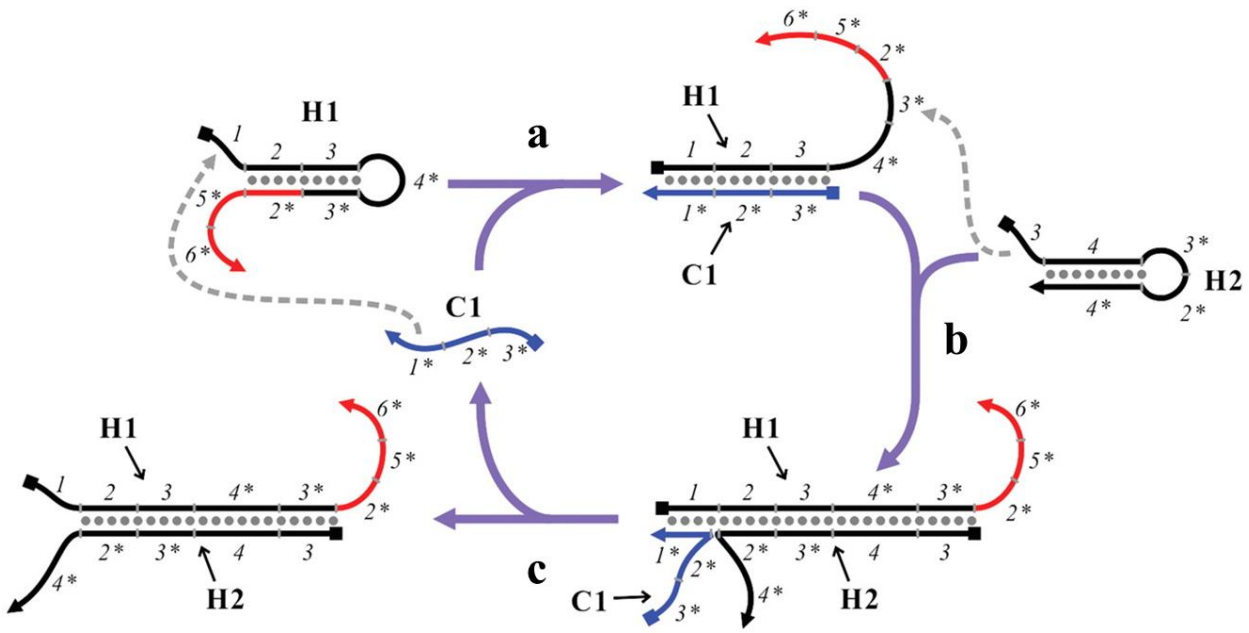

Figure 4.1 Catalytic hairpin assembly (CHA). **(a)** The catalyst strand (C1) opens the first hairpin (H1) via toehold mediated strand displacement. **(b)** This reveals a hidden toehold that the second hairpin (H2) binds to. **(c)** Hybridization of H1 and H2 displaces C1, resulting in a new duplex (H1:H2) and releasing the catalyst to bind to a second H1. Adapted from Ref. [162], with permission from Oxford University Press.

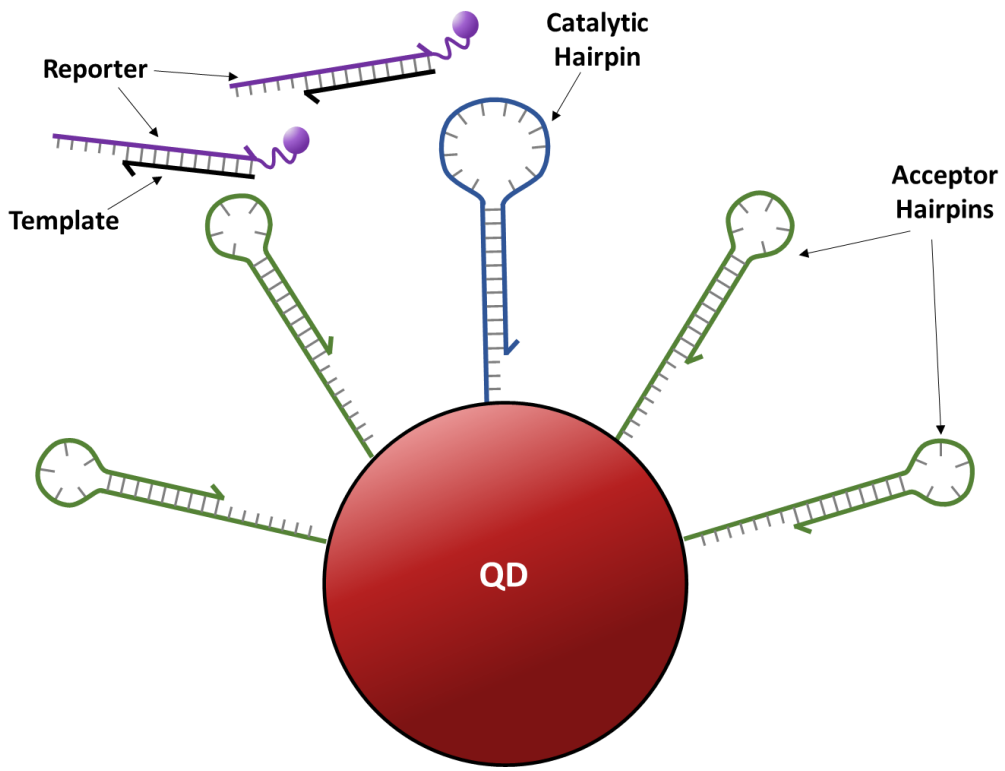

Figure 4.2 Simplified representation of the initial state of the QD-CHA logic gate (before the addition of inputs).

In its initial state, the system comprises a QD covered with a mixture of two oligonucleotides in hairpin form—the *catalyst* and *acceptor*—with a freely-diffusing dye-labelled *reporter* strand in the surrounding solution (Figure 4.2). The *acceptor* contains a hidden toehold for hybridization with the *reporter* within the stem of its hairpin structure, preventing spontaneous hybridization. To initiate the catalytic cycle, inputs are added to open the *catalyst* hairpin, effectively releasing the catalytic segment at its distal end (Figure 4.3a). The *catalyst* is long enough such that, when opened, the catalytic segment can access all the other nucleotides conjugated to the surface of the QD. In the next step, the catalytic segment binds to an exposed toehold on an *acceptor* and displaces the stem duplex, opening the hairpin (Figure 4.3b). This hybridization, in turn, exposes

the hidden toehold for the *reporter*, allowing it to hybridize to the *acceptor* (Figure 4.3c). This hybridization puts the dye on the *reporter* in proximity to the QD, allowing for FRET from the QD to the dye (Figure 4.3d). The displacement of the *catalyst* strand also returns the system to the beginning of the catalytic cycle, leading to further hairpin opening and *reporter* hybridization. The long strand containing the catalyst segment at its distal end can be thought of as a DNA walker moving along the 3D-track represented by the surface of the nanoparticle, a concept that has previously been developed using DNA-coated gold nanoparticles [35].

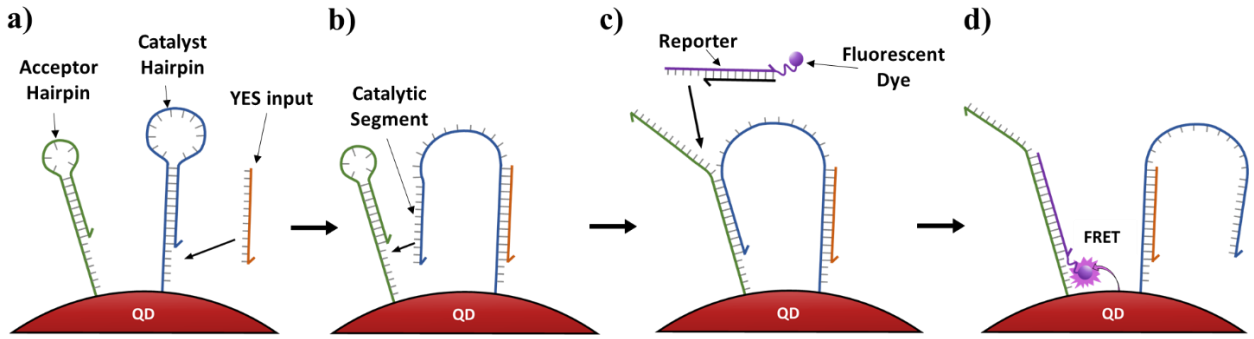

Figure 4.3 FRET signal generation in the DNA HP walker logic gate. **(a)** Displacement of the hairpin by the input/s leads to release of the catalytic segment at the distal end of the *catalyst* oligonucleotide. **(b)** This catalytic segment can then displace the hairpin of the *acceptor* oligonucleotide, revealing a hidden toehold for **(c)** the *reporter* strand to hybridize. **(d)** The catalytic segment is released with hybridization of the *reporter*, and FRET from the QD to the dye gives the fluorescent output signal. Note: the *anchor* strand is omitted in this depiction and the oligonucleotides are not drawn to their full length for the sake of clarity.

The success of this design relies on the balance of hybridization strength between the various duplexes formed during the catalytic cycle. To produce a functional cycle, each displacement step must produce a more stable duplex than the previous step. The component sequences (Table 4.1) were rationally designed to exist as stable hairpins under initial conditions and to initiate strand displacement upon the opening of the hairpin of the *catalyst*. A *template* strand was designed as a partial complement to the *reporter* strand, blocking most of the sequence to prevent unwanted hybridization. This *reporter-template* duplex leaves a section of the *reporter* as a single-stranded dangling end that can bind to the exposed toehold region of the *acceptor*. This binding initiates the toehold-mediated strand displacement of the *catalyst*, as the *reporter-acceptor* duplex is the most stable amongst all the duplexes formed in the system.

Table 4.1 Oligonucleotide sequences for the QD-CHA logic gate. Underlined segments denote the *anchor* binding regions and bolded segments denote the hairpin forming regions.

Name	Sequence (5'-3')
Anchor	GAGCCAACCGAACGAGT
Conjugation 1	ACTTGTTC
Conjugation 2	GGTAGGCT
Catalyst Hairpin	<u>ACTCGTTCGGTTGGCTC</u>GGTGACTG**CAGTGACTCAG**CCTTCCTCTCTTCCTT CCCCTTCCTTCCTTCCTTTA**CTGAGTCACTG**
Acceptor Hairpin	<u>ACTCGTTCGGTTGGCTC</u>CAGT**GACTCAG**ACGGCA**CTGAGTC**
V.1 Reporter	GACTCAGTGCCGTCTGAGTCGTTT
V.1 Template	CGACTCAGACGGCAC
V.2 Reporter	AGTGCCGTCTGAGTC
V.2 Template	AGACGGCACT
YES Input	CTGAGTCACTGCAGTCACC

The colocalization of the hairpin sequences on the nanoparticle functions to favour inter-molecular over intra-molecular hybridization. Typical DNA duplex formation is dependent on diffusion through 3D space and random collisions between nucleotides to initiate hybridization. Co-localization of hairpin strands on a DNA 'track' has been shown to greatly increase the kinetics of the hybridization between the components [34]. This phenomenon has been used recently to increase both the speed and efficiency of multistep DNA hybridization reactions [163,164]. The increase in the speed and degree of hybridization between components can be accounted for by the increase in the effective concentrations of the components due to their confinement within a finite volume [165]. It should be noted that these examples use nucleotides or DNA origami structures to co-localize the hairpins and that the conjugation of DNA to nanoparticle surfaces have less consistent and predictable effects [166,167]. In this project, it was hypothesized that co-localization of the hairpin strands on a QD surface would affect the kinetics of their interactions to produce a more rapid and efficient catalytic hairpin assembly, and therefore better amplification of the logical output signal.

4.2 QD-DNA Conjugation

To implement this logic gate design, it was important to produce QDs with many DNA strands attached to their surfaces. The ratio between the two hairpin oligonucleotides in the logic gate design is important for the proper functioning of the system. In theory, a single *catalyst* hairpin could interact with all the *acceptor* hairpins co-localized on a single QD. This extent, however, would require specific conjugation of a single *catalyst* strand to each QD, which is experimentally not feasible. Instead, the hairpins were simultaneously conjugated to the QD together in a fixed

ratio such that, on average, the QDs have the same ratio of oligonucleotides. It is therefore beneficial to maximize the number of DNA strands conjugated to each QD to reduce the probability of a QD without a conjugated *catalyst* hairpin strand. Additionally, higher DNA density on the QD surface also functions to increase the fluorescent output signal, as single QD can act as FRET donors to many dye molecules. To minimize the possibility of preferential conjugation of either of the hairpin strands based on size or sequence, QDs were conjugated with a common *anchor* strand. This strand comprised a twenty base-pair sequence which was the complement of a segment at the ends of each hairpin sequence.

Single-stranded oligonucleotides are known to adsorb to QD surfaces via hydrogen bonding through the bases [73]. Lasting conjugation, however, requires incorporation of a terminal functional group that forms a bond (or multiple bonds) with the nanoparticle surface. Thiol-containing linkers are particularly useful for conjugation to QD surfaces and have long been used to create DNA-coated QDs [70]. Dihydrolipoic acid (DHLA, Figure 4.4) is a commonly used ligand that contains a terminal dithiol group that has strong interactions with QD surfaces. A DHLA-based linker (DHLA-C6, Figure 4.4) was synthesized based on previously published results from the Algar group [168]. The additional length (in comparison to DHLA) provided by the six-carbon chain provides more distance between the QD surface and the oligonucleotides, hypothetically reducing the effects of steric hindrance and electrostatic repulsion and allowing for the conjugation of more DNA strands to each QD. The *anchor* strand was commercially synthesized with an amine functional group at the 5’ end to enable conjugation with the NHS-ester functionalized linkers. The linker-modified oligonucleotide was purified by size-exclusion chromatography and used for conjugation with QDs.

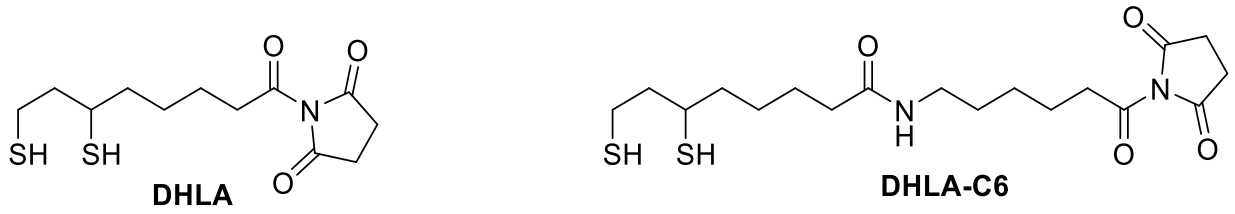

Figure 4.4 Dithiol linkers used for the conjugation of DNA to QD surfaces.

To facilitate surface conjugation with DNA, the QDs were first coated with a water-soluble ligand to allow for resuspension in aqueous buffer. A suitable ligand for this purpose needs to bind to the QD surface such that it produces colloidally stable aqueous QDs for subsequent ligand exchange, but with weaker binding than DHLA to allow for displacement with the DHLA-C6 functionalized DNA. Ligand exchange with histidine coated QDs (His-QDs) has been used to produce high levels of DNA surface coverage on QDs [74,169]. Here, glutathione (GSH) was used due to the better colloidal stability of GSH-QDs compared to His-QDs. The concentration of salt is also a crucial element in the conjugation of DNA and nanoparticles. Electrostatic repulsion between the negatively charged QD surface and nucleotide backbones is reduced by the presence of cations that act to shield the negative charges. Direct addition of a high concentration of salt, however, reduces the colloidal stability of the QDs and results in aggregation. Instead, gradual addition of salt—a technique known as ‘salt-aging’—is used to increase the salt concentration as the colloidal stability increases due to the surface conjugated DNA. This process was originally developed for DNA coating of gold nanoparticles [170,171] and has since been successfully adapted for QD coating [74]. Finally, conjugation of dsDNA to QD surfaces produces increased surface coverage by eliminating the issue of non-specific absorption of ssDNA to the nanoparticle surface. The use of short complementary oligonucleotides to assist during conjugation has been shown to allow for

high density QD coverage with ssDNA [74]. These oligonucleotides are easily removed by filtration after conjugation as they are too short to form stable duplexes at room temperature.

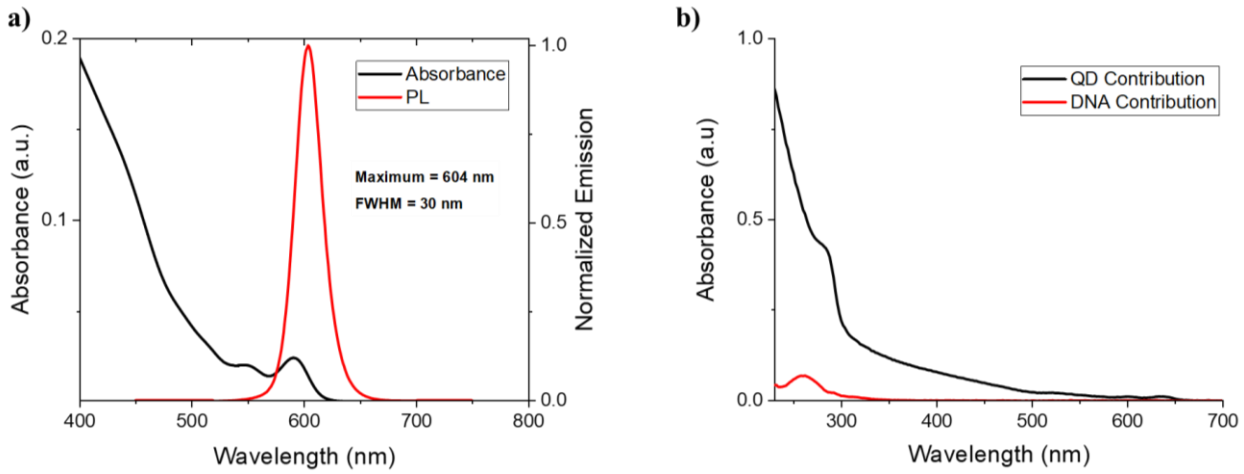

Figure 4.5 Spectroscopic analysis of QDs and QD-DNA conjugates. **(a)** UV-vis absorbance and fluorescence measurements for synthesized QDs and **(b)** deconvoluted absorbance measurements for determining the DNA:QD surface coverage (36.6:1).

CdSe/ZnS core-shell QDs with an emission maximum of 604 nm (QD604) were synthesized by traditional hot-injection methods (Figure 4.5a). The organic surface ligands of the QDs were replaced with either His or GSH to allow for resuspension in aqueous buffers. A variety of ligand exchange conditions were tested including the DNA conjugated ligand, equivalents of DNA, use of ssDNA or dsDNA, salt concentrations, and temperature. Illustrative results from these experiments are summarized in Table 4.2. DHLA-C6 was found to improve DNA density compared to DHLA, as was the use of oligonucleotides in dsDNA form for conjugation. Initial tests used in-house synthesized QD604, but it was found that replacing these with larger

CdSe/CdS/ZnS core-shell-shell QDs (QD644, provided by a collaborator) further improved the DNA:QD ratio. Finally, conducting the reaction at 4 °C allowed the hybridization of two short oligonucleotides to the *anchor*, producing dsDNA for the DNA coating process but ensuring easy removal of the non-conjugated DNA during the purification steps. Cooling the reaction from room temperature to 4 °C after initial DNA conjugation at room temperature led to aggregation of His-coated QDs but was found to be effective with GSH-coated QDs (Figure 4.6). After the ligand exchanged reaction, the QD-DNA conjugates were spin filtered to remove any unconjugated DNA. The DNA:QD ratio was determined by deconvolution of the QD and DNA contributions to the UV-visible absorbance spectra of the purified products (Figure 4.5b). The optimized procedure (see Experimental Methods) produced QDs with approximately 36.6 DNA per nanoparticle. Given this high surface density the *acceptor* hairpin could be added in a relatively large excess to the *catalyst* hairpin (*e.g.* 10:1) with only a negligible amount of the QD population not containing a catalytic unit.

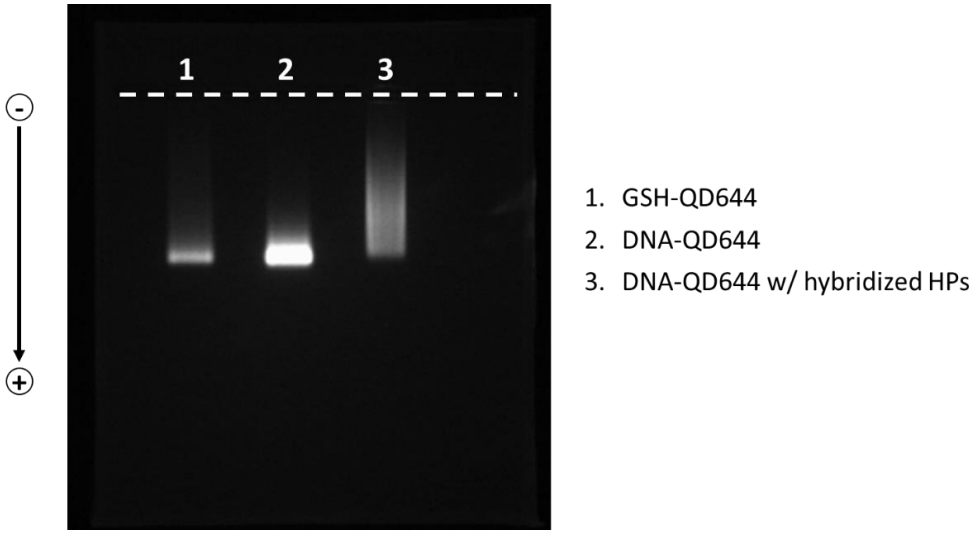

Figure 4.6 Analysis of DNA-QD conjugates by agarose gel electrophoresis. Additional negative charge from the DNA is balanced by the increased sized, resulting in approximately equal mobility between **1** and **2**. Hybridization of the HP strands resulted in streaking in **3** due to the secondary structures of the DNA.

Table 4.2 Summary of DNA-QD conjugation experiments. All experiments listed here used a starting NaCl concentration of 50 mM which was increased to 400 mM after 8 h. QD604 were synthesized in-house while QD644 were provided by a collaborator.

QD	Reaction Conditions				DNA:QD ratio
	DNA Linker	DNA equivalents	DNA type	Temp	
QD604-His	DHLA	20	ssDNA	RT	4.0
QD604-His	DHLA	40	ssDNA	RT	6.5
QD604-His	DHLA	20	dsDNA	RT	10.8
QD604-His	DHLA-C6	40	dsDNA	RT	15.4
QD644-His	DHLA-C6	40	dsDNA	RT	24.0
QD644-His	DHLA-C6	40	dsDNA	RT → 4 °C	-
QD644-GSH	DHLA-C6	60	dsDNA	RT → 4 °C	**36.6**

4.3 Logic Gate Development

The components of the logic gate were rationally designed to produce a system with the required hybridization properties. Melting temperature (T_m) values for the various duplexes and hairpin structures were calculated using DINAMelt [143]. The hairpins were designed such that they would not spontaneously undergo inter-strand hybridization at room temperature when folded but could readily hybridize when the *catalyst* strand was unfolded. A key assumption here was that, apart from an increased effective concentration, the behaviour of the oligonucleotides conjugated to the QD surface would be analogous to DNA in solution. The effective concentration of DNA around a QD was calculated based on the volume around the QD in which the oligonucleotides were free to move, which was estimated as a sphere with a radius equal to the length of the oligonucleotides plus the radius of the QD, with the volume occupied by the QD subtracted. The calculated value (~0.5 mM) represents only an approximation of the effective concentration but provided a useful starting point for the oligonucleotide design. The strength of hybridization between the hairpins was designed with this elevated effective concentration taken into consideration, as the concentration of the oligonucleotides plays a large part in determining the T_m of their duplex. The hybridization of the *input* and *reporter* strands involves oligonucleotides free in solution bonding to the QD-conjugated hairpin strands. As such, these strands were designed based on calculations using the overall DNA concentrations in the solution rather than the effective concentration at the QD surface.

An important feature of this design is the ability to produce multiple logic functionalities by simply changing the sequences of the input strands. Three sets of logical inputs were designed, representing three different logic gate functions: AND, OR, and INH (Figure 4.7). The AND gate

(Figure 4.7a) design utilized the principle of associative toehold activation [31]. In this design scheme, half of the first input hybridizes to the exposed toehold region with the other half remains as an exposed single stranded section. Half of the second input binds to this exposed section, leaving the remainder of its sequence to displace the stem segment of the hairpin. The OR and INH two logic gate designs are made possible by the large loop of the *catalyst* hairpin. At 36 bases long, the loop is large enough such that toehold binding within the loop is not significantly different than binding to random-coil DNA [172]. For the OR gate (Figure 4.7b), this allows unique input strands to bind to toeholds on either side of the hairpin stem segment. Both strands contain a segment that displaces the hairpin stem segment and therefore opens the *catalyst* hairpin. Similarly, the INH gate (Figure 4.7c) uses two unique strands which bind to toeholds within the hairpin loop and displace the stem segment. In this case, however, one of the inputs binds to the distal end of the opened sequence effectively blocking the catalytic segment within the sequence.

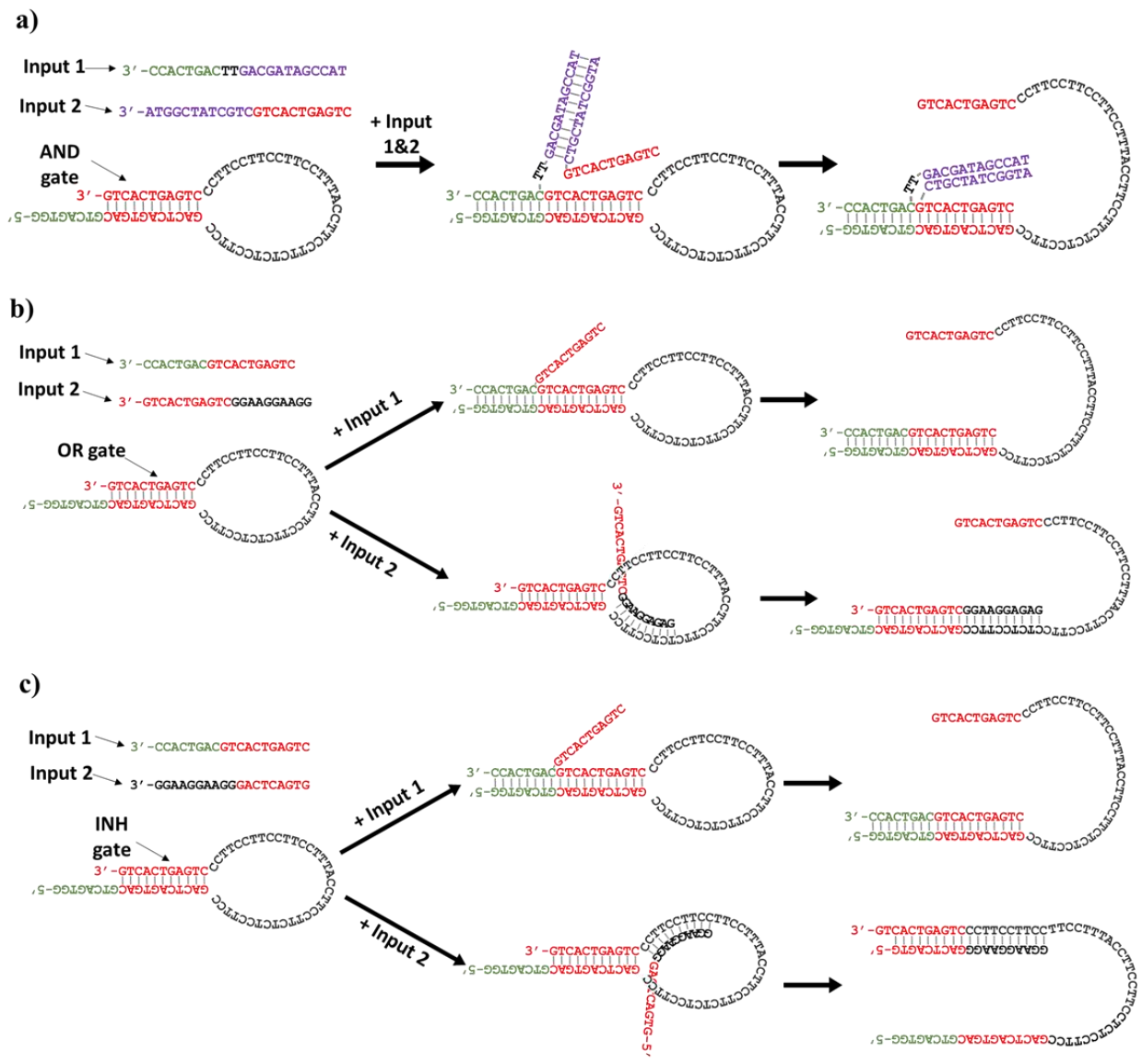

Figure 4.7 Sequences and actuation of the proposed logic gate designs. The **(a)** AND gate uses associative toehold activation, while the **(b)** OR and **(c)** INH gates employ binding of inputs in the large hairpin loops.

A simpler YES gate with a single input strand (*input 1* from the OR gate) was initially used to test the efficacy of the signal amplification system. To produce the logic gate device, mixtures with different ratios of the two hairpin strands were added to solutions of QDs coated with the *anchor*

oligonucleotides and incubated at room temperature to allow hybridization. Unhybridized DNA was subsequently removed via spin filtration. The *reporter* strand was labelled with the fluorescent dye sulfo-cyanine 5.5 (s-Cy5.5), which is a suitable FRET acceptor for the QDs. The degree of hybridization between the *reporter* strand and *acceptor* hairpin was measured by the increase in the FRET sensitized emission of s-Cy5.5. The dye-labelled *reporter* strand was hybridized with a partially complementary *template* strand to block all but the toehold binding segment of the sequence. This approach was intended to eliminate unwanted binding between the *reporter* and *acceptor* hairpin which would result in a high background signal. The system was tested by adding the *reporter:template* complex to a solution of the hairpin DNA-coated QDs and measuring the change in s-Cy5.5 signal over time (Figure 4.8a). These tests revealed an increase in the rate of hybridization of the 'reporter' strand with the YES input added when compared to the sample with no input (Figure 4.8b). The increase in rate was minor, however, and the high background caused by hybridization in the no-input sample is a significant issue for this system. It was hypothesized that hybridization in the *reporter:template* complex was not strong enough to prevent release of the *reporter* strand and subsequent hybridization to the *acceptor* hairpin. The *reporter:template* duplex was redesigned, but synthesis of this system and subsequent experiments were not carried out due to limited time and the unpromising results of the previous iteration.

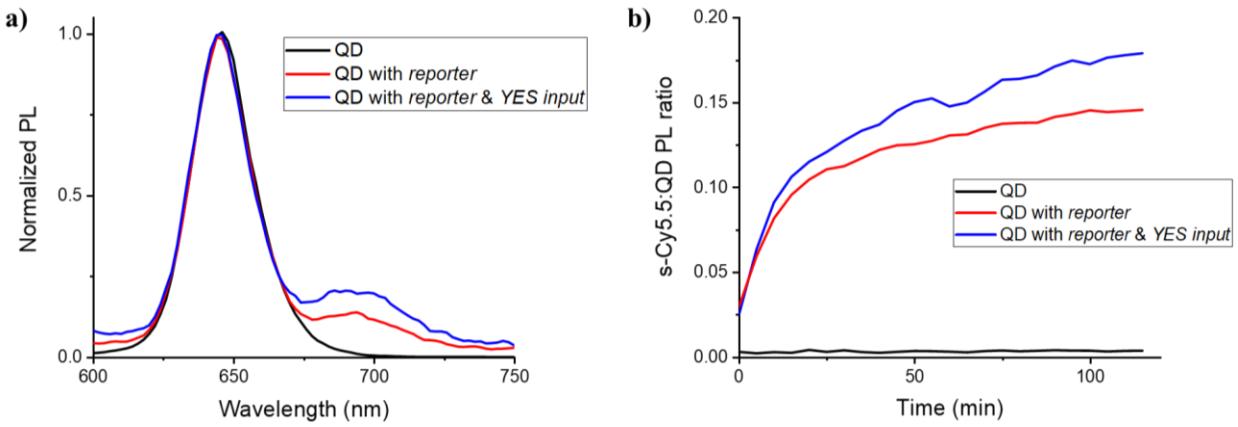

Figure 4.8 Fluorescence measurement of FRET between QD644 and s-Cy5.5 (excitation λ = 490 nm). **(a)** The FRET sensitized signal of s-Cy5.5 (emission max = 694 nm) is increased in the presence of the *YES input*. **(b)** Time course measurements of the increasing ratio of s-Cy5.5 (696 nm) to QD644 (644 nm) emissions reveal a minor increase in the rate of *reporter* hybridization with addition of the *YES input*.

4.4 Conclusions

Optimization of the QD-DNA conjugation procedure resulted in a sufficiently high number of DNA strands per QD (~36.6) for the functioning of the logic gate design. The catalytic hairpin design, however, produced only limited acceleration of the displacement with the addition of the activating *input*. This result is thought to be due to imprecision in the design of the *hairpin*, *reporter*, and *templates* sequences due to assumptions made about the hybridization behaviour of the strands at the nanoparticle surface. The system was designed on the principle that QD conjugation would increase the apparent concentration of the strands but otherwise not have a significant effect on their interactions. It is likely the case that this is not true, and that factors such as electrostatic repulsion between strands and interactions with the QD surface or surface ligands play a non-trivial role in the functioning of the system. Continuation of this project would require

more thorough investigation of the effects of QD conjugation on the hybridization of the DNA components of the system. Understanding this phenomenon is key to the accurate design of oligonucleotide sequences and would enable construction of a more efficient catalytic system.

4.5 Experimental Methods

Materials: CdSe/CdS/ZnS QD655 were provided by a collaborator. Oligonucleotides were custom synthesized by Integrated DNA Technologies (Coralville, IA). L-glutathione (reduced), histidine, N-hydroxysuccinimide, and 6-aminocaproic acid were from Sigma Aldrich (Oakville, ON). Sulfo-cyanine 5.5 NHS-ester was from Lumiprobe (Hallandale Beach, FL). Lipoic acid was from Oakwood Chemicals (Estill, SC).

Instruments: PL and absorption spectral measurements were made with an Infinite M1000 Pro plate reader (Tecan Ltd., Morrisville, NC). Gel images were collected with a Gel Doc XR+ Gel Documentation System (Bio-Rad Laboratories Ltd., Hercules, CA). ImageJ software (NIH, Bethesda, MD) was used for processing images.

Synthesis of lipoic acid-NHS ester (LA-NHS): Lipoic Acid (LA; 4.1 g, 20 mmol) and *N*-hydroxysuccinimide (NHS; 2.9 g, 25 mmol) were dissolved in 30 mL of tetrahydrofuran (THF). N,N´-Diisopropylcarbodiimide (DIC; 3.6 mL, 23 mmol) was added to 10 mL of THF, and this solution was added dropwise to the solution of LA. The reaction was stirred for overnight at room temperature and the resulting white precipitate was filtered by gravity. The filtrate was collected and concentrated to ~5 mL using a rotary evaporator before isopropanol was added and the mixture was left at –20 °C overnight to crystallize LA-NHS. The pale-yellow crystals were collected by

vacuum filtration, washed with ether, and dried. The product LA-NHS (3.807 g, 9.140 mmol, 46% yield) was stored at –20 °C until needed.

Synthesis of lipoic acid-C6 (LA-C6):

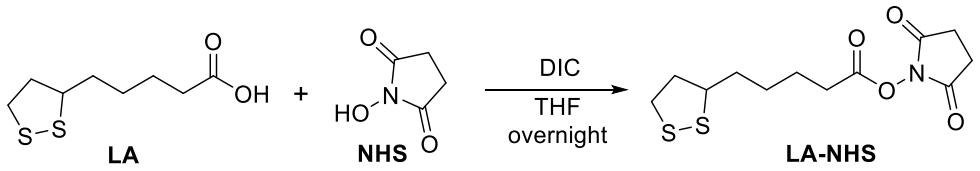

LA-NHS (0.600 g, 1.978 mmol) and 6-aminocaproic acid (0.501 g, 3.82 mmol) were dissolved in 18 mL anhydrous MeOH. Anhydrous pyridine (9 mL, dried over Na_2SO_4) was added and the solution was mixed overnight at room temperature. The solution was diluted to ~300 mL with 1.5 M HCl (aq) with 0.5 M NaCl (aq) and the product LA-C6 was extracted with 75 mL DCM. The organic phase was washed three times with a solution of 1.5 M HCl (aq) with 0.5 M NaCl (aq) and dried over Na_2SO_4. The solvent was evaporated to ~5 mL and 25 mL ether was added. This process was repeated three times to produce a solution of ~99% ether. Finally, the solvent was quickly evaporated to yield LA-C6 as a pale yellow solid (0.232 g, 0.726 mmol, 36% yield) which was immediately used for the next step.

Synthesis of LA-C6-NHS ester:

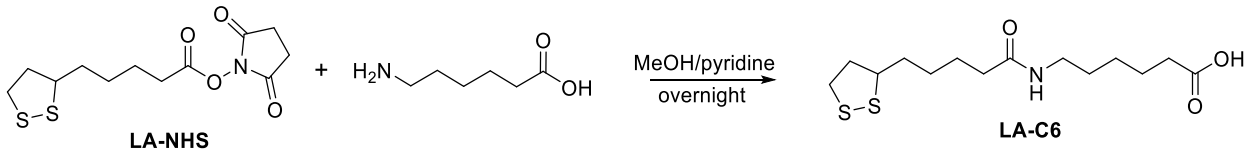

LA-C6 (0.232 g, 0.726 mmol) was dissolved in 20 mL THF and NHS (0.103 g, 0.895 mmol) was added. DIC (0.111 g, 0.881 mmol) was dissolved in 3 mL THF and added dropwise. The solution was stirred for 5 h at room temp and the solvent was reduced to ~5 mL. The yellow oil was filtered, 20 mL of isopropanol was added, and the solution was cooled to –20 °C overnight. The precipitate was separated by vacuum filtration and washed with ether. LA-C6-NHS was isolated as a pale yellow solid (0.123 g, 0.308 mmol, 42%) and stored at –20 °C until needed.

Ligand DNA coupling: 50 μL of 1 mM *anchor* oligonucleotide (50 nmol) was dried to a solid and resuspended in 25 μL borate buffer (100 mM, pH 8.5) and 25 μL DMSO was added. NHS-ester ligand (LA or LA-C6; ~10 μmol) were dissolved in 50 μL DMSO and added to the DNA solution. The reaction mixture was mixed overnight at room temperature. Borate buffer (300 μL) was added and the reaction was centrifuged to precipitate the unreacted ligand. The product was loaded onto a NAP-10 column and eluted with water to remove any residual unreacted ligand. The product was quantified by UV-Visible absorbance measurement and concentrated to dryness under vacuum.

CdSe/ZnS core-shell QD synthesis: Selenium (27 mg, 0.34 mmol) was dissolved in 4 mL of trioctylphosphine (TOP) overnight under inert atmosphere. Cadmium oxide (57 mg, 0.44 mmol) was combined with hexadecylamine (HDA, 6.0 g) and trioctylphosphine oxide (TOPO, 6.0g) and

flushed with N_2. The mixture was degassed under vacuum at 100 °C for 1 h, then heated to 320 °C over 1 h and held at 320 °C for 3 h. The TOPSe mixture was then quickly injected to the solution, and the temperature was held at 290 °C for 90 s. The mixture was cooled to 260 °C and the shelling mixture (1.8 mL TOP, 1.1 mL $ZnEt_2$, and 0.1 mL $(TMS)_2S$) was added dropwise. The mixture was allowed to cool and stirred overnight at 100 °C. The mixture was then cooled to 60 °C and 10 mL of chloroform was added before cooling to room temperature. QDs were precipitated with acetone and resuspended in chloroform three times before finally being resuspended in 10 mL of chloroform.

QD glutathione conjugation: QDs (~1.0 nmol) were precipitated from chloroform three times by addition of acetone and centrifugation for 10 min at 16,900 RCF, before a final resuspension in 500 µL of chloroform. Glutathione (GSH, 40 mg, 0.13 mmol) was dissolved in 200 µL methanolic tetramethylammonium hydroxide (TMAH; 25% w/w TMAH) and added to the QD solution. The mixture was vortexed and let stand at room temperature for ~4 h. Borate buffer (200 µL; 50 mM, pH 9.5, 250 mM NaCl) was added and the mixture was vortexed and left to allow phase separation. The aqueous phase was removed and the GSH-QDs were separated and washed twice by addition of ethanol, centrifugation for 10 min at 4 800 RCF, and resuspension in borate buffer. The GSH-QDs were finally resuspended in borate buffer (50 mM, pH 8.5).

QD DNA ligand exchange: GSH-QD644 (10 µL, 3.7 µM) was mixed with LA-C6-DNA (*anchor* strand, 2.15 nmol) and *conjugation 1&2* strands (2.5 nmol each). Tris(2-carboxyethyl)phosphine (TCEP; 10 µL, 100 mM) and NaCl (1.0 µL, 5 M) were added and the mixture was diluted to 100uL with 400 m tris-borate buffer (TB, pH = 7.4). The solution was mixed overnight at room temperature. TCEP (1 µL, 100 mM) and NaCl (7.5 µL, 5 M) were added and the solution was

mixed for ~8 h at room temperature. The solution was cooled to 4 °C and held there overnight. The DNA-QDs were diluted to 500 µL in borate buffer (50 mM, pH 8.5) and filtered with 30 kDa cut-off centrifugal filters (10 min, 16 900 RCF). This process was repeated until the filtrate contained no DNA (by UV-vis absorbance). The DNA-QDs were finally resuspended in 100 µL borate buffer and the concentration of QD644 and DNA were determined by UV/Vis absorbance.

Agarose gel electrophoresis: Agarose gel (1.0% w/v) was prepared in 1× TBE buffer (pH 8.3). Samples were diluted to a final volume of 15 µL in TBE with 25% v/v glycerol. Sample (12.5 µL) was added to each well and the gel was run for 30 min at ~6.7 V cm^{-1} and imaged under UV illumination.

Chapter 5: Ionic Ligands for Development of a Quantum Dot Protease "Nose" Sensor Array

5.1 Introduction

A key feature of conventional biosensors is specificity—the ability of the sensor to respond to the target analyte while remaining non-responsive to other compounds. Eliminating non-specific interactions with a sensor allows for detection of the target analyte in complex biological matrices. This paradigm is useful for sensitive detection of specific analytes but can be challenging to implement in real biological samples due to the abundance of similar biomolecules present. Furthermore, sensors with single-target specificity need to be designed individually for targets, meaning detection of *n* targets requires the use of *n* different sensors. One strategy to improve on this design is the use of semi-selective sensors to identify analytes or classify samples. Instead of interacting with one specific analyte, a semi-selective sensor interacts with multiple analytes to varying degrees. A unique pattern of response from an array of semi-selective sensors can be used to identify a number of analytes that exceeds the number of elements in the sensor array. The arrays can also be used to categorize a sample (*e.g.* healthy or diseased). With training of the sensor arrays, this application is even possible without knowing the identities of the relevant analytes. This type of response pattern from a semi-selective sensor array is modelled after the functioning of the mammalian olfactory system and has hence been dubbed a 'chemical nose' [173]. The interesting and adaptable surface properties and signalling abilities of luminescent nanoparticles make them potential materials for use in chemical nose systems [174].

Quantum dot (QD)-based chemical noses have been developed for a range of bioanalytical targets, including proteins [175,176], nucleobases [177], heavy metal ions [178], and small molecules [179,180]. The individual elements of the sensor arrays comprise QDs with different surface chemistries that have differing non-specific interactions with the analytes. The patterns of responses for the different target compounds are typically discriminated through chemometric methods (*e.g.* linear discriminant analysis).

Proteases are enzymes that catalyze the hydrolysis of proteins into smaller peptides or single amino acids. Proteolysis plays a pivotal role in a wide variety of biological processes, often regulating the activity and localization of other proteins [181]. Dysregulation of proteases has been shown to be an important factor in many diseases including cancer, Alzheimer's disease, and AIDS [182]. Serine proteases are the largest known family of proteolytic enzymes, characterized by a serine residue in their active site. The role of these proteases in processes such as blood coagulation, apoptosis, and inflammation make them useful bioanalytical targets [183]. Regulation of the activity of proteases is critical to their roles in biological processes, meaning useful analysis of proteases requires measurement of their activities rather than just their concentrations. A wide range of assays for sensing the activity of proteases has been developed using electrochemical [184], surface-enhanced Ramen scattering [185], surface plasmon resonance [186], colorimetric [187], mass spectroscopy [188], and fluorescence [189] based methods. These assays all rely on the proteolysis of substrate peptides by the protease analytes to induce a signal change. Fluorescence assays typically employ modulation of FRET-sensitized emissions from a fluorophore conjugated to one end of the cleavable substrate peptide [190–192]. QDs are well

suited to act as FRET donors for these applications due to their desirable luminescent properties and the ability to conjugate peptides directly to their surfaces.

One strategy for the detection and identification of proteases is to use peptides sequences that are specifically hydrolyzed by a target protease. The general utility of this strategy is limited by the number of proteases that share specificity for a given peptide sequence. A sensor array-based assay which successfully differentiates between proteases must therefore employ other elements to enable differentiation of protease analytes. Previous work from our group has shown that different small molecule ligands have a significant effect on the rate of proteolysis of substrate peptides conjugated to the surface of QDs [193,194]. Surface ligands can have diverse effects on the activity of different proteases [195] indicating that a QD-based chemical nose for the analysis of proteases is achievable.

A long-term aim of the group is the development of a QD-based protease-nose for the differentiation of serine proteases. The use of different peptide sequences allows for differentiation of some of these proteases but is not enough to differentiate a full panel of tested proteases (unpublished work by Katherine Krause). Achieving a functioning chemical nose for a wide variety of serine proteases necessitates a selection of surface ligands with differing chemical properties. The active site of a serine protease typically contains a pocket—called the oxyanion hole—which stabilizes the oxyanion intermediate of the substrate peptide during hydrolysis [196]. It was hypothesized that headgroups on QD surface ligands would interact with the protease exosites, and/or other features on their exterior surface, leading to significant differences in activity between the different proteases. This project focused on the development of several dihydrolipoic acid (DHLA)-based ligands with charged headgroups—sulfate, phosphate, and

trimethylammonium—toward the differentiation of serine proteases in a chemical nose sensor array.

5.2 Ligand Synthesis and Characterization

DHLA readily binds to nanoparticle surfaces through thiol-metal bonding to produce colloidally stable aqueous QDs, making it a useful basis for the development of a ligand library. Conjugation to the distal carboxylic acid group of DHLA allows for the synthesis of DHLA-based ligands with diverse functionalities, leading to a range of QD surface chemistries. Several DHLA-based ligands (Figure 5.1a) were designed (by Katherine Krause and Tiffany Jeen) to provide a range of ionic functional groups at the QD surface. The ligands were synthesized with the dithiolane ring of the lipoic acid (LA) starting material intact due to the tendency of thiols to reoxidize or undergo unwanted side reactions. The ligands were reduced to their dithiol forms immeditatly prior to ligand exchange (Figure 5.1b). Lipoic acid derivatives with distal phosphate and sulfate groups (PO_4-LA and SO_4-LA) were successfully synthesized via a LA-NHS ester intermediate (Figure 5.1c). Synthesis of a lipoic acid derivative with a distal trimethylammonium group (Me_4N-LA) was attempted via Steglich esterification (Figure 5.1d) where the synthesis appeared successful but the coating of QDs did not.

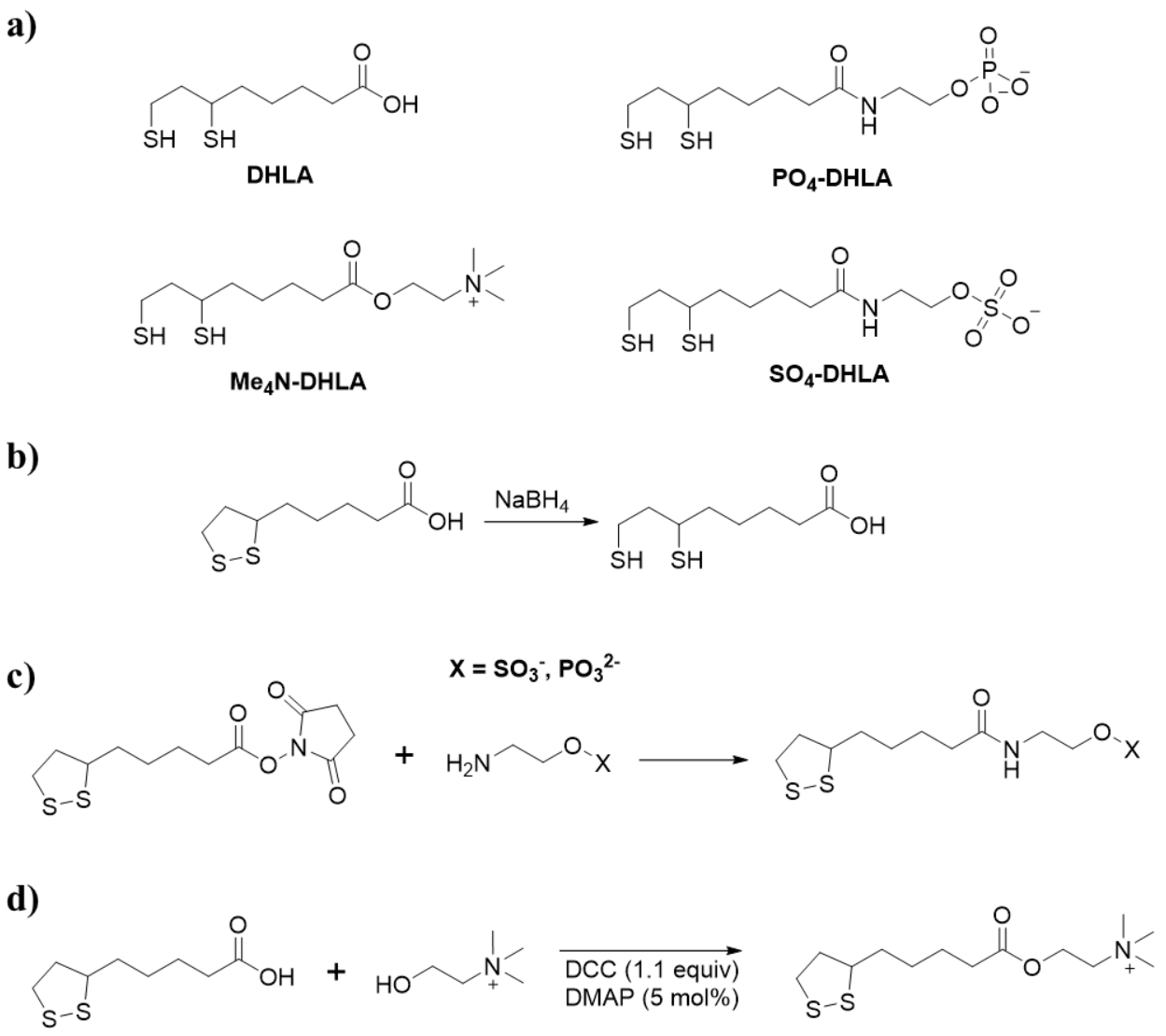

Figure 5.1 Charged QD ligands. **(a)** Dihydrolipoic acid (DHLA) and the proposed DHLA-based ionic ligands. **(b)** The ligands are reduced to their dihydro forms before ligand exchange. Synthetic pathways for **(c)** PO_4-LA and SO_4-LA, and **(d)** for Me_4N-LA.

The synthesized ligands were characterized by nuclear magnetic resonance (NMR), mass spectroscopy (MS), and thin layer chromatography (TLC) to confirm their identity and purity (see Section 5.6 and Appendices Figure B1 ^{1}H NMR spectrum of SO_4-LAB.1, B.2, and B.5**Error!**

Reference source not found.). This characterization data for SO_4-LA matched the expected results with no obvious signs of significant impurities or starting materials present. MS measurement (Figure B17) revealed the desired product at 328.0 m/z, and ^{1}H (Figure B1) and ^{13}C (Figure B4) NMR showed the correct pattern of peaks with only minor impurities present. MS data for PO_4-LA (Figure B18) revealed the intended product (328.0 m/z) along with a significant amount of dimer (657.0 m/z) and trimer (986.0 m/z) species, while the compound showed very low mobility by TLC (R_f = 0.07). This data indicates polymerization of the compound via intermolecular disulfide bond formation. As the ligands are reduced to dithiols prior to use, this polymerization does not affect the suitability of the compound for coating QDs. NMR data were collected for the ligand after reduction with $NaBH_4$ (Figure B2, Figure B5) and showed the expected pattern of peaks for PO_4-DHLA, albeit with inconsistent integration results (perhaps due to incomplete reduction of the ligand) and significant unknown impurities present. The identity of Me_4N-LA was confirmed by MS (291.1 m/z; Figure B19) and NMR (Figure B3, Figure B6), though both methods revealed that a significant amount of choline chloride starting material was present. This impurity could likely be removed by running the compound through a silica plug, as the product showed significant mobility on TLC (R_f = 0.25). Choline chloride was not thought to have a significant effect on the QD functionalization step, and the product was used without further purification.

5.3 Functionalization of QDs

Conjugation of the ligands to QD surfaces was accomplished via aqueous ligand exchange reactions (see section 5.6). Successful displacement of the hydrophobic ligands was indicated by

phase transfer of the QDs from the organic phase ($CHCl_3$) to the aqueous phase. QDs coated with PO_4-DHLA directly from the organic phase were found to be colloidally unstable, perhaps due to a lower ligand surface density caused by electrostatic repulsion between the doubly-charged phosphate groups or poor organic solubility of the ligand. Aqueous ligand exchange starting from histidine (His)-coated QDs produced colloidally stable PO_4-DHLA-QDs (Figure 5.2). The QD surface binding by His is much weaker than that of DHLA-based ligands, allowing these ligands to displace His when added in excess. Displacement of the His ligands was evident from the difference in electrophoretic mobility between the His-QD starting material and the PO_4-DHLA-QD product (Figure 5.2), indicating a significant difference in surface charge. Me_4N-DHLA-QDs were also produced by ligand exchange with His-QDs but had unexpected electrophoretic mobility (Figure 5.2). The positively-charged quaternary nitrogen on the Me_4N-DHLA should have led to an overall positive charge for Me_4N-DHLA-QDs, leading to migration towards the negative terminal (*i.e.* upwards). The mobility of Me_4N-DHLA-QDs was approximately equivalent to that of the negatively charged ligands (SO_4-DHLA, PO_4-DHLA, and DHLA), indicating that either the ligand was not efficiently conjugating to the QD surface or that the positively charged product species had become negatively charged at some stage of the process (Figure 5.2).

FTIR spectra were recorded for the neat ligands and for the ligand-coated QDs to confirm the presence of the desired ligand on the QD surfaces. Though broadening of the features in the QD samples makes analysis of the fine spectral features difficult, some features of the spectra for SO_4-LA (Figure B7) and PO_4-LA (Figure B8) were retained in their respective QD conjugates (Figure B14 and Figure B15). Most notably, the N-H stretches at ~3310-3285 cm^{-1} and the C-H stretches at 2935-2920 cm^{-1} appeared in the spectra of both the neat ligands and the QD conjugates. The IR

spectra for Me_4N-LA (Figure B9) and Me_4N-DHLA-QDs (Figure B16), on the other hand, did not have any discernable common fine features, though more intense broadening of the QD conjugate spectrum made identification of any fine features impossible. In all cases, significant changes from the QD starting materials (Figure B10 for SO_4-DHLA-QDs and Figure B11 for PO_4- and Me_4N-DHLA-QDs) were observed. This data, though not conclusive, give further evidence that surface coating of the Me_4N-DHLA-QDs is not the desired species.

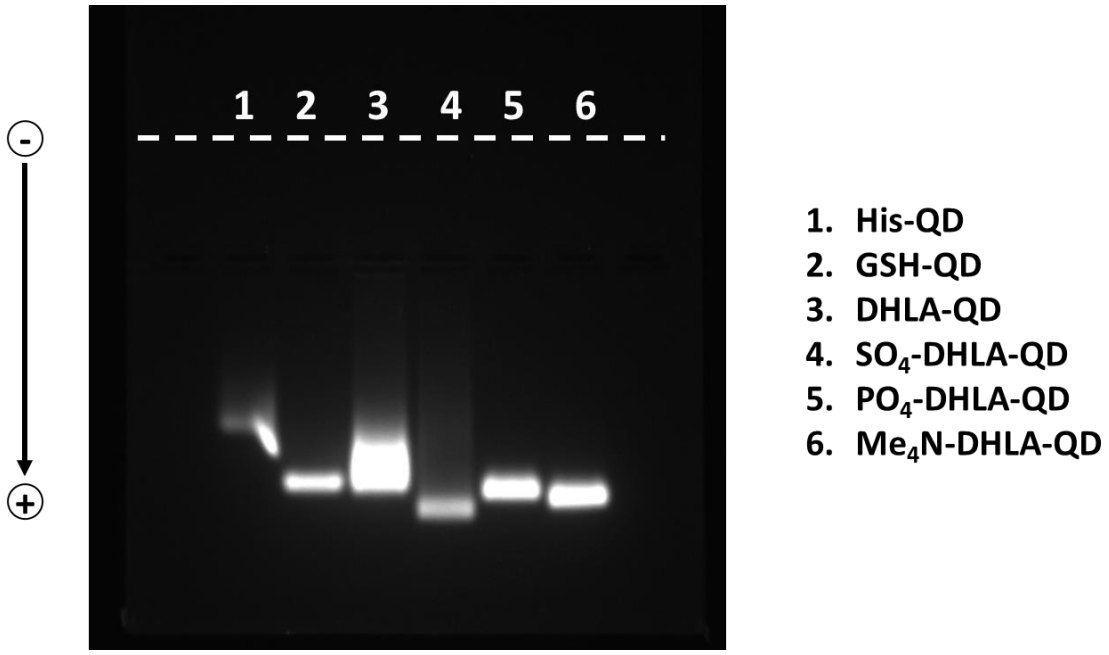

Figure 5.2 Agarose gel electrophoresis of the DHLA derivative ligands conjugated with QDs. The DHLA-based ligands coating all produced relatively stable, negatively charged QDs as indicated by the minimal streaking and migration towards the positive terminal.

5.4 Effects of QD Surface Chemistry on Proteolysis

The effects of the three DHLA-based ligands on proteolysis at the QD surface were investigated in comparison to glutathione (GSH)- and DHLA-QDs, with the caveat that the exact identity of the surface ligands in the Me_4N-DHLA-QDs is unknown. The proposed protease nose sensor array uses the initial rates of proteolysis of QD-peptide conjugates to detect different proteases (Figure 5.3). The peptides have poly-histidine tags at their N-termini to bind to the QD surface and were labelled with sulfo-cyanine 5 (s-Cy5) at their C-terminus. This fluorescent dye is a suitable FRET acceptor for the QDs (emission max at 605 nm, Figure 5.3b), allowing peptide cleavage to be monitored by the change in s-Cy5-to-QD emission ratio (Figure 5.3c) [193,197]. To account for any photobleaching of the dye or photobrightening of the QDs, the s-Cy5:QD emission ratio for a given sample was divided by the s-Cy5:QD ratio for a blank sample (*i.e.* no protease added) at each time point. The progress curves generated from this data were fitted with a monoexponential decay function from which initial rates were calculated (Figure 5.3d-e).

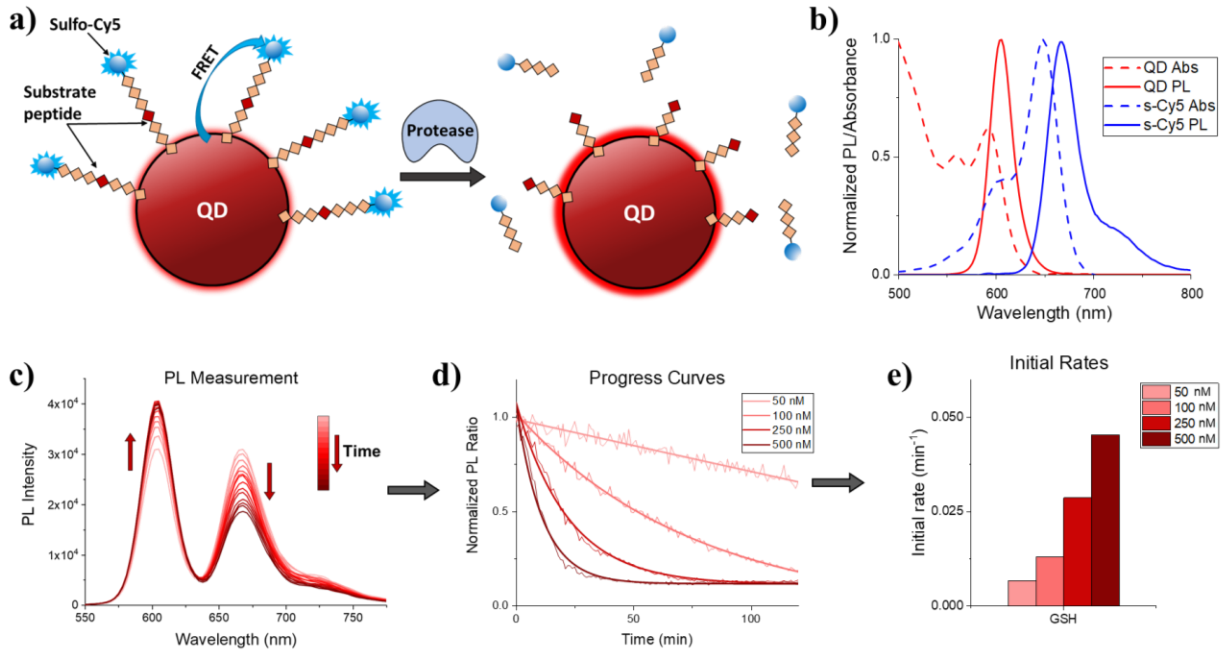

Figure 5.3 Protease initial rate determination by QD-s-Cy5 FRET. **(a)** Dye-labelled peptides conjugated to the QD surface are hydrolyzed by the protease, releasing the dye-labelled end into solution (Note: QD ligands are omitted here for clarity). **(b)** The spectral overlap between the QD and dye (s-Cy5) allows the QD to act as a FRET donor, sensitizing the dyes emission. **(c)** After protease addition, the s-Cy5 signal (λ_{max} = 670 nm) decreases as the QD signal (λ_{max} = 605 nm) increases with peptide cleavage. The s-Cy5 to QD PL ratio for each protease concentration level is normalized against a blank sample (no protease added), and the resulting data is used to plot **(d)** progress curves for each protease concentration level from which **(e)** the initial rates are calculated.

The peptide sequences (designed by Tiffany Jeen) have a common sequence apart from a single amino acid substitution at the recognition site (Table 5.1). The tested proteases have previously been shown to have varying levels of activity to the different peptides (unpublished work from Katherine Krause). Certain sets of the tested proteases—chymotrypsin and elastase, endoproteinase LysC and plasmin, proteinase K and subtilisin and papain—have proved difficult to differentiate by their response to the different substate peptide sequence alone when conjugated

to GSH-QDs. SO_4-DHLA-, PO_4-DHLA-, and Me_4N-DHLA-QDs, along with DHLA- and GSH-QDs, were conjugated with non-specific substrate peptide sequences to evaluate the efficacy of the ligands for differentiating between these proteases.

Table 5.1 Sequences of the substrate peptides and the corresponding proteases which were tested against them. The arrow indicates the hydrolysis site.

Peptide	Sequence	Proteases
ns.K	H_6GP_5GSDGNEGNL**K**↓GSGC	Endoproteinase LysC and plasmin
ns.Y	H_6GP_5GSDGNEGNL**Y**↓GSGC	Chymotrypsin, elastase, proteinase K, subtilisin, and papain

Proteolytic activities were measured for each combination of protease, protease concentration, and QD surface chemistry in duplicate to calculate the initial rates of proteolysis (See Appendix B.6 for progress curves). Most progress curves show an exponential decline in the PL ratio from t=0 and are well modeled (empirically) by an exponential decay function (Figure 5.4a). For some samples with significantly lower proteolytic rates, however, the changes in signal were better modelled by linear equations (Figure 5.4b). Experimental determination of the initial rates for plasmin with the QDs coated with DHLA-based ligands proved impractical as the generated progress curves showed very rapid but incomplete proteolysis (*i.e.* the majority of the peptide cleavage occurred before the measurement of the first data point). This is likely due to non-specific interactions between the surface ligands and the proteases (*e.g.* adsorption of the protease to the QD surface), inhibiting the protease activity after the initial period. Previous research from the group has shown similar results with plasmin (among other proteases). These results have been

attributed to a 'scooting' mode of proteolysis, where the protease hydrolyses all of the peptides on a QDs surface but is then unable to move to another QD due to adsorption, leading to the non-convergent progress curves [198]. Progress curves for plasmin with GSH-QDs showed more typical exponential decay, likely due to weaker interactions between GSH and the protease (Figure B16).

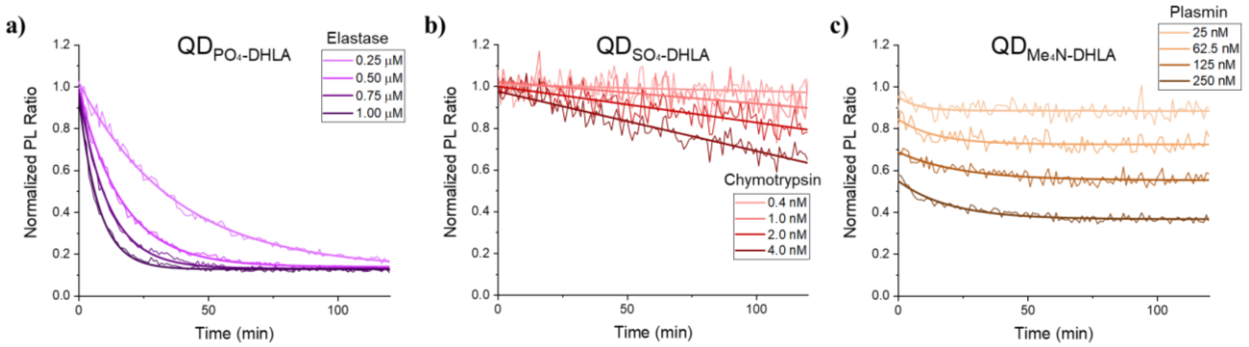

Figure 5.4 Example progress curves for proteolytic activity at QD surfaces. **(a)** Progress curve fit with a monoexponential decay function (*e.g.* elastase with PO_4-DHLA-QDs). **(b)** Samples with lower activity were more accurately modelled with a linear function (*e.g.* chymotrypsin with SO_4-DHLA-QDs). **(c)** Measurement for plasmin with the DHLA surface chemistries resulted in incomplete cleavage (*e.g.* plasmin with Me_4N-DHLA-QDs), likely due to non-specific interactions between the protease and the ligand-coated QD surface.

The patterns of initial rates of the different surface chemistries for each set of proteases were evaluated to determine the efficacy of these surface chemistries for differentiating the proteases (Figure 5.5). SO_4-DHLA-QDs generally produced the least protease activity, with measured rates significantly lower than those of GSH-, PO_4-DHLA- and Me_4N-DHL-QDs for all the tested proteases (Figure 5.5), and lower than DHLA for several (subtilisin and proteinase K). This

inhibiting effect on the proteolysis is potentially related to the direct inhibition of some serine proteases (*e.g.* thrombin) by sulfate-containing molecules (*e.g.* heparin) [199]. The sulfate groups affect enzyme activity, in part, by binding to the enzyme surface, inhibiting its ability to cleave the peptides. The very low activity of some proteases with SO_4-DHLA is useful in the context of a protease nose sensor array, as larger differences in activities between QD ligands for a given protease provide a more robustly identifiable activity profile. For example, the pattern of initial rates of chymotrypsin and elastase on PO_4-DHLA- and Me_4N-DHLA-QDs are significantly different, but the relatively small difference between the rates makes this difference a less reliable identification tool. The stark difference in response patterns for chymotrypsin and elastase between SO_4-DHLA- and PO_4-DHLA-QDs would provide a more robust method of identification.

PO_4-DHLA and Me_4N-DHLA significantly accelerated the rate of proteolysis compared to the other tested ligands in several cases (Figure 5.5). This apparent enhancement of protease activity is potentially very useful for sensitive detection of low-abundance proteases. For PO_4-DHLA, this increased activity may be related to the similarity between the PO_4-DHLA coated QD surface and the phospholipid membranes of cells. Though the phospholipids of biological membranes typically contain other functionalities at the phosphate headgroups (*e.g.* phosphatidylserine, phosphatidylcholine, etc.), it may be the case that the PO_4-DHLA covered surface more closely mimics a biological environment to which the proteases are adapted, leading to accelerated proteolysis. As the exact identity of the Me_4N-DHLA ligand is unknown, it is impossible to speculate on the mechanism of its accelerating effects on the protease activities.

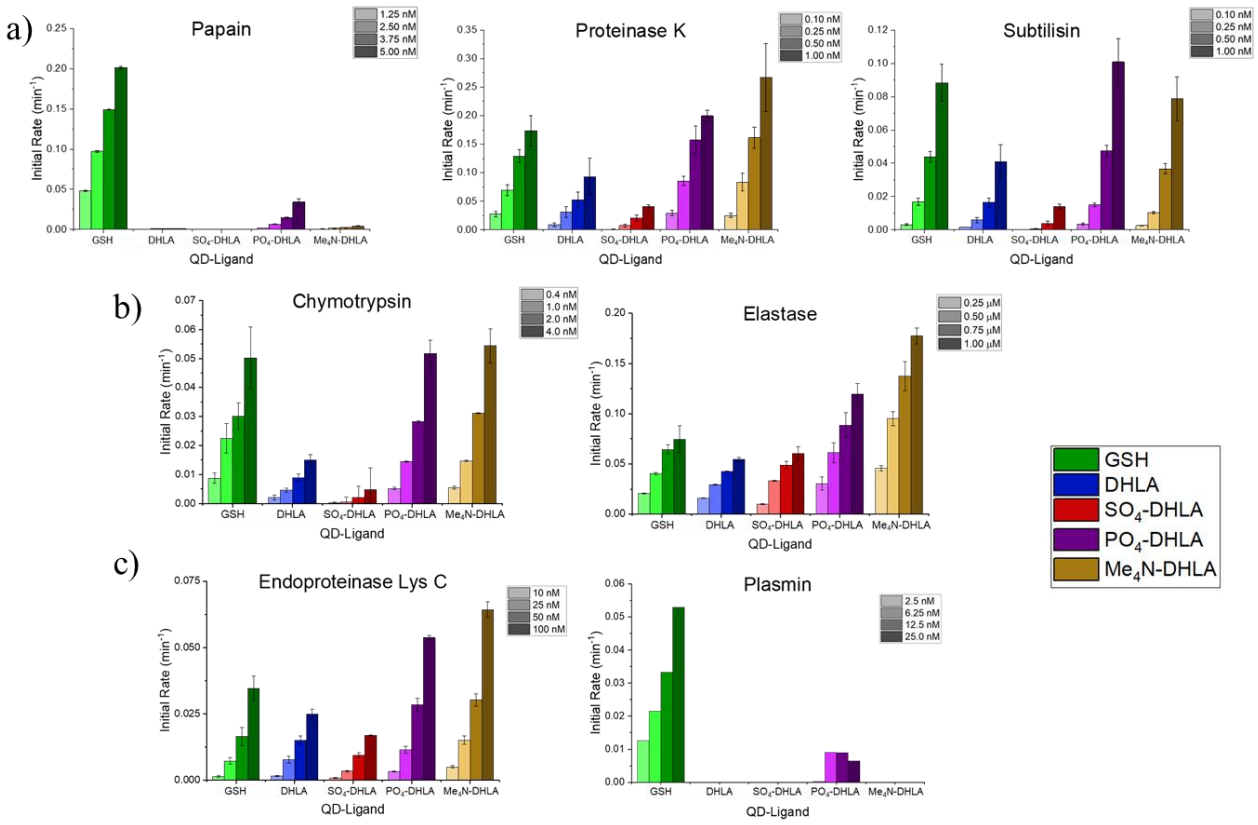

Figure 5.5 Response patterns for the tested sets of serine proteases: **(a)** papain, proteinase K, and subtilisin, **(b)** chymotrypsin and elastase, and **(c)** endoproteinase Lys C and plasmin. Error bars represent standard deviation between two replicate measurements.

Importantly, the pattern of initial rates between the five different tested ligand coatings was unique for the protease sets of papain, subtilisin, proteinase K (with ns.Y substrate; Figure 5.5a); chymotrypsin and elastase (with ns.Y substrate; Figure 5.5b); and plasmin and endoproteinase LysC (with ns.K substrate; Figure 5.5c). Previous results (unpublished work by Katherine Krause) have shown that chymotrypsin and elastase exclusively cleave ns.Y, while papain, subtilisin, and proteinase K cleave four tested substrate peptides (including ns.Y and ns.K), hence the separation of these two sets of proteases. It should be noted that the initial rate determination for plasmin was

not successful for many of the DHLA-based ligands, likely due to non-proteolytic interactions between the QDs and the enzyme (*vida supra*). These unique 'fingerprint' patterns are critical to the proper functioning of the protease nose. For subtilisin and proteinase K, these fingerprint patterns were relatively similar, and these proteases would likely require an additional sensor element to be properly differentiated. The stark difference between the accelerating effect of PO_4-DHLA and Me_4N-DHLA and the inhibitory effect of SO_4-DHLA on protease activity makes them promising elements for a sensor array. In most cases, however, PO_4-DHLA- and Me_4N-DHLA-QDs produced quite similar rates of proteolytic cleavage, meaning the two surface chemistries would be redundant in a sensor array. The combination of the SO_4-DHLA and PO_4-DHLA ligands developed here, along with QD ligands being developed by other group members, will likely produce a sensor array capable of distinguishing the entire panel of serine proteases.

5.5 Conclusions

The three proposed DHLA-based ligands with charged headgroups were successfully synthesized and tested as candidate surface ligands for a QD-based protease nose sensor array. SO_4-DHLA- and PO_4-DHLA-QDs were successfully produced and proved to be useful elements for the proposed sensor array. Me_4N-DHLA-QDs were produced, but characterization data (*i.e.* gel electrophoresis and FTIR) revealed that the resulting QDs were likely not coated with the correct ligand. Despite this, the purported Me_4N-DHLA-QDs were shown to have an accelerating effect on proteolysis at the QD surface. The proteases of the three tested sets (papain, subtilisin, proteinase K; chymotrypsin and elastase; and plasmin and endoproteinase LysC) all produced

unique fingerprint response patterns with the five different QD surface chemistries (including GSH and DHLA), allowing differentiation of the proteases within the sets.

5.6 Experimental Methods

Materials: CdSe/ZnS QD605s were synthesized with Kelly Rees. L-glutathione (reduced), histidine, 2-aminoethyl sulfate, *o*-phosphorylethanolamine, and choline chloride were from Sigma Aldrich (Oakville, ON). Peptides were from Bio-Synthesis Inc. (Lewisville, TX) and were labelled by Tiffany Jeen and Katherine Krause. Human plasmin was from Haematologic Technologies (Essex Junction, VT). Subtilisin A (Type VIII) and α-Chymotrypsin (Type II, from bovine pancreas) were from Sigma Aldrich. Elastase, Proteinase K, and Papain were from Worthington Biochemical Corporation (Lakewood, NJ). Endoproteinase Lys C was from New England BioLabs (Ipswitch, MA).

Instruments:

PL and absorption spectral measurements were made with an Infinite M1000 Pro plate reader (Tecan Ltd., Morrisville, NC). Gel images were collected with a GelDoc XR Gel Documentation System (Bio-Rad Laboratories Ltd., Hercules, CA). ImageJ software (NIH, Bethesda, MD) was used for processing images.

Ligand Synthesis:

Synthesis of LA-NHS: See Section 4.5.

Synthesis of SO_4-LA.

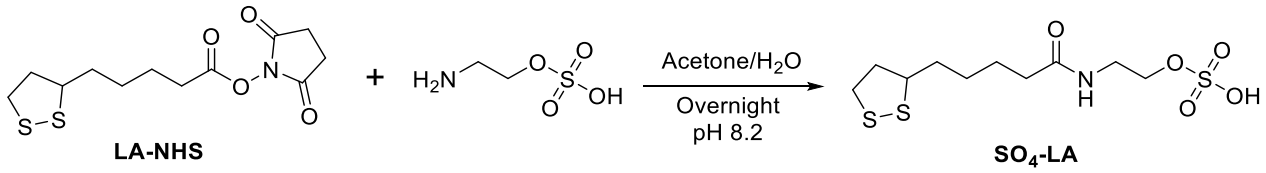

LA-NHS (250 mg, 0.819 mmol) was dissolved in 20 mL of acetone. 2-aminoethyl sulfate (133 mg, 0.942 mmol) was dissolved in a sodium bicarbonate solution (10 mL, 200 mM) and added to the solution of LA-NHS. The mixture was stirred overnight at room temperature. The solution was diluted with 10 mL water and washed three times with ether. The aqueous layer was acidified to a pH of ~2 with HCl (aq, 1 M) and then extracted into butanol (45 mL in three portions). The organic layer was washed with a saturated sodium bicarbonate solution, then with water. The organic layer was evaporated to dryness under vacuum to give a pale-yellow powder (176 mg, 66% crude yield). ^{1}H NMR (D_2O, 400 MHz): δ 4.02 (t, 2 H), 3.41 (t, 2 H), 3.18-3.08 (m, 2 H), 2.44-2.37 (m, 1 H), 2.20 (t, 2 H), 1.96–1.87 (m, 1H), 1.72-1.61 (m, 1H), 1.60-1.50 (m, 3H), 1.39-1.31 (m, 2H). ^{13}C NMR (CD_3OD, 400 MHz): δ 177.2, 67.1, 56.4, 40.2, 38.7, 38.1, 35.5, 33.7, 27.7, 24.9. FTIR ν_{max}/cm^{-1} 3306 (N-H), 2927 and 2856 (C-H), 1631s (C=O). TLC (DCM:MeOH 4:1): R_f = 0.58. ESI-TOF MS (neg; m/z): calcd for $C_{10}H_{18}NO_5S_3^-$ 328.0, found 328.0 [M –].

Synthesis of PO_4-LA.

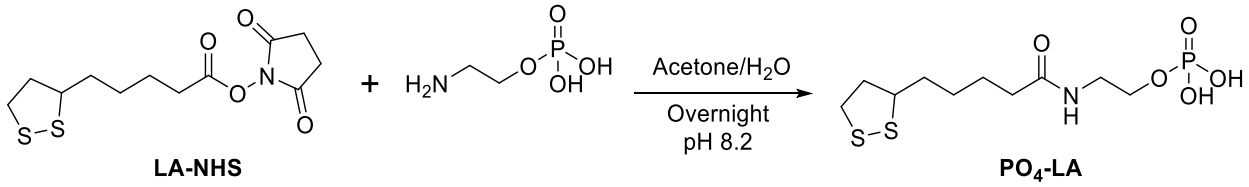

LA-NHS (503 mg, 1.66 mmol) was dissolved in 20 mL acetone. *O*-phosphorylethanolamine (257 mg, 1.82 mmol) was dissolved in a solution of sodium bicarbonate (20 mL, 100 mM) and the pH was adjusted to 8.2 with NaOH (aq, 1 M). The solutions were combined and mixed overnight at room temperature. The solution was washed three times with ether. The aqueous layer was acidified to a pH of ~2 with HCl (aq, 1 M) and then extracted into butanol (45 mL in three portions). The volume of the organic layer was reduced to ~25% under vacuum and ~15 mL of isopropanol was added. This was repeated four times before the solvent was evaporated to dryness. The resulting product was dried under high vacuum for ~2 h to give an orange oil (505 mg, 93% crude yield). ^{1}H NMR (D_2O, 400 MHz): δ 3.93 (m, 1 H), 3.74 (m, 2 H), 3.30 (t, 2 H), 2.89 (m, 1 H), 2.56 (m, 2 H), 2.20 (t, 2 H), 1.82 (m, 1 H), 1.72-1.61 (m, 1H), 1.60-1.50 (m, 3H), 1.39-1.31 (m, 2H). ^{13}C NMR (CD_3OD, 400 MHz): δ 177.2, 64.3, 62.2, 40.6, 38.8, 37.8, 35.6, 34.2, 25.7, 21.7. FTIR ν_{max}/cm^{-1} 3312br (N-H), 2933 and 2860 (C-H), 1707s (C=O). TLC (DCM:MeOH 4:1): R_f = 0.07. ESI-TOF MS (neg; m/z): calcd for $C_{10}H_{19}NO_5S_2P^-$ 328.0, found 328.0 [M –].

Synthesis of Me_4N-LA.

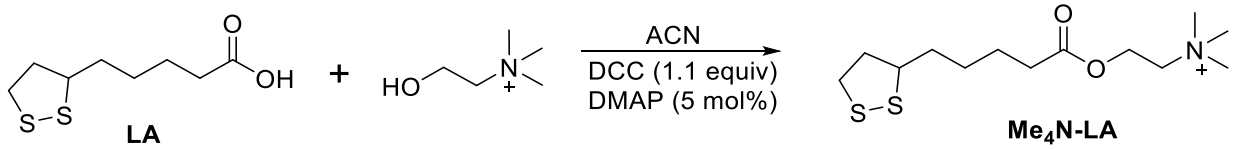

Lipoic acid (103 mg, 0.499 mmol) and choline chloride (76 mg, 0.54 mmol) were mixed in 20 mL acetonitrile (ACN) on ice. N,N'-Dicyclohexylcarbodiimide (DCC; 104 mg, 0.502 mmol) was dissolved in 1 mL ACN and added to the solution which was stirred for 10 min. 4-Dimethylaminopyridine (DMAP; 3.1 mg, 0.025 mmol) was dissolved in 1 mL ACN and added to the solution. The solution was stirred on ice for 30 min before being warmed to room temperature and stirred overnight. The solution was filtered to remove precipitate and the solvent was evaporated to ~5 mL under vacuum. Diethyl ether was added to precipitate the product which was collected by vacuum filtration and dissolved in ACN. The solvent was evaporated to dryness under vacuum to yield a yellow oil (93 mg, 64% crude yield inclusive of choline chloride and DMAP). ^{1}H NMR (D_2O, 400 MHz): δ 4.50 (m, 2 H), 3.68 (dd, 2 H), 3.64 (m, 1 H), 3.13 (s, 6 H), 2.44 (m, 1 H), 2.41 (t, 2 H), 1.97–1.90 (m, 1H), 1.72-1.62 (m, 1H), 1.60-1.52 (m, 3H), 1.42-1.36 (m, 2H). ^{13}C NMR (CD_3OD, 400 MHz): δ 175.5, 67.4, 64.6, 58.3, 53.9, 53.8, 53.7, 40.3, 38.1, 33.7, 33.4, 27.9, 23.8. FTIR ν_{max}/cm^{-1} 3019, 2929, and 2860 (C-H), 1735s (C=O). TLC (DCM:MeOH 4:1): R_f = 0.25. ESI-TOF MS (pos; m/z): calcd for $C_{13}H_{26}NO_2S_2^+$ 292.1, found 292.2 [M +].

Histidine ligand exchange: Histidine (His; 20 mg, 0.13 mmol) was dissolved in 100 µL of methanolic tetramethylammonium hydroxide (TMAH; 25% w/w TMAH). QDs (20 µL, 1.0 nmol) were diluted to 200 µL in $CHCl_3$ and mixed with the His solution at room temperature for 1 h. Borate buffer with salt (100 µL, 50 mM, 250 mM NaCl, pH 8.5) was added, the mixture was vortexed, and the sample was left to allow the phases to separate. The aqueous phase was removed and the QDs were precipitated by addition of ethanol and centrifuged for 5 min (5000 RCF). The pellet was resuspended in borate buffer with salt and precipitated with ethanol twice more before a final resuspension in borate buffer (BB; 50 mM, pH 8.5).

SO_4-DHLA ligand exchange: SO_4-LA (33 mg, 0.10 mmol) was dissolved in 100 µL water and a solution of $NaBH_4$ (11 mg, 0.29 mmol in 100 µL of water) was added dropwise. The reaction was mixed and left at room temperature for 20 min before being quenched with 200 µL acetone. Excess acetone (additional 600 µL) was added and the solution was centrifuged for 5 min (17 000 RCF). The supernatant was removed, and the pelleted SO_4-DHLA was dissolved in 400 µL BB. QDs (1.0 nmol) were precipitated from chloroform three times by addition of acetone and centrifugation for 10 min (17 000 RCF), before a final resuspension in 500 µL of chloroform. The SO_4-DHLA solution was combined with the QD solution in chloroform, and 200 µL of methanolic TMAH was added. The reaction mixture was covered from light, vortexed, and mixed for 90 min at room temperature. BB (200 µL) was added to the reaction mixture and the aqueous layer was separated. SO_4-DHLA-QDs were collected via spin filtration (30 kDa MWCO filter) and washed three times with BB (500 µL). The QDs were then transferred to a microcentrifuge tube and diluted with BB to ~300 µL and stored at 4 °C until use.

PO_4-DHLA Ligand Exchange: PO_4-LA (40 µmol) was dissolved in 100 µL water and a solution of $NaBH_4$ (11 mg, 0.29 mmol in 100 µL of water) was added dropwise. The reaction was mixed and left at room temperature for 20 min before being quenched with 200 µL acetone. Excess acetone (additional 600 µL) was added and the solution was centrifuged for 5 min (17 000 RCF). The reduced ligand (PO_4-DHLA) was dissolved in bicarbonate buffer (100 µL, 100 mM, pH 8.5). An aliquot of His-QDs (1.0 nmol) was diluted with bicarbonate buffer (to 400 µL) and the reduced ligand solution was added. The mixture was vortexed, covered from light, and incubated at 37 °C for 3 h. The PO_4-DHLA-QDs were collected via spin filtration (30 kDa MWCO filter) and washed three times with bicarbonate buffer (500 µL). The QDs were then transferred to a microcentrifuge tube and diluted with bicarbonate buffer to ~300 µL and stored at 4 °C until use.

Me_4N-DHLA Ligand Exchange: Me_4N-LA (40 µmol) was dissolved in 100 µL water and the solution was centrifuged for 5 min (17 000 RCF) to remove residual diisopropyl urea (DIU). The supernatant was transferred to a separate tube and a solution of $NaBH_4$ (11 mg, 0.29 mmol in 100 µL of water) was added dropwise. The reaction was mixed and left at room temperature for 20 min before being quenched with 200 µL acetone. Excess acetone (additional 600 µL) was added and the solution was centrifuged for 5 min (17 000 RCF). The reduced ligand (Me_4N-DHLA) was dissolved in bicarbonate buffer (100 µL, 100 mM, pH 8.5). An aliquot of His-QDs (1.0 nmol) was diluted with bicarbonate buffer (to 400 µL) and the reduced ligand solution was added. The mixture was vortexed, covered from light, and incubated at 37 °C for 3 h. The Me_4N-DHLA-QDs were collected via spin filtration (30 kDa MWCO filter) and washed three times with bicarbonate buffer (500 µL). The QDs were then transferred to a microcentrifuge tube and diluted with bicarbonate buffer to ~300 µL and stored at 4 °C until use.

Peptide conjugation: Ligand coated QDs in BB were mixed with 8 molar equivalents of dye-labelled peptides. The reaction mixture was covered from light and mixed at room temperature for 2 h then stored at 4 °C until use.

Protease kinetics: Proteases were diluted to the twice the desired concentrations in 1X Dulbecco's phosphate buffered saline (DPBS; 137 mM NaCl, 2.7 mM KCl, 8.9 mM Na_2HPO_4, and 1.5 mM KH_2PO_4, pH 7.4) and 20 µL of each were added to wells in a black polystyrene 384-well plate. QD-peptide conjugates were diluted to 200 nM with 1X DPBS and 20 µL was added to each of the wells and the plate was quickly transferred to the plate reader for fluorescence measurements. PL emission intensity of the QD (at 605 nm) and s-Cy5 (at 670 nm) were measured with excitation at 405 nm. Excitation and emission bandwidths were 7 nm. PL measurements were taken every 1 min over 120 min as the mixtures reacted at room temperature in the plate reader. Duplicate measurements were made using the same hydrophobic ligand-functionalized QD batches but with the peptide conjugation done separately and proteolytic measurements made on separate days.

Initial rate determination: Progress curves were generated from the PL intensity data by dividing the ratio of dye:QD emission from each sample by the dye:QD emission ratio of a blank sample (without protease) for each time point [193,197]. Normalization to the blank sample reduces the effect of any non-proteolytic processes, such as photobleaching of the dye or photobrightening of the QDs. The resulting data was fit with an exponential decay function using OriginPro to determine the initial rates.

Chapter 6: Conclusions and Future Work

6.1 Thesis Overview

The work described in this thesis explores the development of several novel fluorescent DNA logic gate designs. DNA logic gates have potential to produce efficient sensors which give more direct information than traditional sensing devices. The proposed AND gate protease sensor could simultaneously deliver information on both the presence and activity of a target protease, providing more reliable detection of active targets and reducing the rate of false positives. To be effective, these systems require good separation of the TRUE and FALSE signal states (*i.e.* high signal contrast), and amplification of output signals is an important goal. The use of enzymes to produce this amplification can be effective but imposes significant limitations on the adaptability of these systems. Two different logic gate systems were designed and tested to produce non-enzymatic amplification. Tuning of the energetics of the many oligonucleotide components of the systems to produce the desired response while maintaining stability proved to be a significant challenge. Further development and optimization of these designs has potential to produce effective and adaptable amplification systems for DNA logic gates.

This thesis also contributed to the development of different QD surface chemistries for the detection and differentiation of serine proteases. Protease activity at QD surfaces can be substantially different depending on the ligand which is conjugated to the QD surface. This idea has led the group towards the development of a library of QD ligands, with the eventual goal of developing a chemical 'nose' array sensor for the differentiation of proteases and detection of

diseases linked with protease biomarkers. To this end, three ionic ligands were developed and tested for their effects on protease activity and their ability to differentiate between a panel of proteases. The tested ligands, along with GSH and DHLA, were able to successfully differentiate between the different tested proteases. The two anionic ligands (SO_4-DHLA and PO_4-DHLA) are viable candidates for inclusion in a 'nose' sensor array. The nominally cationic ligand (Me_4N-DHLA) did not produce the expected cationic QDs, but showed interesting results in protease assays, and warrants further investigation.

6.2 Future Work

For the AND gate protease logic probe (Chapter 2:), efforts to develop a protease AND gate logic probe were ultimately unsuccessful. It was determined that the proposed structure-switching *aptamer-template* design was not feasible due to thermodynamic limitations imposed by the required hybridization strength to produce a stable duplex with the aptamer while incorporating a hairpin forming segment into the *template* strand. The general idea of a protease logic probe remains possible, however, and adaptation of the structure-switching aptamer template design could make this possible. Simply omitting the hairpin forming segment would allow adjustment of the *aptamer-template* hybridization strength to allow for dissociation of the duplex in the presence of thrombin. This would likely reduce the utility of the LLC in the design, as the fixed dye-LLC required for optimal signal contrast could not be achieved. Replacement of the LLC with another fluorophore could produce a functioning device, albeit likely with lower signal contrast.

For the displacement cascade logic gate amplifier (Chapter 3:), optimization of sequence design for the displacement cascade logic gate amplifier resulted in a product that showed the correct response pattern to inputs for the AND gate with reasonable signal contrast. However, this response only achieved with a short *amplifier* domain containing a single copy of the dye labelled *backbone unit* due to issues with the ligation-based synthesis. With optimization of the synthetic method, this design scheme could likely produce a functioning amplification system resulting in high contrast logic gates. It was hypothesized that issues with the behaviour of the logic gate were a result of by products that did not contain the critical *gate* strand, reducing the overall performance of the samples. Sequence specific purification is necessary to resolve this issue. This could be accomplished via magnetic pulldown using magnetic beads coated with capture oligonucleotides to specifically hybridize the *gate* strand, eliminating all sequences which do not contain this segment. Alternately, the *gate* strands could be conjugated to a solid-phase resin before ligation to allow for easy removal of any components not attached to the tethered *gate* strand. These improvements to the *logic gate* assembly would likely produce systems with larger functional displacement cascades.

For the QD-catalytic hairpin assembly logic gate (Chapter 4:), conjugation of a sufficiently high number of DNA strands per QD was the first step towards development of this logic gate system. Optimization of the conjugation procedure produced QDs with the required surface density of DNA. The design of the catalytic hairpin system, however, requires further optimization to produce a functioning logic gate. Though some catalytic behaviour was observed, the limited degree of increased hybridization in the presence of logical inputs indicates that the oligonucleotide sequences making up the system need to be redesigned. It is likely that the

assumptions made about the hybridization behaviour of the QD-conjugated DNA strand were inaccurate, and rational design of the various hybridization strengths would require better understanding of these behaviours. Future work in this area could include more fundamental studies of the effect of DNA density at QD surfaces on its hybridization behaviour. Studying the effect of different QD surface ligands, as well as the ligands used to conjugate the DNA to the QD surface, could provide valuable tools for tuning the behaviour of DNA at the nanoparticle surface.

For ionic ligands for development of a QD protease "nose" sensor array (Chapter 5:), the negatively charged SO_4-DHLA and PO_4-DHLA ligands were successfully synthesized, coated on QDs, and tested for their ability to differentiate proteases based on their effects on the proteolytic activity. Derivatives of PO_4-DHLA that include phosphate groups more closely related to those found in biological membranes (*e.g.* phosphatidylcholine or phosphatidylglycerol) are worthy synthetic targets for future studies as these compounds may have stronger effects on protease activity. The cationic Me_4N-DHLA, however, was not successfully coated on QDs. The effect on a QD with positive surface charge on protease activity would likely be significantly different then that of the more typical negatively charged ligands, making this type of ligand a worthy target for inclusion in the proposed protease nose sensor array. Further investigation of the Me_4N-DHLA ligand, including additional purification and optimization of the ligand exchange procedure, could lead to successful QD functionalization with this ligand. Purification of Me_4N-DHLA could be achieved through reverse-phase (C8- or C18-silica gel) column chromatography. Alternatively, DHLA-based ligands with other distal cationic groups (*e.g.* phosphonium or sulfonium) could be investigated. The end goal for this project is the inclusion of the chosen ligands (SO_4-DHLA and

PO_4-DHLA) in a functional protease nose sensor array, which will be able to identify unknown proteases by their unique response patterns.

Bibliography

1. Amelia, M.; Zou, L.; and Credi, A. (2010) *Coord. Chem. Rev.*, **254**, 2267–2280.

2. Wu, C.; Wan, S.; Hou, W.; Zhang, L.; Xu, J.; Cui, C.; Wang, Y.; Hu, J.; and Tan, W. (2015) *Chem. Commun.*, **51**, 3723–3734.

3. Seeman, N.C. (2007) *Mol. Biotechnol.*, **37**, 246–257.

4. Bath, J.; and Turberfield, A.J. (2007) *Nat. Nanotechnol.*, **2**, 275–284.

5. Ma, Y.; Yang, X.; Wei, Y.; and Yuan, Q. (2016) *Chinese J. Chem.*, **34**, 291–298.

6. Kuzyk, A.; Jungmann, R.; Acuna, G.P.; and Liu, N. (2018) *ACS Photonics*, **5**, 1151–1163.

7. Simmel, F.C. (2007) *Nanomedicine*, **2**, 817–830.

8. Hu, Q.; Li, H.; Wang, L.; Gu, H.; and Fan, C. (2019) *Chem. Rev.*, **119**, 6459–6506.

9. Travers, A.; and Muskhelishvili, G. (2015) *FEBS J.*, **282**, 2279–2295.

10. Hastman, D.; Diaz, S.A.; and Medintz, I.L. (2019) in *Plasmonics in Biology and Medicine XVI* (eds T. Vo-Dinh, H.-P.A. Ho, K. Ray). SPIE, pp. 41.

11. Tyagi, S.; and Kramer, F.R. (1996) *Nat. Biotechnol.*, **14**, 303–308.

12. Seelig, G.; Soloveichik, D.; Zhang, D.Y.; and Winfree, E. (2006) *Science*, **314**, 1585–1588.

13. Seeman, N.C. (1982) *J. Theor. Biol.*, **99**, 237–247.

14. Zhao, J.; Bacolla, A.; Wang, G.; and Vasquez, K.M. (2010) *Cell. Mol. Life Sci.*, **67**, 43–62.

15. Mergny, J.L.; and Sen, D. (2019) *Chem. Rev.*, **119**, 6290–6325.

16. Guo, Y.; Yao, W.; Xie, Y.; Zhou, X.; Hu, J.; and Pei, R. (2016) *Microchim. Acta*, **183**, 21–34.

17. Yakovchuk, P.; Protozanova, E.; and Frank-kamenetskii, M.D. (2006) **34**, 564–574.

18. SantaLucia, J.; and Hicks, D. (2004) *Annu. Rev. Biophys. Biomol. Struct.*, **33**, 415–440.

19. Breslauer, K.J.; Frank, R.; Blocker, H.; and Marky, L.A. (1986) *Proc. Natl. Acad. Sci. U. S. A.*, **83**, 3746–3750.

20. Andreatta, D.; Sen, S.; Pérez Lustres, J.L.; Kovalenko, S.A.; Ernsting, N.P.; Murphy, C.J.;

Coleman, R.S.; and Berg, M.A. (2006) *J. Am. Chem. Soc.*, **128**, 6885–6892.

21. Seeman, N.C.; and Kallenbach, N.R. (1994) *Annu. Rev. Biophys. Biomol. Struct.*, **23**, 53–86.

22. Lilley, D.M.J. (2000) *Q. Rev. Biophys.*, **33**, 109–159.

23. Zhang, D.Y.; and Winfree, E. (2009) *J. Am. Chem. Soc.*, **131**, 17303–17314.

24. Schaeffer, J.M.; Srinivas, N.; Ouldridge, T.E.; Petr, S.; Yurke, B.; Louis, A.A.; Doye, J.P.K.; and Winfree, E. (2013) **41**, 10641–10658.

25. Genot, A.J.; Zhang, D.Y.; Bath, J.; and Turber, A.J. (2011) 2177–2182.

26. Yurke, B.; Turberfield, A.J.; Mills, A.P.; Simmel, F.C.; and Neumann, J.L. (2000) *Nature*, **406**, 605–608.

27. Reif, J.H. (2003) *Nat. Comput.*, **2**, 439–461.

28. Turberfield, A.J.; Mitchell, J.C.; Yurke, B.; Mills, A.P.; Blakey, M.I.; and Simmel, F.C. (2003) *Phys. Rev. Lett.*, **90**, 4.

29. Xing, Y.; Yang, Z.; and Liu, D. (2011) *Angew. Chem. Int. Ed.*, **50**, 11934–11936.

30. Huang, F.; You, M.; Han, D.; Xiong, X.; Liang, H.; and Tan, W. (2013) *J. Am. Chem. Soc.*, **135**, 7967–7973.

31. Chen, X. (2012) *J. Am. Chem. Soc.*, **134**, 263–271.

32. Yin, Y.; and Zhao, X.S. (2011) *Acc. Chem. Res.*, **44**, 1172–1181.

33. Chen, C.; Wang, W.; Wang, Z.; Wei, F.; and Zhao, X.S. (2007) *Nucleic Acids Res.*, **35**, 2875–2884.

34. Bui, H.; Miao, V.; Garg, S.; Mokhtar, R.; Song, T.; and Reif, J. (2017) *Small*, **13**, 1–8.

35. Yang, X.; Tang, Y.; Mason, S.D.; Chen, J.; and Li, F. (2016) *ACS Nano*, **10**, 2324–2330.

36. Li, F.; Tang, Y.; Traynor, S.M.; Li, X.F.; and Le, X.C. (2016) *Anal. Chem.*, **88**, 8152–8157.

37. Fujifilm Wako Chemicals U.S.A. Corporation; Fredriksson, S.; Gullberg, M.; Jarvius, J.; Olsson, C.; Pietras, K.; Gústafsdóttir, S.M.; Östman, A.; and Landegren, U. (2014) *Nat. Biotechnol.*, **20**, 473–477.

38. Hermanson, G.T. (2013) in *Bioconjugate Techniques* Elsevier, pp. 959–987.

39. Niemeyer, C.M. (2010) *Angew. Chem. Int. Ed.*, **49**, 1200–1216.

40. El-Sagheer, A.H.; and Brown, T. (2010) *Chem. Soc. Rev.*, **39**, 1388–1405.

41. Dong, Y.; Liu, D.; and Yang, Z. (2014) *Methods*, **67**, 116–122.

42. Weisbrod, S.H.; and Marx, A. (2008) *Chem. Commun.*, 5675.

43. Xu, W.; Chan, K.M.; and Kool, E.T. (2017) *Nat. Chem.*, **9**, 1043–1055.

44. Moreira, B.G.; You, Y.; Behlke, M.A.; and Owczarzy, R. (2005) *Biochem. Biophys. Res. Commun.*, **327**, 473–484.

45. Lehnman, I.R. (1974) *Science*, **186**, 790–797.

46. Wilkinson, A.; Day, J.; and Bowater, R. (2001) *Mol. Microbiol.*, **40**, 1241–1248.

47. Song, I.H.; Shin, S.W.; Park, K.S.; Lansac, Y.; Jang, Y.H.; and Um, S.H. (2015) *Sci. Rep.*, **5**, 1–9.

48. Rossi, R.; Montecucco, A.; Ciarrocchi, G.; and Biamonti, G. (1997) *Nucleic Acids Res.*, **25**, 2106–2113.

49. Shi, K.; Bohl, T.E.; Park, J.; Zasada, A.; Malik, S.; Banerjee, S.; Tran, V.; Li, N.; Yin, Z.; Kurniawan, F.; Orellana, K.; and Aihara, H. (2018) *Nucleic Acids Res.*, **46**, 10474–10488.

50. Zhao, B.; Tong, Z.; Zhao, G.; Mu, R.; Shang, H.; and Guan, Y. (2013) *Acta Biochim. Biophys. Sin. (Shanghai).*, **46**, 727–737.

51. Rusche, J.R.; and Howard-Flanders, P. (1985) *Nucleic Acids Res.*, **13**, 1997–2008.

52. Hayashi, K.; Nakazawa, M.; Ishizaki, Y.; Hiraoka, N.; and Obayashi, A. (1986) *Nucleic Acids Res.*, **14**, 7617–7631.

53. Valeur, B.; and Berberan-Santos, M.N. (2012) in *Molecular Fluorescence: Principles and Applications - 2nd Edition*.

54. Medintz, I.; and Hildebrandt, N. (2013) in *FRET - Förster Resonance Energy Transfer: From Theory to Applications*.

55. Hötzer, B.; Medintz, I.L.; and Hildebrandt, N. (2012) *Small*, **8**, 2297–2326.

56. Giepmans, B.N.G. (2006) *Science*, **312**, 217–224.

57. Sauer, M.; Hofkens, J.; and Enderlein, J. (2011) in *Handbook of Fluorescence Spectroscopy and Imaging*.

58. Sameiro, M.; and Gonçalves, T. (2009) *Chem. Rev.*, **109**, 190–212.

59. Navarro, E.; Serrano-Heras, G.; Castaño, M.J.; and Solera, J. (2015) *Clin. Chim. Acta*, **439**, 231–250.

60. Arthanari, H.; Basu, S.; Kawano, T.L.; and Bolton, P.H. (1998) *Nucleic Acids Res.*, **26**, 3724–3728.

61. Bünzli, J.C.G. (2010) *Chem. Rev.*, **110**, 2729–2755.

62. Moore, E.G.; Samuel, A.P.S.; and Raymond, K.N. (2009) *Acc. Chem. Res.*, **42**, 542–552.

63. Algar, W.R.; Wegner, D.; Huston, A.L.; Blanco-Canosa, J.B.; Stewart, M.H.; Armstrong, A.; Dawson, P.E.; Hildebrandt, N.; and Medintz, I.L. (2012) *J. Am. Chem. Soc.*, **134**, 1876–1891.

64. Bünzli, J.-C.G. (2015) *Coord. Chem. Rev.*, **293**–**294**, 19–47.

65. Selvin, P.R. (2002) *Annu. Rev. Biophys. Biomol. Struct.*, **31**, 275–302.

66. Pu, Y.; Cai, F.; Wang, D.; Wang, J.X.; and Chen, J.F. (2018) *Ind. Eng. Chem. Res.*, **57**, 1790–1802.

67. Petryayeva, E.; Algar, W.R.; and Medintz, I.L. (2013) *Appl. Spectrosc.*, **67**, 215–252.

68. Sutherland, A.J. (2002) *Curr. Opin. Solid State Mater. Sci.*, **6**, 365–370.

69. Medintz, I.L.; Uyeda, H.T.; Goldman, E.R.; and Mattoussi, H. (2005) *Nat. Mater.*, **4**, 435–446.

70. Mitchell, G.P.; Mirkin, C.A.; and Letsinger, R.L. (1999) *J. Am. Chem. Soc.*, **121**, 8122–8123.

71. Banerjee, A.; Pons, T.; Lequeux, N.; and Dubertret, B. (2016) *Interface Focus*, **6**, 20160064.

72. Sun, D.; and Gang, O. (2013) *Langmuir*, **29**, 7038–7046.

73. Algar, W.R.; and Krull, U.J. (2006) *Langmuir*, **22**, 11346–11352.

74. Doane, T.L.; Alam, R.; and Maye, M.M. (2015) *Nanoscale*, **7**, 2883–2888.

75. Massey, M.; Medintz, I.L.I.L.I.L.; Ancona, M.G.M.G.M.G.; and Algar, W.R.R. (2017) *ACS Sensors*, **2**, 1205–1214.

76. Douglas, S.M.; Bachelet, I.; Church, G.M.; Winfree, E.; and LaBean, T.H. (2012) *Science*, **335**, 831–834.

77. Adleman, L. (1994) *Science*, **266**, 1021–1024.

78. Lipton, R. (1995) *Science*, **268**, 542–545.

79. Guarnieri, F.; Fliss, M.; and Bancroft, C. (1996) *Science*, **273**, 220–223.

80. Ogihara, M.; and Ray, A. (1999) *Algorithmica*, **25**, 239–250.

81. Qian, L.; and Winfree, E. (2011) *J. R. Soc. Interface*, **8**, 1281–1287.

82. Wang, F.; Lv, H.; Li, Q.; Li, J.; Zhang, X.; Shi, J.; Wang, L.; and Fan, C. (2020) *Nat. Commun.*, **11**, 1–8.

83. Vijayakumar, P.; and Macdonald, J. (2017) *ChemPhysChem*, **18**, 1735–1741.

84. Hemphill, J.; and Deiters, A. (2013) *J. Am. Chem. Soc.*, **135**, 10512–10518.

85. Chen, Y.; Song, Y.; Wu, F.; Liu, W.; Fu, B.; Feng, B.; and Zhou, X. (2015) *Chem. Commun.*, **51**, 6980–6983.

86. Xu, W.; Deng, R.; Wang, L.; and Li, J. (2014) *Anal. Chem.*, **86**, 7813–7818.

87. Zhang, X.; Cheng, R.; Shi, Z.; and Jin, Y. (2017) *Sensors Actuators, B Chem.*, **244**, 387–392.

88. Li, X.; Ding, T.; Sun, L.; and Mao, C. (2011) *Biosens. Bioelectron.*, **30**, 241–248.

89. Bi, S.; Ye, J.; Dong, Y.; Li, H.; and Cao, W. (2016) *Chem. Commun.*, **52**, 402–405.

90. Orbach, R.; Mostinski, L.; Wang, F.; and Willner, I. (2012) *Chem. Eur. J.*, **18**, 14689–14694.

91. Qian, L.; and Winfree, E. (2011) *Science*, **332**, 1196–1201.

92. Yao, D.; Song, T.; Zheng, B.; Xiao, S.; Huang, F.; and Liang, H. (2015) *Nanotechnology*, **26**, 425601.

93. Liu, J.; Zhang, Y.; Xie, H.; Zhao, L.; Zheng, L.; and Ye, H. (2019) *Small*, **15**, 1–17.

94. Guo, Y.; Wu, J.; and Ju, H. (2015) *Chem. Sci.*, **6**, 4318–4323.

95. Bi, S.; Yue, S.; Wu, Q.; and Ye, J. (2016) *Biosens. Bioelectron.*, **83**, 281–286.

96. Bi, S.; Chen, M.; Jia, X.; Dong, Y.; and Wang, Z. (2015) *Angew. Chem. Int. Ed.*, **54**, 8144–8148.

97. Chen, J.; Zhou, S.; and Wen, J. (2015) *Angew. Chemie*, **127**, 456–460.

98. Bi, S.; Yue, S.; Wu, Q.; and Ye, J. (2016) *Chem. Commun.*, **52**, 5455–5458.

99. Yin, P.; Choi, H.M.T.; Calvert, C.R.; and Pierce, N.A. (2008) *Nature*, **451**, 318–322.

100. Peracchi, A. (2005) *ChemBioChem*, **6**, 1316–1322.

101. Hollenstein, M. (2015) *Molecules*, **20**, 20777–20804.

102. Kumar, S.; Jain, S.; Dilbaghi, N.; Ahluwalia, A.S.; Hassan, A.A.; and Kim, K.H. (2019) *Trends Biochem. Sci.*, **44**, 190–213.

103. Orbach, R.; Willner, B.; and Willner, I. (2015) *Chem. Commun.*, **51**, 4144–4160.

104. Breaker, R.R.; and Joyce, G.F. (1994) *Chem. Biol.*, **1**, 223–229.

105. Chandra, M.; Sachdeva, A.; and Silverman, S.K. (2009) *Nat. Chem. Biol.*, **5**, 718–720.

106. Lan, T.; and Lu, Y. (2012) in *Interplay between Metal Ions and Nucleic Acids* (eds A. Sigel, H. Sigel, R.K.O. Sigel). Springer Netherlands, Dordrecht, pp. 217–248.

107. Stojanovic, M.N.; Mitchell, T.E.; and Stefanovic, D. (2002) *J. Am. Chem. Soc.*, **124**, 3555–3561.

108. Stojanović, M.N.; and Stefanović, D. (2003) *J. Am. Chem. Soc.*, **125**, 6673–6676.

109. Lederman, H.; Macdonald, J.; Stefanovic, D.; and Stojanovic, M.N. (2006) *Biochemistry*, **45**, 1194–1199.

110. Brown, C.W.; Lakin, M.R.; Horwitz, E.K.; Fanning, M.L.; West, H.E.; Stefanovic, D.; and Graves, S.W. (2014) *Angew. Chem. Int. Ed.*, **53**, 7183–7187.

111. Elbaz, J.; Wang, F.; Remacle, F.; and Willner, I. (2012) *Nano Lett.*, **12**, 6049–6054.

112. Elbaz, J.; Lioubashevski, O.; Wang, F.; Remacle, F.; Levine, R.D.; and Willner, I. (2010) *Nat. Nanotechnol.*, **5**, 417–422.

113. Yang, T.; Wang, N.; Li, N.; Huang, C.; Wang, J.; Zou, H.; Liu, Z.; and Peng, Z. (2018) *Sci. China Chem.*, **61**, 490–496.

114. Kahan-Hanum, M.; Douek, Y.; Adar, R.; and Shapiro, E. (2013) *Sci. Rep.*, **3**, 1–6.

115. Orbach, R.; Wang, F.; Lioubashevski, O.; Levine, R.D.; Remacle, F.; and Willner, I. (2014) *Chem. Sci.*, **5**, 3381.

116. Orbach, R.; Remacle, F.; Levine, R.D.; and Willner, I. (2014) *Chem. Sci.*, **5**, 1074.

117. Xu, Y. (2011) *Chem. Soc. Rev.*, **40**, 2719.

118. Monchaud, D.; and Teulade-Fichou, M.P. (2008) *Org. Biomol. Chem.*, **6**, 627–636.

119. Krainer, F.W.; and Glieder, A. (2015) *Appl. Microbiol. Biotechnol.*, **99**, 1611–1625.

120. Tao, L.; Shaojun, D.; and Erkang, W. (2009) *Chem. Asian J.*, **4**, 918–922.

121. Golub, E.; Freeman, R.; Niazov, A.; and Willner, I. (2011) *Analyst*, **136**, 4397–4401.

122. Chen, J.; Pan, J.; and Chen, S. (2018) *Chem. Sci.*, **9**, 300–306.

123. Gao, W.; Zhang, L.; Zhang, Y.M.; Liang, R.P.; and Qiu, J.D. (2014) *J. Phys. Chem. C*, **118**, 14410–14417.

124. Li, T.; Ackermann, D.; Hall, A.M.; and Famulok, M. (2012) *J. Am. Chem. Soc.*, **134**, 3508–3516.

125. Li, T.; Wang, E.; and Dong, S. (2009) *J. Am. Chem. Soc.*, **131**, 15082–15083.

126. Li, D.; Cheng, W.; Li, Y.; Xu, Y.; Li, X.; Yin, Y.; Ju, H.; and Ding, S. (2016) *Anal. Chem.*, **88**, 7500–7506.

127. Li, T.; Lohmann, F.; and Famulok, M. (2014) *Nat. Commun.*, **5**, 4940.

128. Zhu, J.; Li, T.; Zhang, L.; Dong, S.; and Wang, E. (2011) *Biomaterials*, **32**, 7318–7324.

129. Pejler, G.; Rönnberg, E.; Waern, I.; and Wernersson, S. (2010) *Blood*, **115**, 4981–4990.

130. Hanahan, D.; and Weinberg, R.A. (2011) *Cell*, **144**, 646–674.

131. Sanman, L.E.; and Bogyo, M. (2014) *Annu. Rev. Biochem.*, **83**, 249–273.

132. Mann, K.G.; Brummel, K.; and Butenas, S. (2003) *J. Thromb. Haemost.*, **1**, 1504–1514.

133. Reddel, C.J.; Tan, C.W.; and Chen, V.M. (2019) *Cancers (Basel).*, **11**, 1–20.

134. Davalos, D.; Baeten, K.M.; Whitney, M.A.; Mullins, E.S.; Friedman, B.; Olson, E.S.; Ryu, J.K.; Smirnoff, D.S.; Petersen, M.A.; Bedard, C.; Degen, J.L.; Tsien, R.Y.; and Akassoglou, K. (2014) *Ann. Neurol.*, **75**, 303–308.

135. Hermanson, G.T. (2013) *Bioconjugate Tech.*, 229–258.

136. Deng, B.; Lin, Y.; Wang, C.; Li, F.; Wang, Z.; Zhang, H.; Li, X.; and Le, X.C. (2014) *Anal. Chim. Acta*, **837**, 1–15.

137. Tasset, D.M.; Kubik, M.F.; and Steiner, W. (1997) 688–698.

138. Krauss, I.R.; Pica, A.; Merlino, A.; Mazzarella, L.; and Sica, F. (2013) *Acta Crystallogr. Sect. D Biol. Crystallogr.*, **69**, 2403–2411.

139. Müller, J.; Freitag, D.; Mayer, G.; and Pötzsch, B. (2008) *J. Thromb. Haemost.*, **6**, 2105–2112.

140. Lin, P.H.; Chen, R.H.; Lee, C.H.; Chang, Y.; Chen, C.S.; and Chen, W.Y. (2011) *Colloids Surfaces B Biointerfaces*, **88**, 552–558.

141. Massey, M.; Ancona, M.G.; Medintz, I.L.; and Algar, W.R. (2015) *ACS Photonics*, **2**, 639–652.

142. Massey, M.; Ancona, M.G.; Medintz, I.L.; and Algar, W.R. (2015) *Anal. Chem.*, **87**, 11923–11931.

143. Markham, N.R.; and Zuker, M. (2005) *Nucleic Acids Res.*, **33**, 577–581.

144. Bock, L.C.; Griffin, L.C.; Latham, J.A.; Vermaas, E.H.; and Toole, J.J. (1992) *Nature*, **355**, 564–566.

145. Trapaidze, A.; Hérault, J.; Herbert, J.; Bancaud, A.; and Gué, A. (2016) *Biosens. Bioelectron.*, **78**, 58–66.

146. Segers, K.; Dahlback, B.; Bock, P.E.; Tans, G.; Rosing, J.; and Nicolaes, G.A.F. (2007) *J. Biol. Chem.*, **282**, 33915–33924.

147. Zhou, G.; Huang, X.; and Qu, Y. (2010) *Biochem. Eng. J.*, **52**, 117–122.

148. Padmanabhan, K.; and Tulinsky, A. (1996) *Acta Crystallogr. Sect. D Biol. Crystallogr.*, **52**, 272–282.

149. Li, J.J.; Fang, X.; and Tan, W. (2002) *Biochem. Biophys. Res. Commun.*, **292**, 31–40.

150. Markham, N.R.; Zuker, L.S.; and Zuker, M. .

151. Pagano, B.; Martino, L.; Randazzo, A.; and Giancola, C. (2008) *Biophys. J.*, **94**, 562–569.

152. Li, B.; Wei, H.; and Dong, S. (2007) *Chem. Commun.*, 73–75.

153. Wu, M.; Petryayeva, E.; and Algar, W.R. (2014) *Anal. Chem.*, **86**, 11181–11188.

154. Sui, N.; Wang, L.; Xie, F.; Liu, F.; Xiao, H.; Liu, M.; and Yu, W.W. (2016) *Microchim. Acta*, **183**, 1563–1570.

155. Nutiu, R.; and Li, Y. (2003) *J. Am. Chem. Soc.*, **125**, 4771–4778.

156. Levy, M.; Cater, S.F.; and Ellington, A.D. (2005) *ChemBioChem*, **6**, 2163–2166.

157. Li, N.; and Ho, C.-M. (2008) *J. Am. Chem. Soc.*, **130**, 2380–2381.

158. Wang, W.; Chen, C.; Qian, M.; and Zhao, X.S. (2008) *Anal. Biochem.*, **373**, 213–219.

159. Bassam, B.J.; and Gresshoff, P.M. (2007) *Nat. Protoc.*, **2**, 2649–2654.

160. Kosuri, S.; and Church, G.M. (2014) *Nat. Methods*, **11**, 499–507.

161. Wang, S.; Gaylord, B.S.; and Bazan, G.C. (2004) *J. Am. Chem. Soc.*, **126**, 5446–5451.

162. Li, B.; Ellington, A.D.; and Chen, X. (2011) *Nucleic Acids Res.*, **39**, e110–e110.

163. Chatterjee, G.; Dalchau, N.; Muscat, R.A.; Phillips, A.; and Seelig, G. (2017) *Nat. Nanotechnol.*, **12**, 920–927.

164. Bui, H.; Shah, S.; Mokhtar, R.; Song, T.; Garg, S.; and Reif, J. (2018) *ACS Nano*, **12**, 1146–1155.

165. Liu, L.; Rong, Q.; Ke, G.; Zhang, M.; Li, J.; Li, Y.; Liu, Y.; Chen, M.; and Zhang, X.B. (2019) *Anal. Chem.*, **91**, 3676–3680.

166. Nasef, H.; Ozalp, V.C.; Beni, V.; and O'Sullivan, C.K. (2010) *Anal. Biochem.*, **406**, 34–40.

167. Chen, C.; Wang, W.; Ge, J.; and Zhao, X.S. (2009) *Nucleic Acids Res.*, **37**, 3756–3765.

168. Li, J.J.; and Russ Algar, W. (2016) *Analyst*, **141**, 3636–3647.

169. Han, H.; Zylstra, J.; and Maye, M.M. (2011) *Chem. Mater.*, **23**, 4975–4981.

170. Elghanian, R.; Storhoff, J.J.; Mucic, R.C.; Letsinger, R.L.; and Mirkin, C.A. (1997) *Science*, **277**, 1078–1081.

171. Hurst, S.J.; Lytton-Jean, A.K.R.; and Mirkin, C.A. (2006) *Anal. Chem.*, **78**, 8313–8318.

172. Green, S.J.; Lubrich, D.; and Turberfield, A.J. (2006) *Biophys. J.*, **91**, 2966–2975.

173. Geng, Y.; Peveler, W.J.; and Rotello, V.M. (2019) *Angew. Chem. Int. Ed.*, **58**, 5190–5200.

174. Bigdeli, A.; Ghasemi, F.; Golmohammadi, H.; Abbasi-Moayed, S.; Nejad, M.A.F.; Fahimi-Kashani, N.; Jafarinejad, S.; Shahrajabian, M.; and Hormozi-Nezhad, M.R. (2017) *Nanoscale*, **9**, 16546–16563.

175. Xu, Q.; Zhang, Y.; Tang, B.; and Zhang, C.Y. (2016) *Anal. Chem.*, **88**, 2051–2058.

176. Chang, N.; Lu, Y.; Mao, J.; Yang, J.; Li, M.; Zhang, S.; and Liu, Y. (2016) *Analyst*, **141**, 2046–2052.

177. Liu, J.; Li, G.; Yang, X.; Wang, K.; Li, L.; Liu, W.; Shi, X.; and Guo, Y. (2015) *Anal. Chem.*, **87**, 876–883.

178. Jiao, Z.; Zhang, P.; Chen, H.; Li, C.; Chen, L.; Fan, H.; and Cheng, F. (2019) *Sensors Actuators, B Chem.*, **295**, 110–116.

179. Abbasi-Moayed, S.; Golmohammadi, H.; Bigdeli, A.; and Hormozi-Nezhad, M.R. (2018) *Analyst*, **143**, 3415–3424.

180. Ghasemi, F.; Hormozi-Nezhad, M.R.; and Mahmoudi, M. (2016) *Anal. Chim. Acta*, **917**, 85–92.

181. López-Otín, C.; and Bond, J.S. (2008) *J. Biol. Chem.*, **283**, 30433–30437.

182. Chakraborti, S.; Chakraborti, T.; and Dhalla, N.S. (2017) in *Proteases in Human Diseases*.

183. Heutinck, K.M.; ten Berge, I.J.M.; Hack, C.E.; Hamann, J.; and Rowshani, A.T. (2010) *Mol. Immunol.*, **47**, 1943–1955.

184. Cao, Y.; Yu, J.; Bo, B.; Shu, Y.; and Li, G. (2013) *Biosens. Bioelectron.*, **45**, 1–5.

185. Chen, L.; Fu, X.; and Li, J. (2013) *Nanoscale*, **5**, 5905–5911.

186. Esseghaier, C.; Ng, A.; and Zourob, M. (2013) *Biosens. Bioelectron.*, **41**, 335–341.

187. Ding, X.; and Yang, K.L. (2015) *Analyst*, **140**, 340–345.

188. Hu, J.; Liu, F.; and Ju, H. (2015) *Anal. Chem.*, **87**, 4409–4414.

189. Wang, Y.; Shen, P.; Li, C.; Wang, Y.; and Liu, Z. (2012) *Anal. Chem.*, **84**, 1466–1473.

190. Zauner, T.; Berger-Hoffmann, R.; Müller, K.; Hoffmann, R.; and Zuchner, T. (2011) *Anal. Chem.*, **83**, 7356–7363.

191. Zhu, S.; Liu, Z.; Hu, L.; Yuan, Y.; and Xu, G. (2012) *Chem. Eur. J.*, **18**, 16556–16561.

192. Sapsford, K.E.; Granek, J.; Deschamps, J.R.; Boeneman, K.; Blanco-Canosa, J.B.; Dawson, P.E.; Susumu, K.; Stewart, M.H.; and Medintz, I.L. (2011) *ACS Nano*, **5**, 2687–2699.

193. Rees, K.; Tran, M. V.; Massey, M.; Kim, H.; Krause, K.D.; and Algar, W.R. (2020) *Bioconjug. Chem.*, **31**, 861–874.

194. Wu, M.; and Algar, W.R. (2015) *ACS Appl. Mater. Interfaces*, **7**, 2535–2545.

195. Algar, W.R.; Jeen, T.; Massey, M.; Peveler, W.J.; and Asselin, J. (2019) *Langmuir*, **35**, 7067–7091.

196. Di Cera, E. (2009) *IUBMB Life*, **61**, 510–515.

197. Jeen, T.; and Algar, W.R. (2018) *Bioconjug. Chem.*, **29**, 3783–3792.

198. Petryayeva, E.; Jeen, T.; and Algar, W.R. (2017) *ACS Appl. Mater. Interfaces*, **9**, 30359–30372.

199. Lee, C.J.; and Ansell, J.E. (2011) *Br. J. Clin. Pharmacol.*, **72**, 581–592.

Appendices

Appendix A Oligonucleotide Thermodynamic Calculations

Table A1 Sequences of oligonucleotides for design optimization via thermodynamic calculations. The position of the Uni-link internal amine linker is represented by the 'L' in the template sequences.

Sequence #	Template	Aptamer
Experimental	GCCAACCACACCAACCTLAAGTGGTTGGC	GAGGTTGGTGTGGTTGG
1	GCCAACCACACCATTGALAAGTGGTTGGC	GAGGTTGGTGTGGTTGG
2	GCCAACCACACACCLAGGTTGGC	GAGGTTGGTGTGGTTGG
3	GCCAACCACACAATTGALAGGTTGGC	GAGGTTGGTGTGGTTGG
4	GCCAACCACACAATTGALAAAAGGTTGGC	GAGGTTGGTGTGGTTGG
5	TGCCAACCACACACCLAGTTGGCA	GAGGTTGGTGTGGTTGG
6	GCCAACCACACCTTTGALAAATGGTTGGC	GAGGTTGGTGTGGTTGG
7	TTAATTAACCAATTAALTTAATTAA	GGTTGGTGTGGTTGGTTAATTAA
8	TTCATTAACCAATTAALTTAATGAA	GGTTGGTGTGGTTGGTTAATGAA
9	CTCATTAACCAATTAALTTAATGAG	GGTTGGTGTGGTTGGTTAATGAG
10	CTCCTTAACCAATTAALTTAAGGAG	GGTTGGTGTGGTTGGTTAAGGAG
11	GCCAACCACACAATTGALAAAAAAAAAAGGTTGGC	GAGGTTGGTGTGGTTGG
12	CTCCTCAACCAATTAALTTGAGGAG	GGTTGGTGTGGTTGGTTGAGGAG
13	GCCAACCACACCATTGALATGGTTGGC	GAGGTTGGTGTGGTTGG
14	GCCAACCACACACCLGGTTGGC	GAGGTTGGTGTGGTTGG
15	GCCAACCACACCATTGALAAATGGTTGGC	GAGGTTGGTGTGGTTGG
16	TTAATTAACCAATTAALTAATTAA	GGTTGGTGTGGTTGGTTAATTAA
17	TTGCCAACCACACACCLATTGGCAA	GAGGTTGGTGTGGTTGG
18	GCCAACCACACCTTTGALAAAAGGTTGGC	GAGGTTGGTGTGGTTGG
19	GCCAACCACACCTTGALATGGTTGGC	GGTTGGTGTGGTTGGC
20	GCCAACCACACCCLGGTTGGC	GAGGTTGGTGTGGTTGG
21	GGCCAACCACACCTTAALGGTTGGCC	GGTTGGTGTGGTTGGC
22	GGCCAACCACACCTTGALAGGTTGGCC	GGTTGGTGTGGTTGGC

Table A2 Parameters for thermodynamic survey of template designs

Sequence #	Hairpin bp	Hairpin GC:AT ratio	Hairpin ΔG (kcal/mol)	Duplex bp	Duplex GC:AT Ratio	Duplex ΔG (kcal/mol)	Hairpin loop length	ΔΔG (kcal/mol)	System Tm (°C)
Experimental	9	2	-10.1	16	1.28	-21.6	11	-11.5	31.5
1	9	2	-10.2	12	1.4	-16.5	7	-6.3	1.5
2	7	2.5	-7.2	10	1.5	-14.5	5	-7.3	12.5
3	7	2.5	-7	10	1.5	-14.5	7	-7.5	8
4	7	2.5	-6.8	10	1.5	-14.5	10	-7.7	14.5
5	7	1.33	-6.7	10	1.5	-14.5	5	-7.8	13
6	8	1.67	-8.1	11	1.75	-16.1	9	-8	15
7	8	0	-2.3	12	0.2	-10.4	5	-8.1	16
8	8	0.14	-3.5	12	0.33	-11.6	5	-8.1	19
9	8	0.33	-3.9	12	0.5	-12	5	-8.1	19.5
10	8	0.6	-4.7	12	0.71	-12.8	5	-8.1	20.5
11	7	2.5	-6.3	10	1.5	-14.5	17	-8.2	15.5
12	8	1	-5.8	12	1	-14	5	-8.2	21.5
13	8	1.67	-8.2	12	1.4	-16.5	5	-8.3	21.5
14	7	2.5	-6.1	10	1.5	-14.5	4	-8.4	19.5
15	8	1.67	-8.1	12	1.4	-16.5	8	-8.4	22
16	7	0	-1.8	12	0.2	-10.4	5	-8.6	20.5
17	7	0.75	-5.8	10	1.5	-14.5	5	-8.7	21.5
18	7	2.5	-6.8	11	1.75	-16.1	9	-9.3	22.5
19	8	1.67	-8.3	12	2	-17.7	6	-9.4	25.5
20	7	2.5	-6.1	10	1.5	-15.8	3	-9.7	29
21	8	3	-8	12	2	-18.3	5	-10.3	31.5
22	8	3	-7.8	12	2	-18.3	6	-10.5	24.5

Appendix B Additional Characterization Data

B.1 ^{1}H NMR Spectra

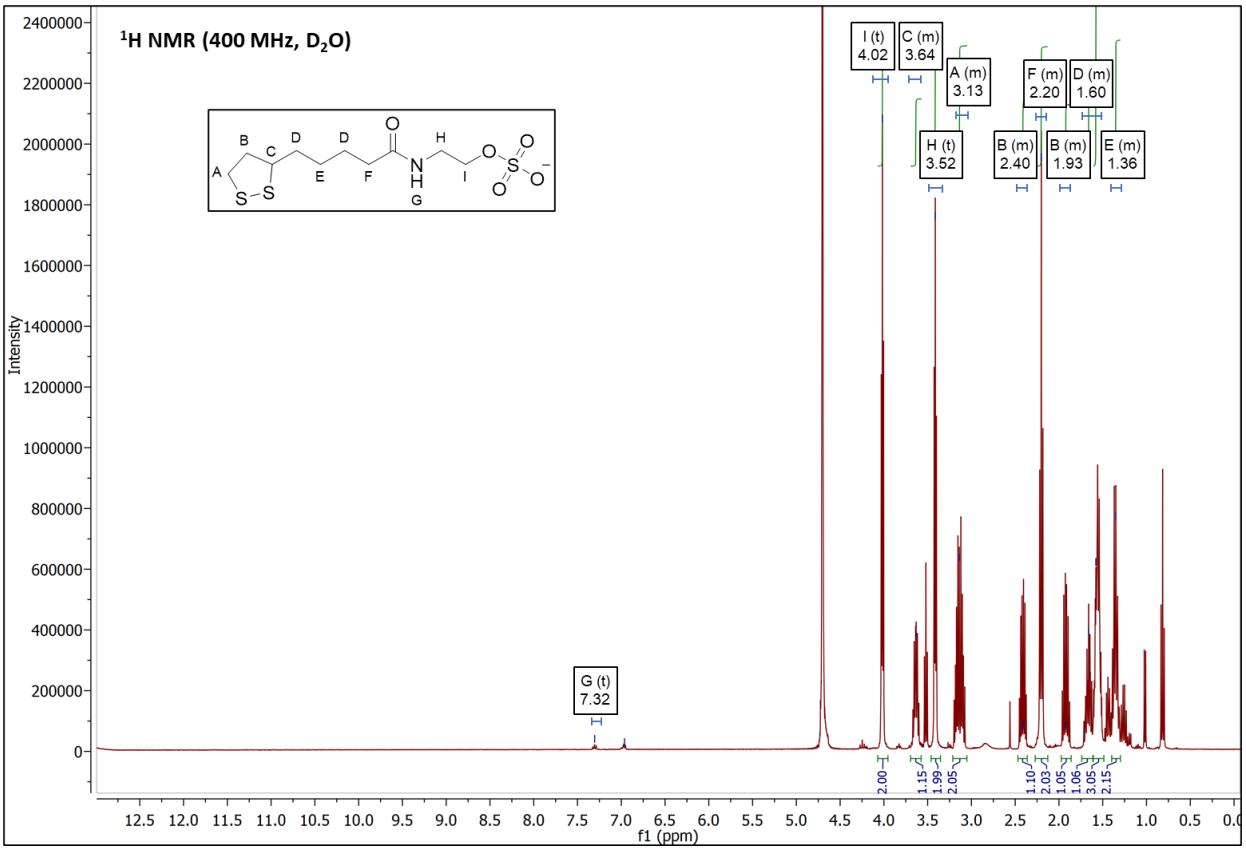

Figure B1 ^{1}H NMR spectrum of SO_4-LA

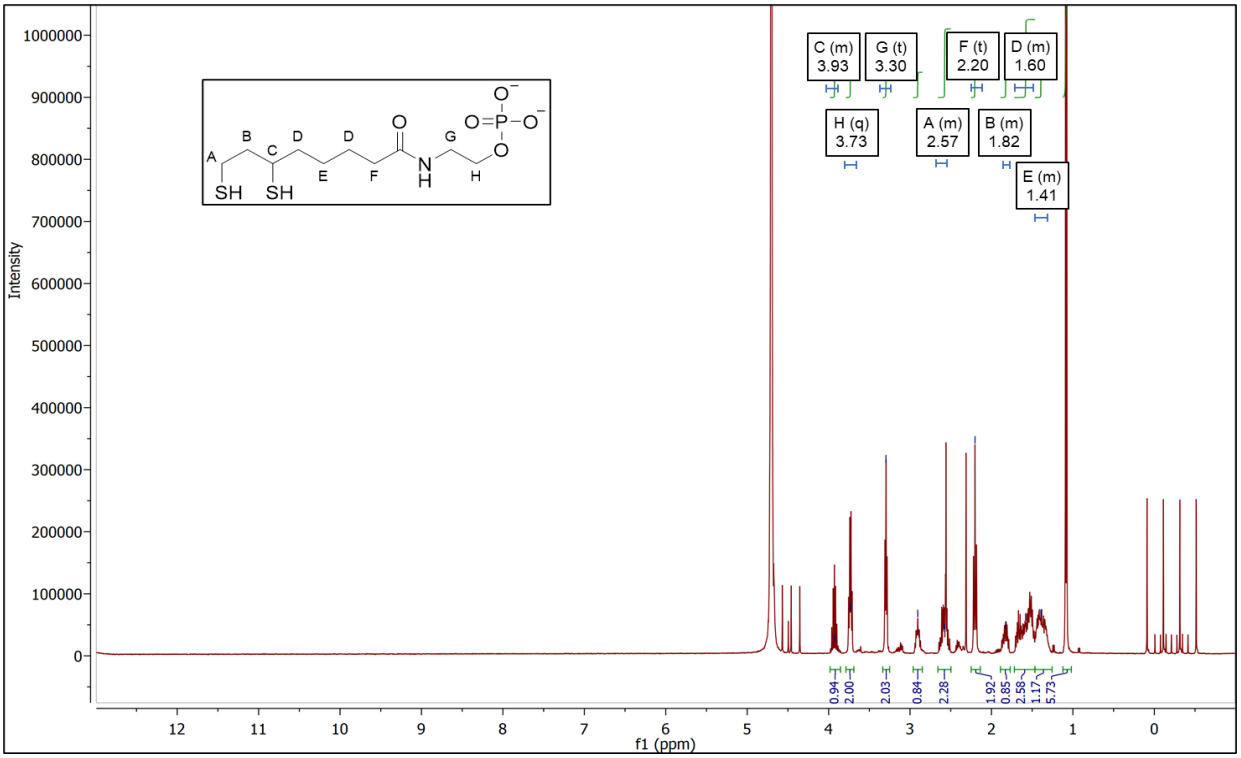

Figure B2 ^{1}H NMR spectrum of PO_4-DHLA

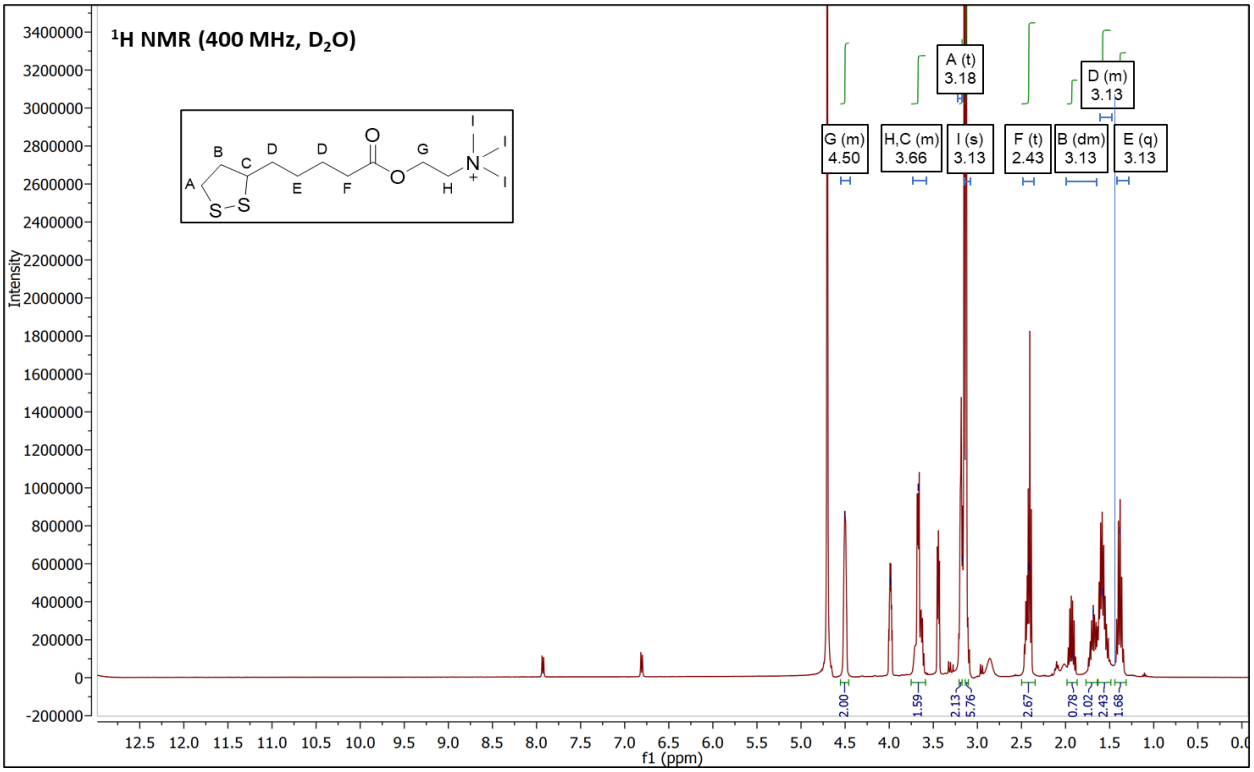

Figure B3 ^{1}H NMR spectrum of Me_4N-LA, with impurities present: choline chloride (3.99m, 3.44dd, 3.15s) and DMAP (7.95d, 6.61d, 3.18s).

B.2 ^{13}C NMR Spectra

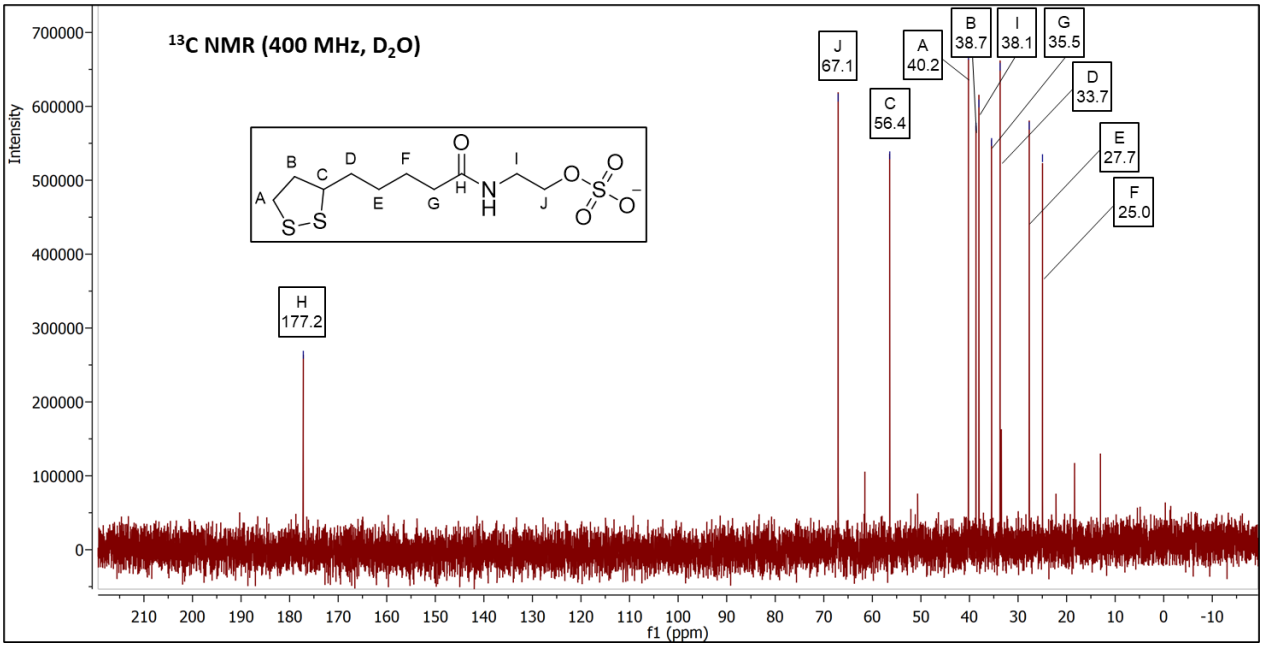

Figure B4 ^{13}C NMR spectrum of SO_4-LA

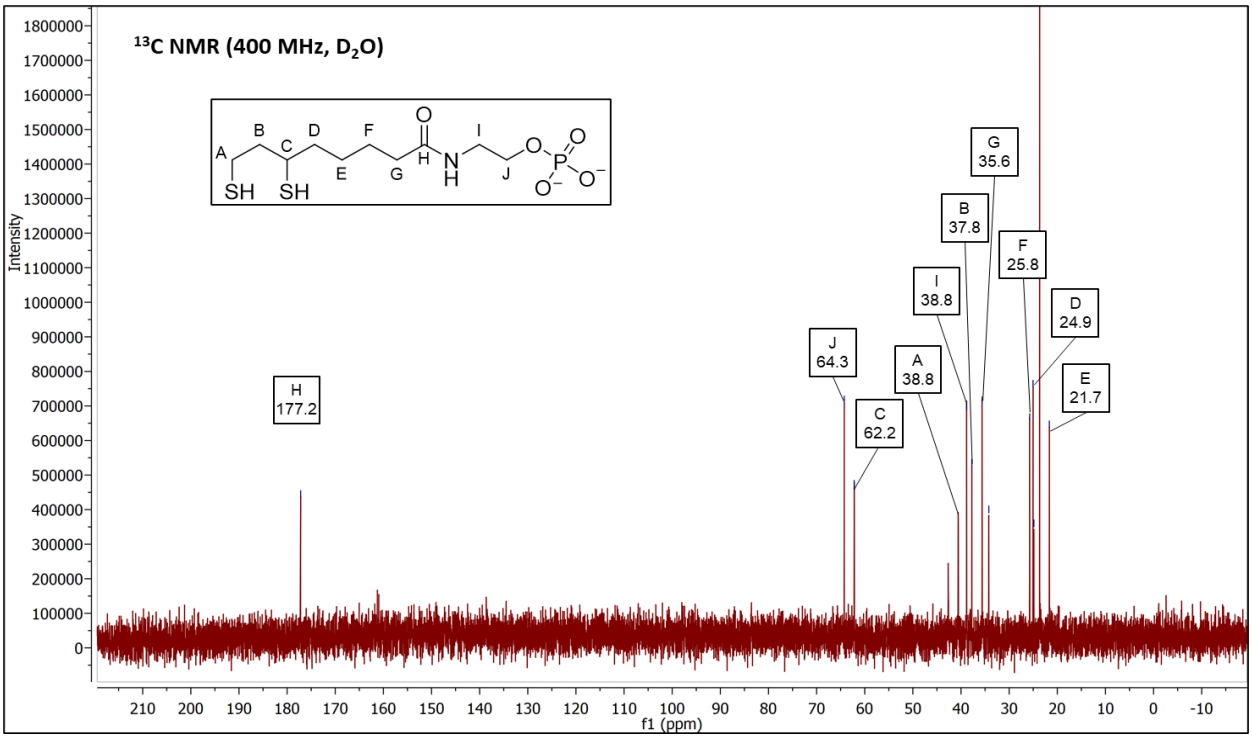

Figure B5 ^{13}C NMR spectrum of PO_4-LA

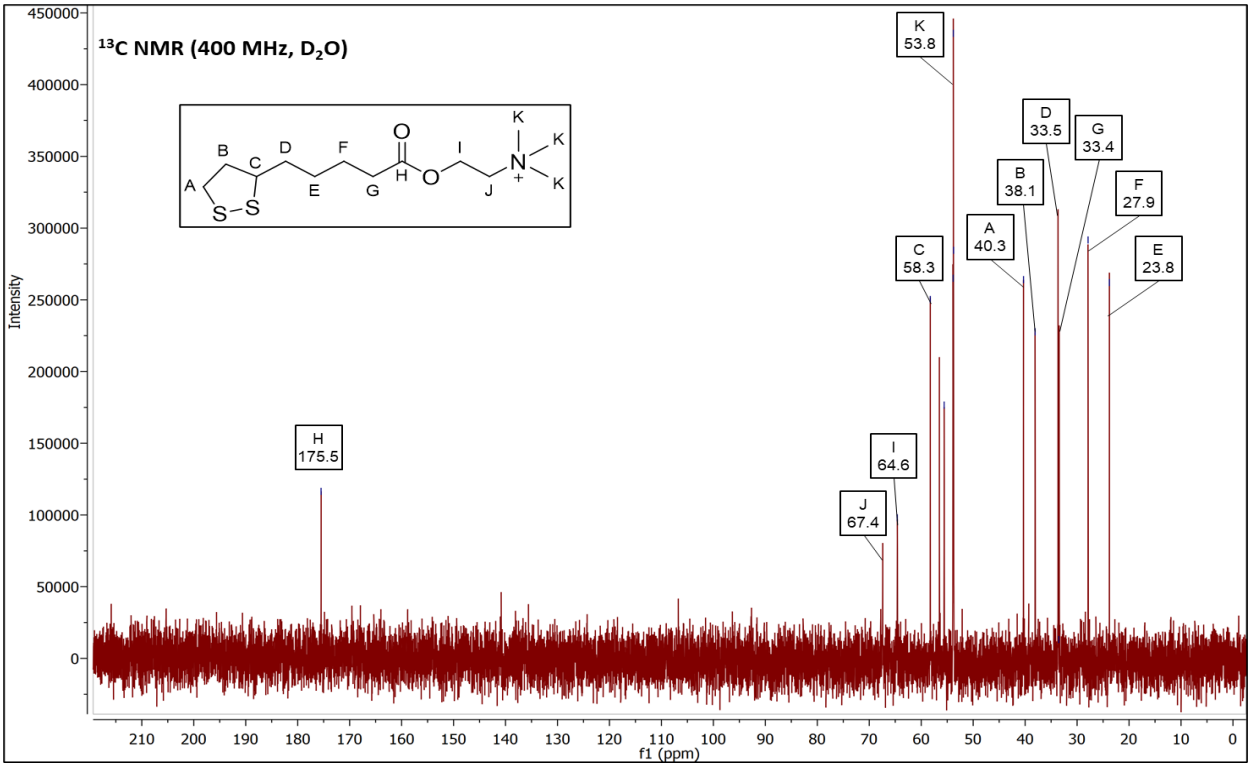

Figure B6 ^{13}C NMR spectrum of Me_4N-LA

B.3 FTIR Spectra of Neat Ligands

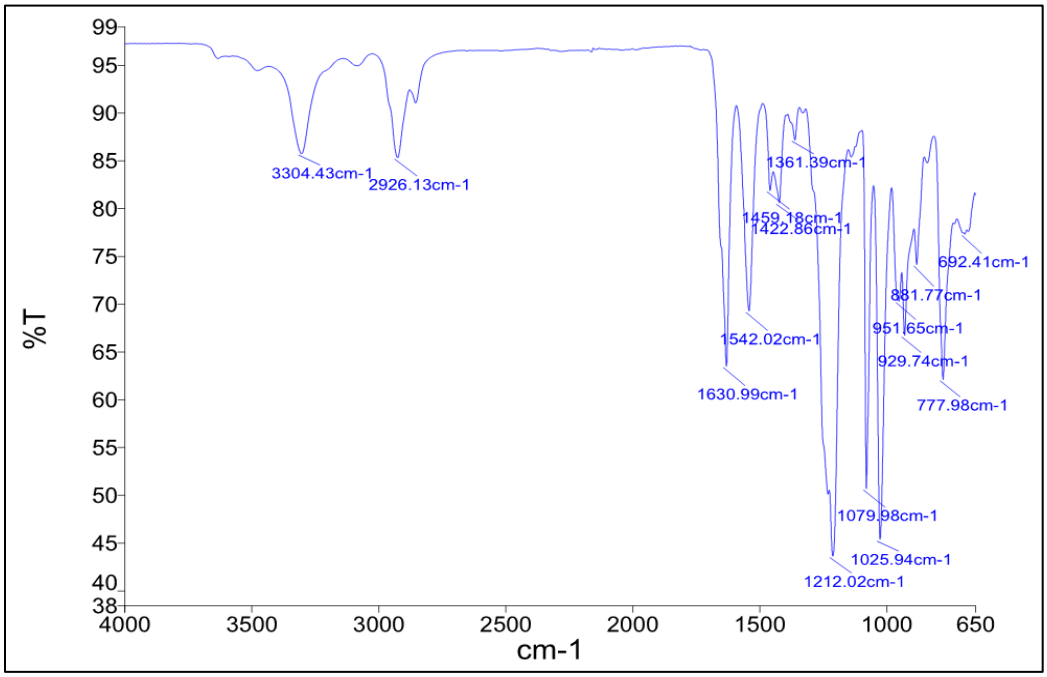

Figure B7 FTIR spectrum of SO_4-LA

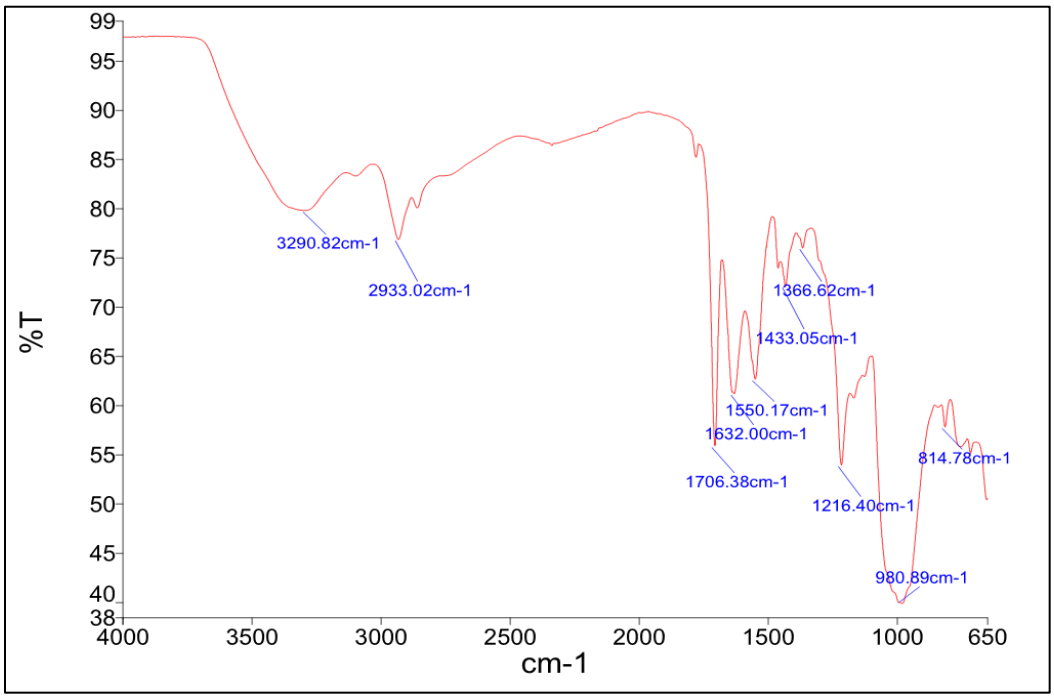

Figure B8 FTIR spectrum of PO_4-LA

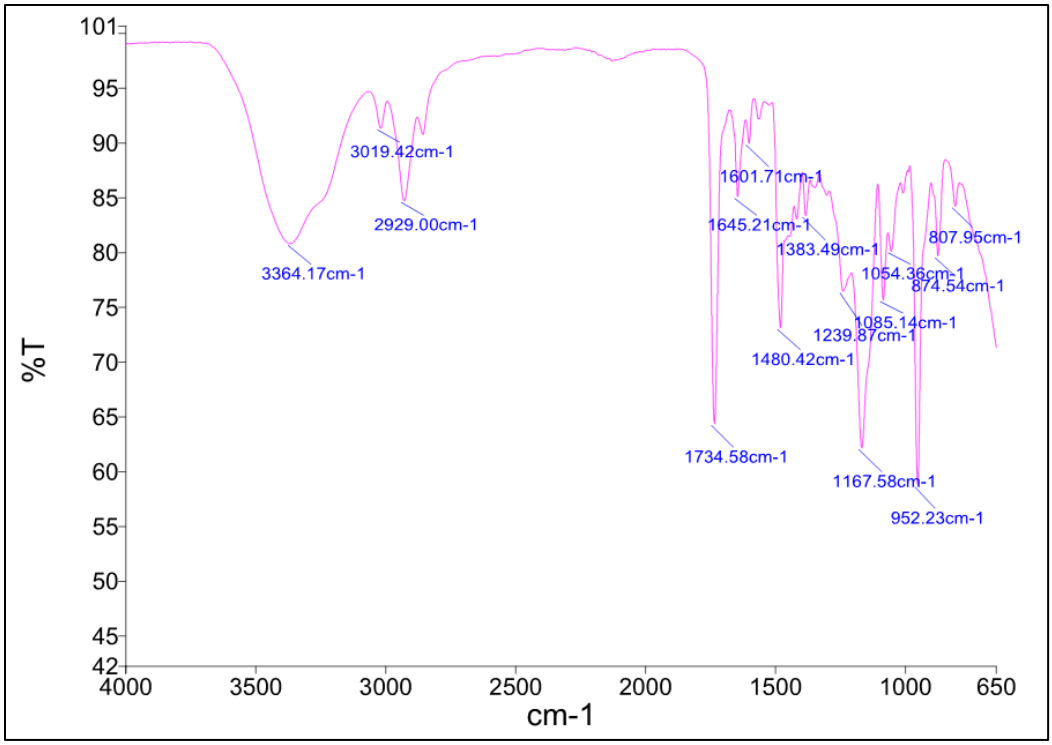

Figure B9 FTIR spectrum of Me_4N-LA

B.4 FTIR Spectra of QD-Ligand Conjugates

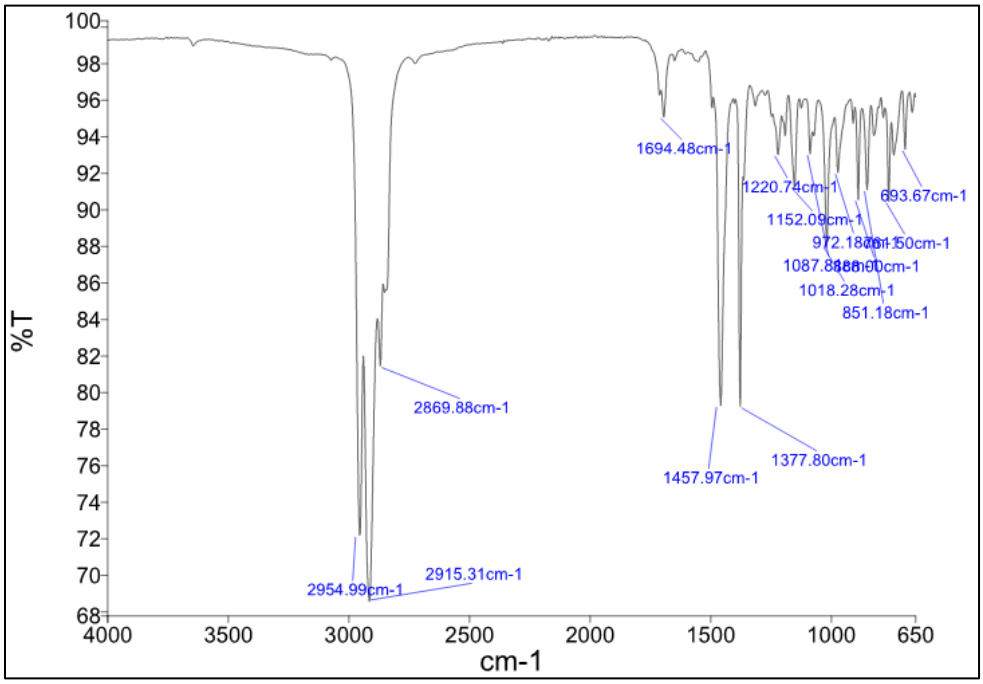

Figure B10 FTIR spectrum of alkyl ligand coated-QDs

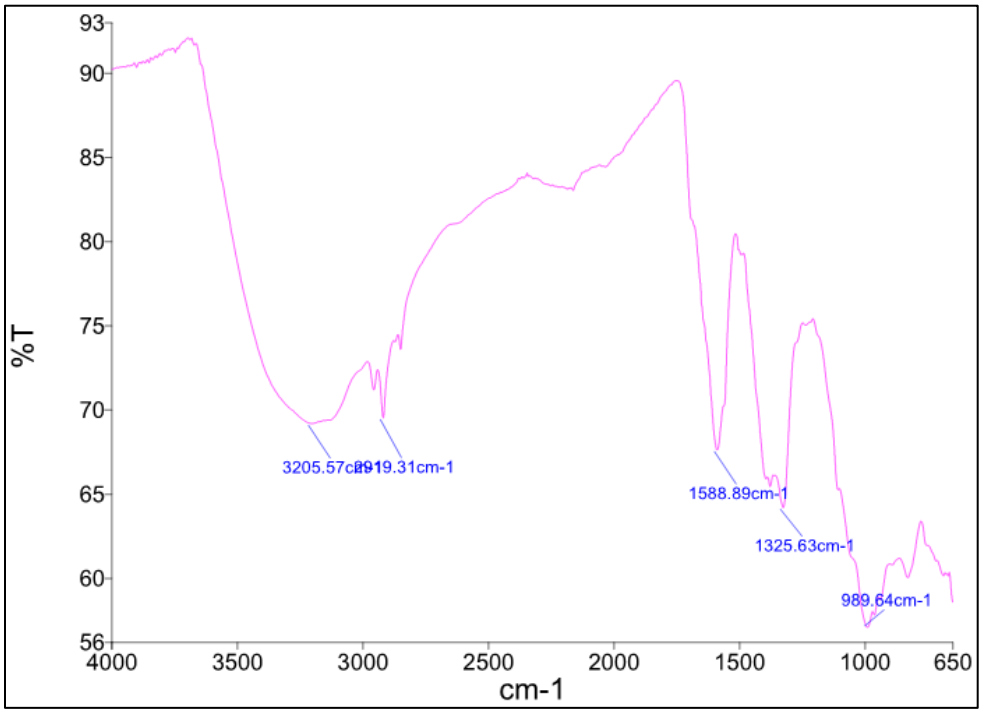

Figure B11 FTIR spectrum of His-QDs

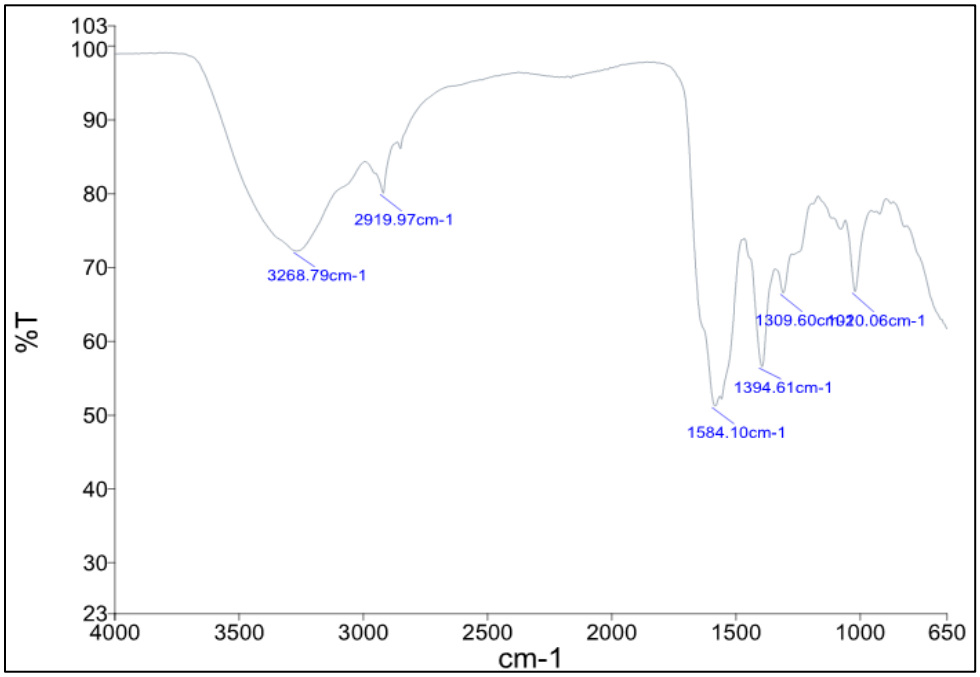

Figure B12 FTIR spectrum of GSH-QDs

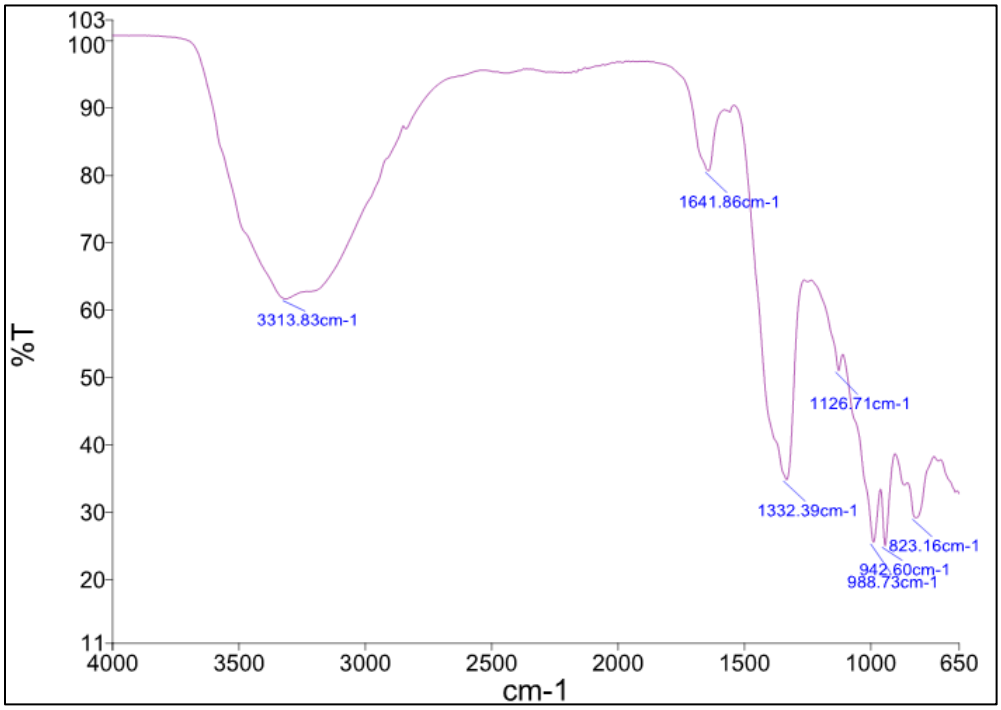

Figure B13 FTIR spectrum of DHLA-QDs

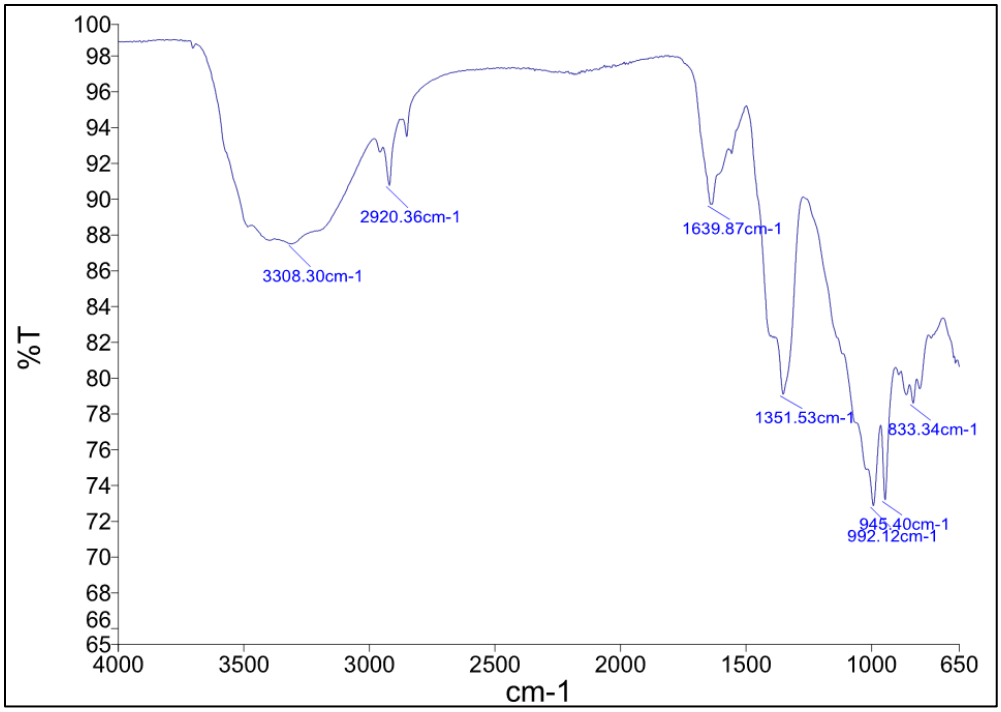

Figure B14 FTIR spectrum of SO_4-DHLA-QDs

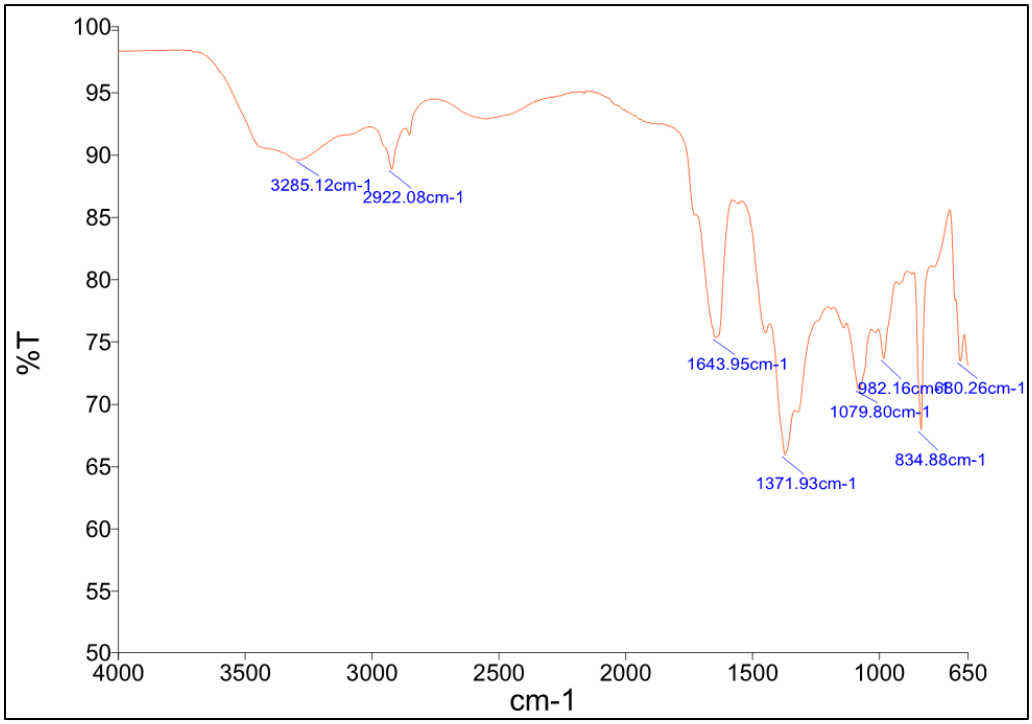

Figure B15 FTIR spectrum of PO_4-DHLA-QDs

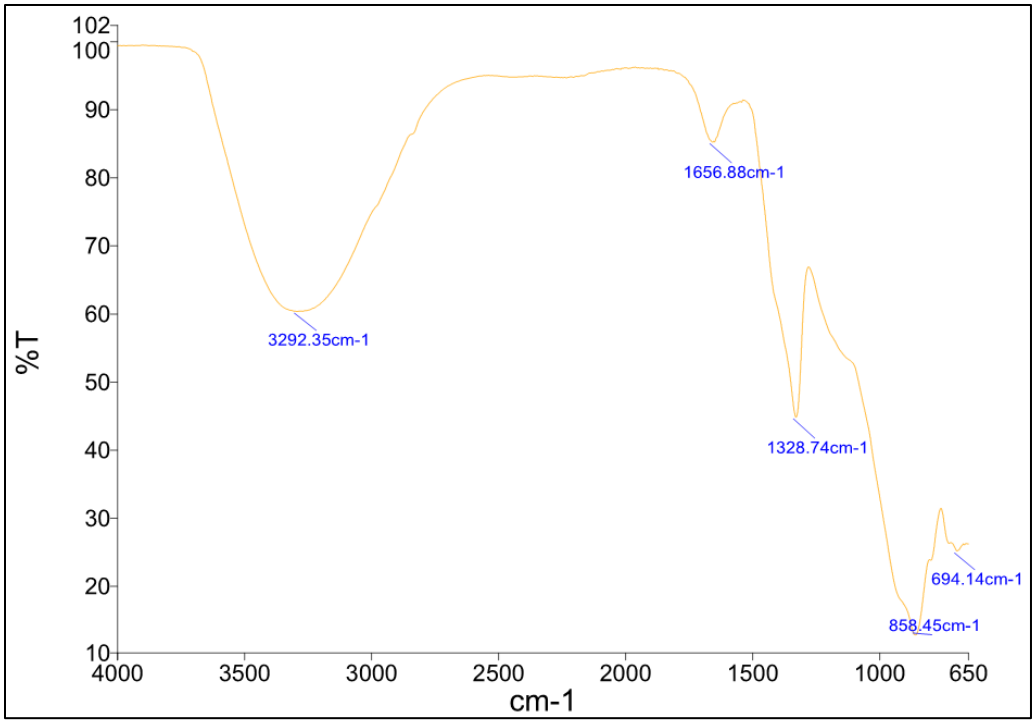

Figure B16 FTIR spectrum of nominal Me_4N-DHLA-QDs

B.5 ESI-MS Spectra

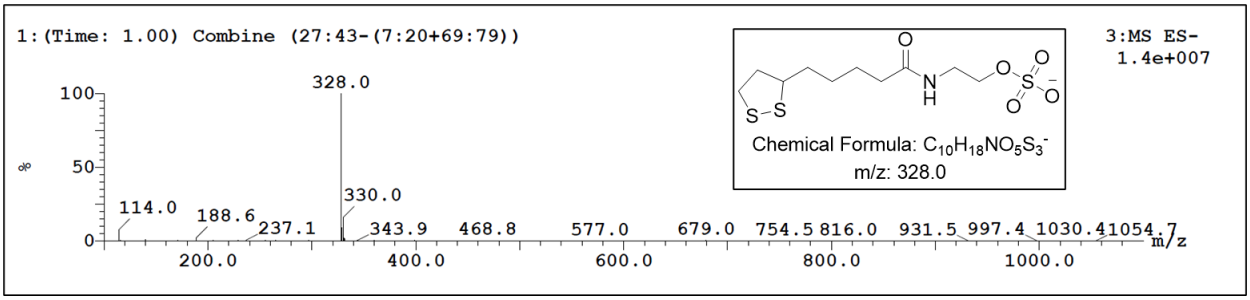

Figure B17 ESI-MS (-) spectrum for SO_4-LA

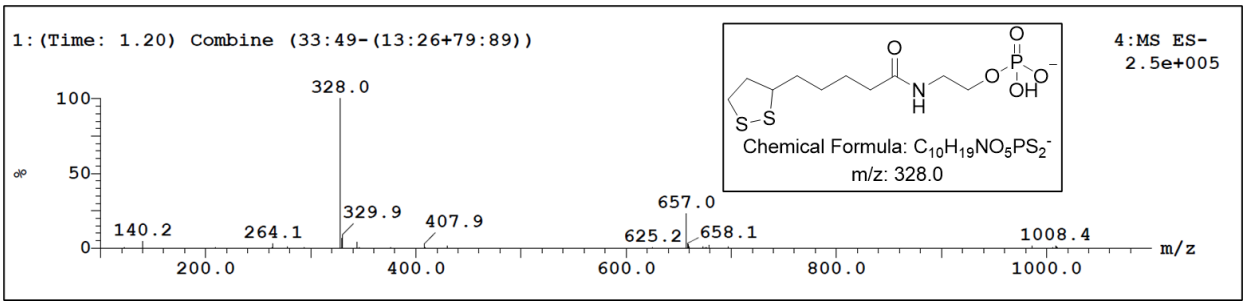

Figure B18 ESI-MS (-) spectrum for PO_4-LA (Note: peak at 657.0 m/z is the dimerized product species)

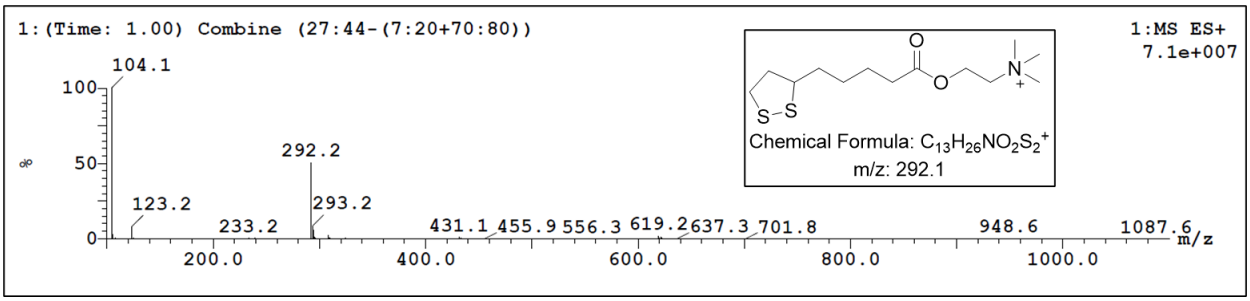

Figure B19 ESI-MS (+) spectrum for Me_4N-LA (Note: peak at 104.1 m/z is the choline chloride impurity)

B.6 Enzyme Assay Progress Curves

Each column contains one of two duplicate measurements. Measurements were made on separate days with samples from the same ligand functionalized QD stocks but using freshly prepared enzyme stocks and QD-peptide conjugates.

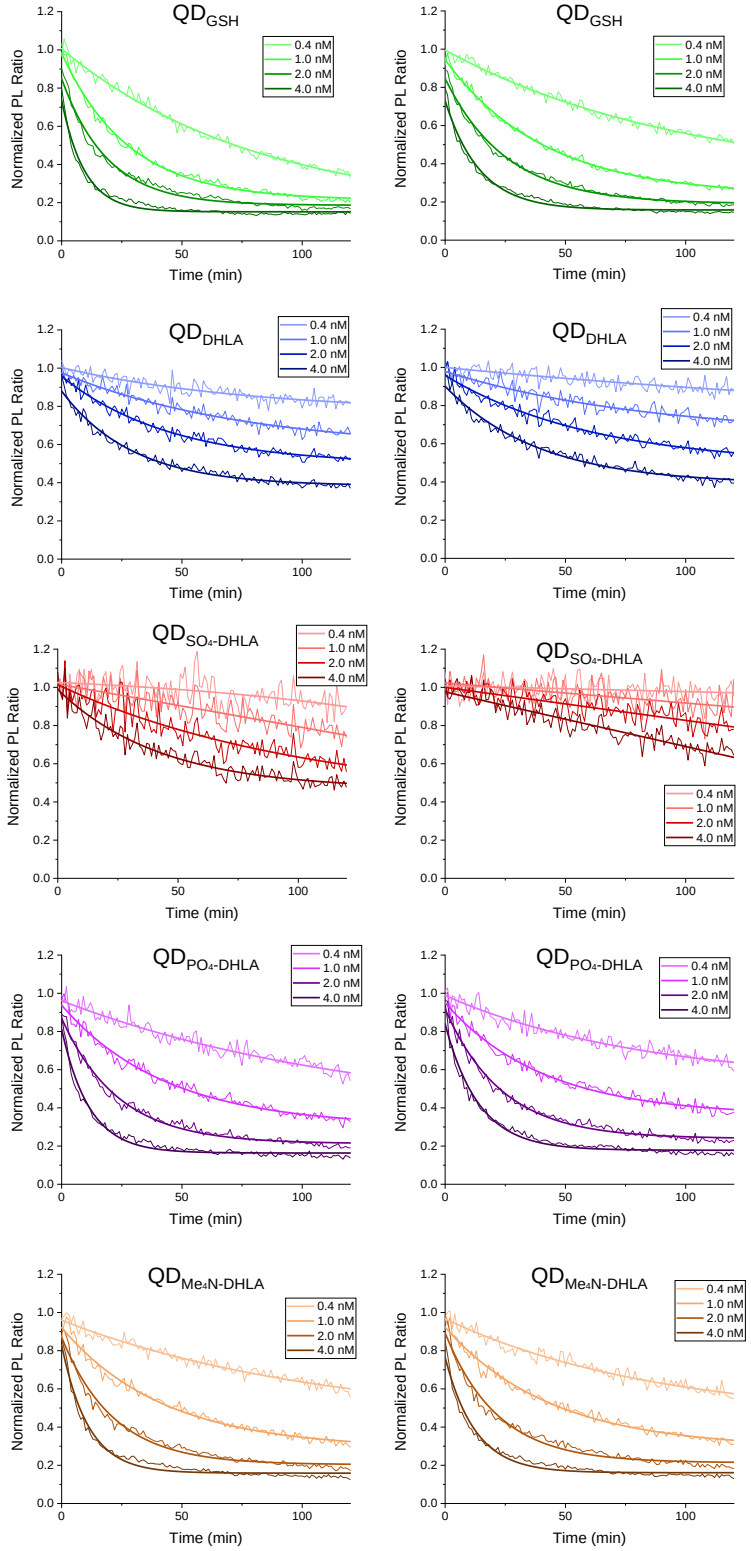

Figure B20 Progress curves for peptide cleavage by chymotrypsin

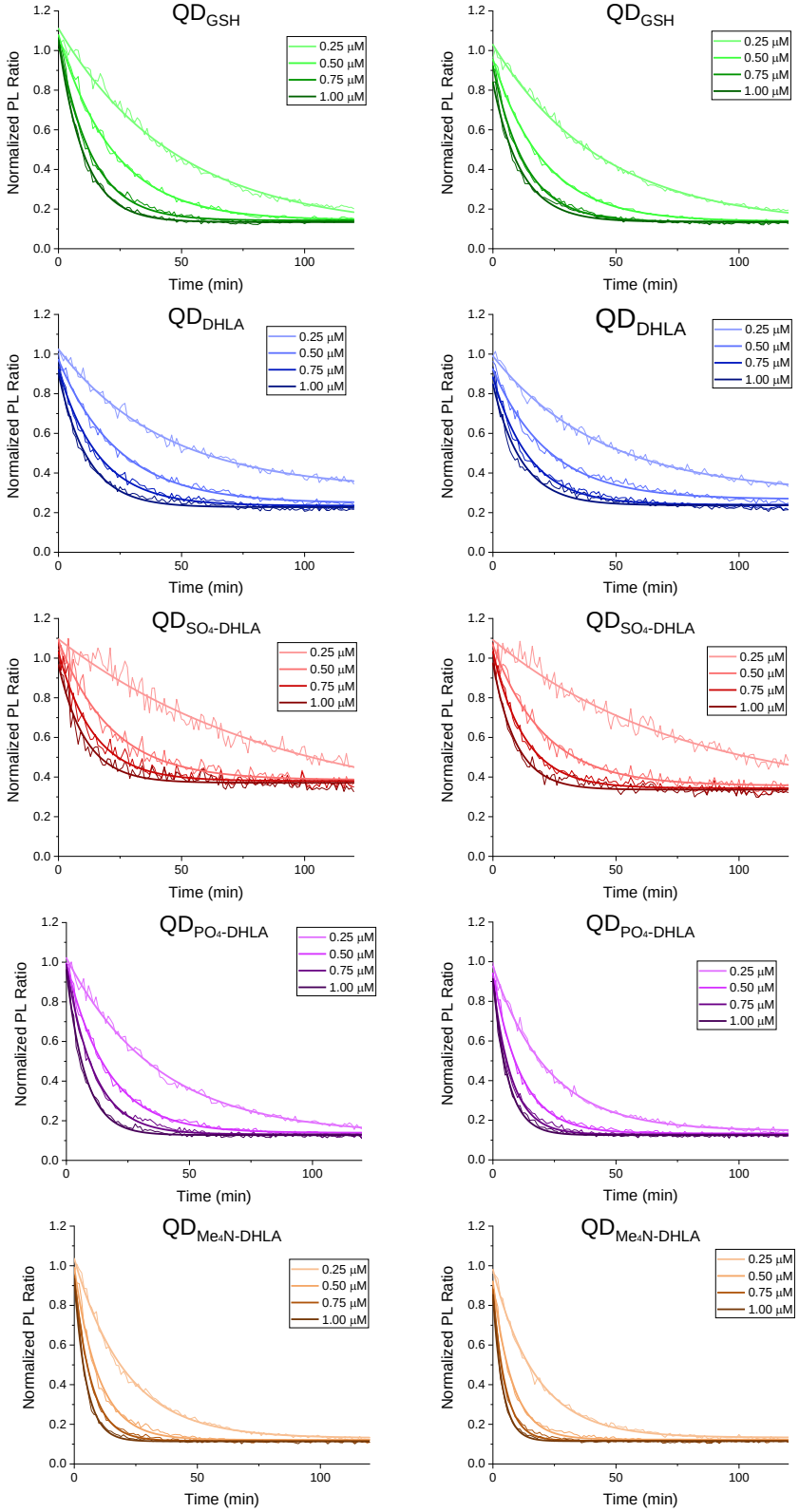

Figure B21 Progress curves for peptide cleavage by elastase

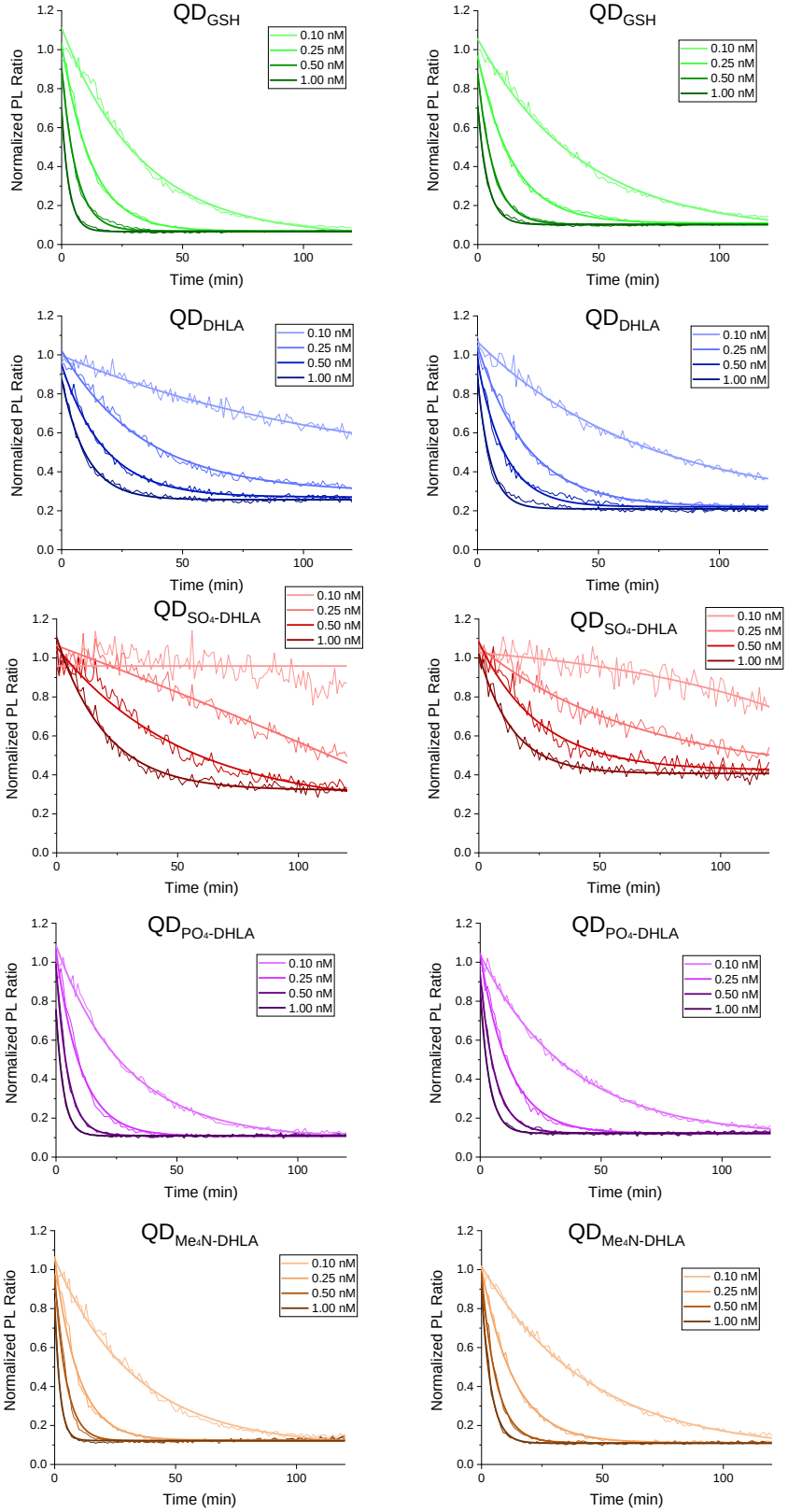

Figure B22 Progress curves for peptide cleavage by proteinase K

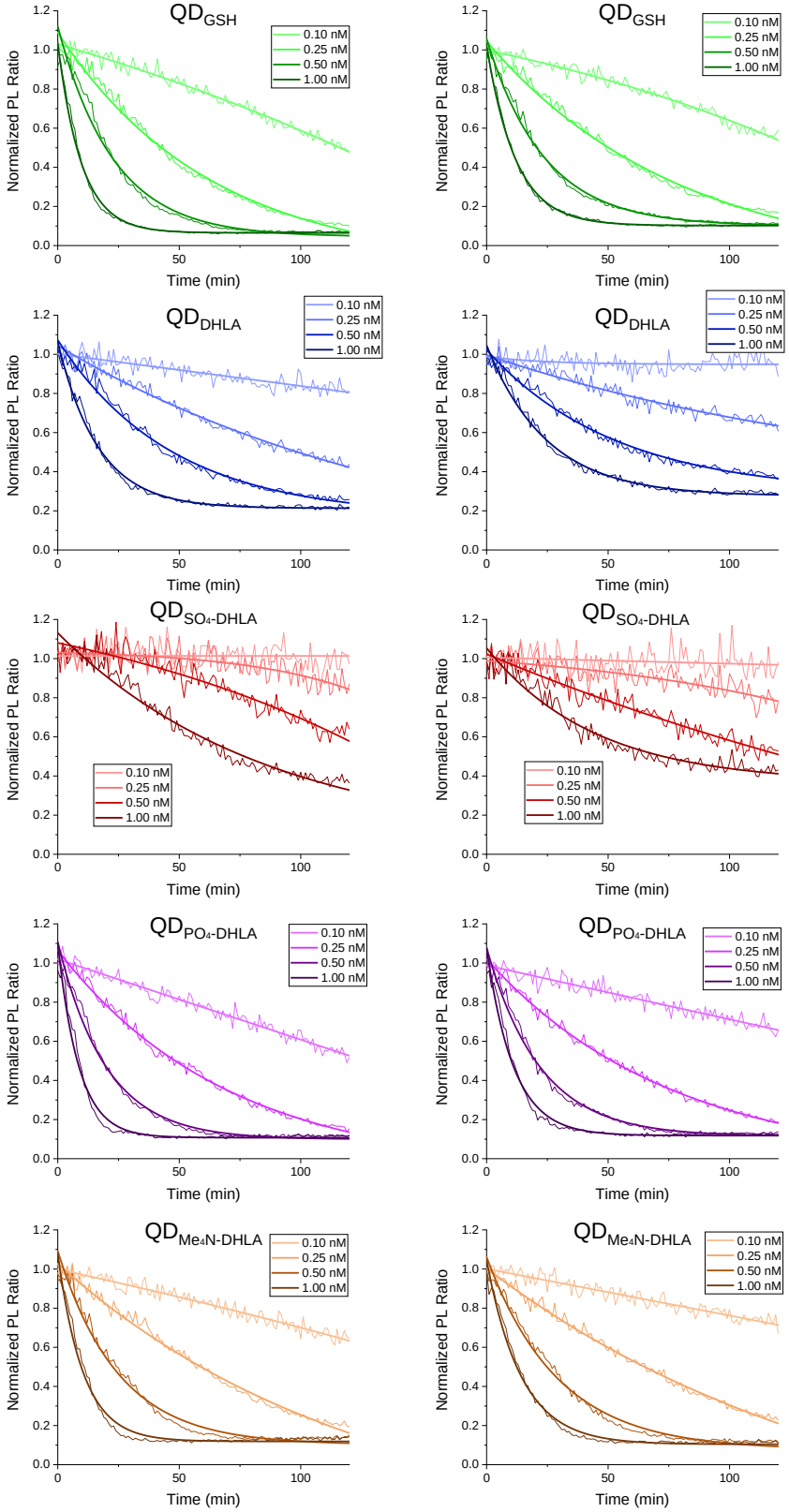

Figure B23 Progress curves for peptide cleavage by subtilisin

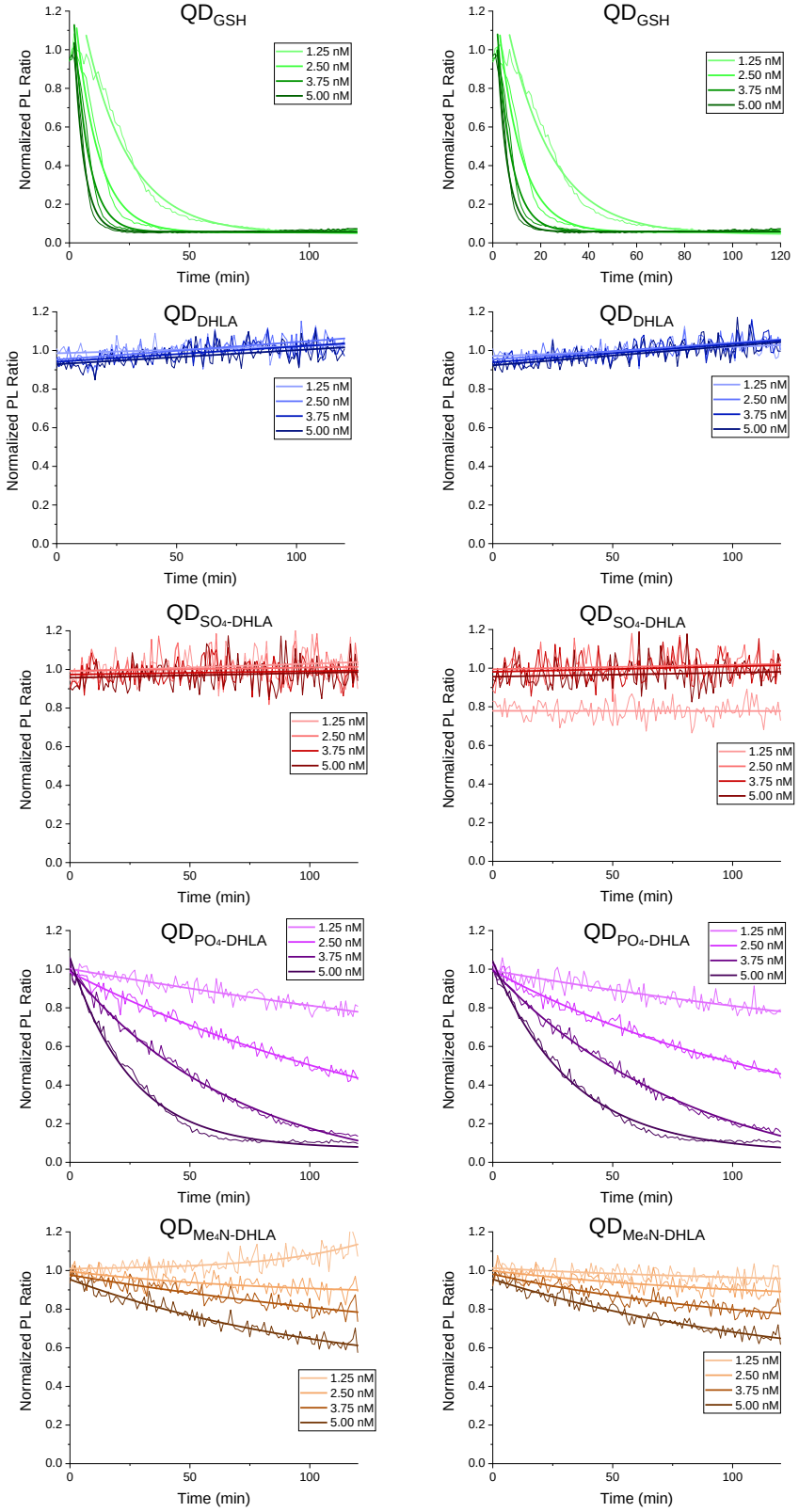

Figure B24 Progress curves for peptide cleavage by papain

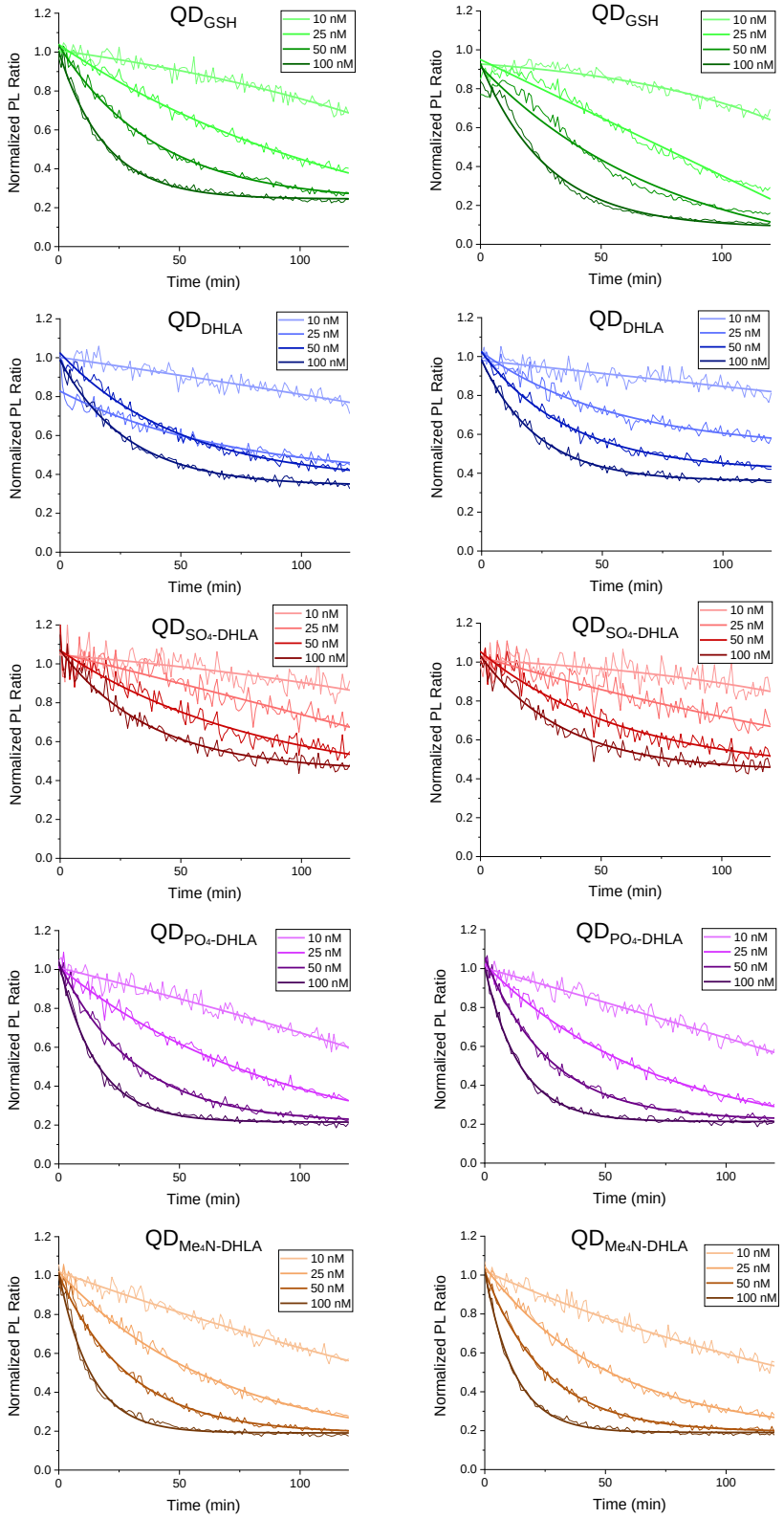

Figure B25 Progress curves for peptide cleavage by endoproteinase LysC

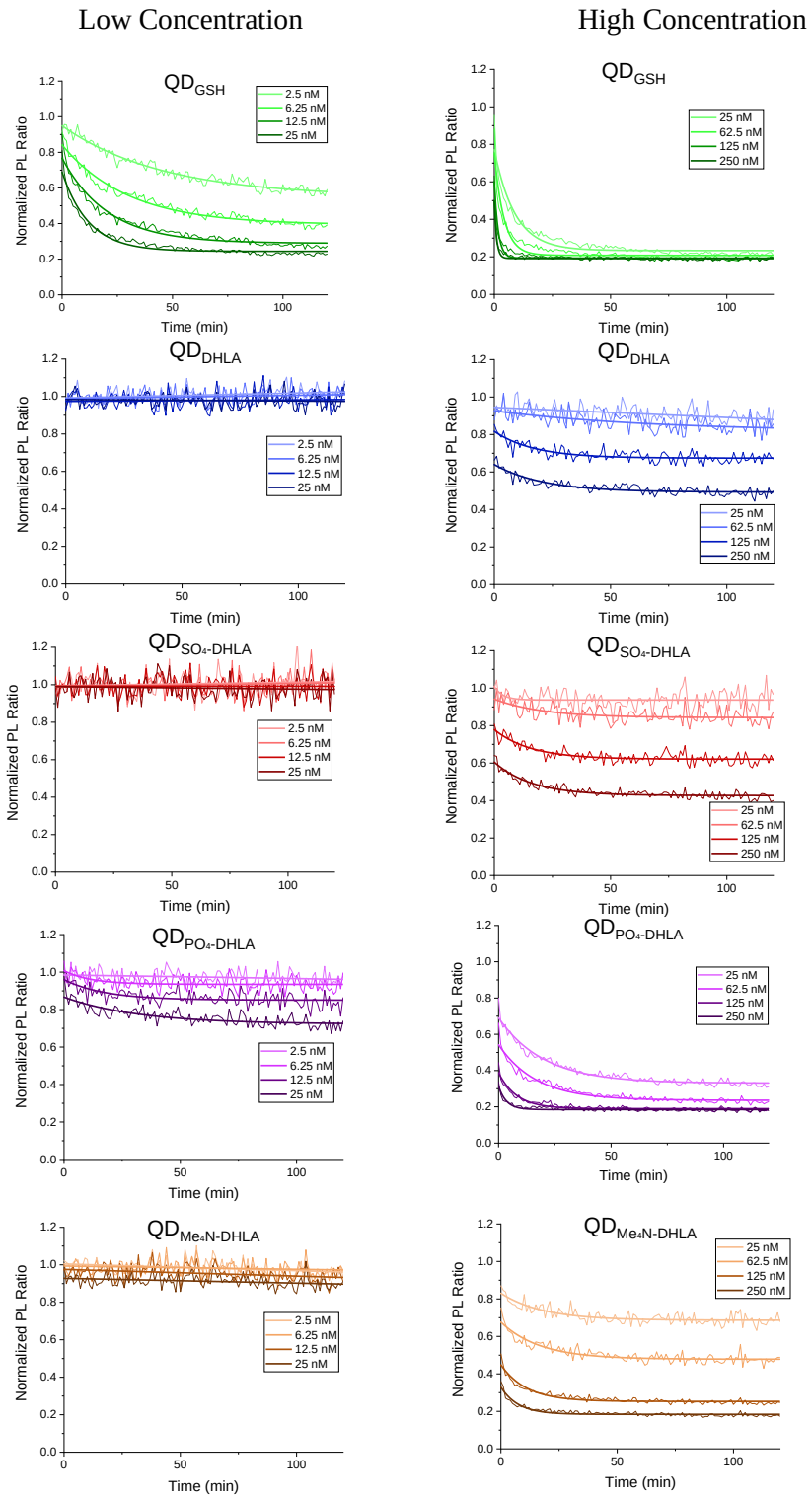

Figure B26 Progress curves for peptide cleavage by plasmin. (Note: two concentration ranges instead of duplicate measurements were tested for plasmin)